Sub-cycle quantum motion in solids under strong terahertz fields

Dissertation

zur Erlangung des Doktorgrades der Naturwissenschaften

(Dr. rer. nat.)

der Fakultät für Physik der Universität Regensburg

Vorgelegt von

Matthias Hohenleutner

aus München

im Jahr 2016

Das Promotionsgesuch wurde eingereicht am 26.01.2016.
Die Arbeit wurde angeleitet von Prof. Dr. Rupert Huber.

Prüfungsausschuss:	Vorsitzender:	Prof. Dr. Andreas Schäfer
	1. Gutachter:	Prof. Dr. Rupert Huber
	2. Gutachter:	Prof. Dr. Christian Schüller
	weiterer Prüfer:	PD Dr. Mariusz Ciorga

Contents

Chapter 1

Introduction

Controlling electronic motion on ever faster time scales lies at the heart of current high-speed electronics. An ongoing quest for increasing electronic clock rates inescapably culminates in one central question: Is there a fundamental limit to the speed of future electronic devices? From a technological point of view, finding an answer to this question primarily necessitates a suitable stimulus to steer electronic motion on ultrafast time scales. Today, all electronic devices rely on externally applied electric fields, whose switching frequencies are limited to the gigahertz range [Kim10] by means of conventional electronics. A promising route to overcome this limitation is to exploit the fastest alternating electromagnetic fields found in nature - the carrier wave of light. This fascinating concept of *lightwave electronics* [Gou07] seems natural, but has challenged state-of-the-art photonics for decades.

The advent of ultrashort laser pulse sources has revolutionized time-resolved spectroscopy and has allowed for observing elementary dynamics of matter on its natural time scale, i.e., on time spans down to the femtosecond scale ($1\,\mathrm{fs} = 1 \cdot 10^{-15}\mathrm{s}$). In conventional pump-probe schemes, cycle-averaged quantities like the intensity and frequency of laser pulses are analysed, for instance after transmission through an optically excited sample. Going one step further, the electromagnetic light field itself might be exploited to drive electronic dynamics, as already pointed out in 1965 in Leonid Keldysh's seminal theoretical work on strong-field ionization in atoms and interband tunneling in semiconductors [Kel65]. It took more than 20 years, however, until the tunneling of electrons in atoms was first proven to be driven by the electric field of a laser pulse [Chi85]. Nowadays, lightwave-driven charge transport is an established, versatile tool to study electronic dynamics under high fields in gaseous media [Bra00]: Strong-field photo-ionization has even been resolved temporally [Uib07, Eck08, Sha12] and has set the stage for controlling the motion of quasi-free electrons. In particu-

lar, carriers may be accelerated and subsequently recollided with their ion core by strong electric lightwaves [Cor93, Lew94]. This dynamics gives rise to the emission of extremely broadband electromagnetic radiation - so-called high-order harmonics. As a specific fingerprint of the underlying mechanism, the emitted radiation carries key information about the process [Chi06, Smi09] as well as the structure of atoms and molecules [Kan05, Sha09, Voz11]. High achievable photon energies up to the soft X-ray range [Ser05] and the capability to form sub-femtosecond pulses [Ant96, Pau01, Dud06] have additionally rendered high-order harmonic generation in gases a yet unparalleled instrument for a series of spectroscopic techniques and have kicked off the development of attosecond science [Cor07, Chi14, Kra14].
Despite the fact that existing, technologically relevant electronics rely on solid-state devices, lightwave-driven charge transport in condensed matter systems is still in its infancy and the process of understanding the underlying dynamics has just begun [Ghi14]. Latest reports have shown that strong light fields can induce optical currents even in dielectrics [Sch13a], which may be exploited for fast signal manipulation [Sch13b]. Non-perturbative high-order harmonic generation in bulk solids has only recently been realized for the first time: Ghimire and co-workers observed high-order harmonics above the fundamental band gap of zinc oxide upon illumination with intense mid-infrared pulses [Ghi10]. Anharmonic intraband currents in non-parabolic electronic bands have been suggested as a responsible mechanism. The potential to temporally resolve or even control the dynamics has remained untapped due to the fluctuating phase of the employed pulses, however. In consequence, many questions regarding the microscopic mechanism dominating high-order harmonic generation have not been answered yet [Ghi14, Hig14]. Envisaged applications like all-optical band structure reconstruction [Vam15b] or next-generation attosecond sources [Ghi14] strongly depend on removing ambiguity and urge for a time-resolved study of high-order harmonic generation in bulk solids.

Exploiting the carrier wave of intense laser pulses in the proper sense of lightwave electronics requires a well-defined and reproducible optical field profile. In the terahertz spectral range ($1\,\mathrm{THz} = 1 \cdot 10^{12}\mathrm{Hz}$), phase-locked electromagnetic few- or single-cycle waveforms are now routinely traced with absolute resolution of amplitude and phase [Wu95, Gal99, Hub00, Sch11, Por14b]. This capability enables the observation of elementary excitations in solids on a *sub-cycle* time scale [Hub01, Ton07, Gün09, Ulb11, Jep11], i.e., with a temporal resolution much better than one single oscillation cycle of the carrier wave. Terahertz photon energies lie well below typical electronic resonances in solids, which is highly favourable for field-driven dynamics. With the recent development of novel efficient sources, the high field strengths needed to control quantum motion

on such short time scales have now also become available in the broadband terahertz regime[1] [Sel08a, Jun10, Hir11a, Kam13]. Examples on terahertz field-induced processes in solids include coherent control of optically dark excitons [Lei08], interband tunneling [Jun12], strong carrier multiplication due to impact ionization [Hir11b], electron-hole recollisions [Zak12] or field-induced phase transitions [Liu12].

In this work, a comprehensive study of solid-state high-order harmonic generation in the bulk semiconductor gallium selenide is presented. Phase-locked waveforms in a frequency range of several 10 THz with atomically strong electric peak fields are used to drive non-perturbative high-order harmonic generation. Record-bandwidth, phase-stable spectra up to the 22^{nd} harmonic order of the fundamental driving frequency are recorded. The observed spectral emission characteristics allow for identifying coherent interband excitation and simultaneously driven, strongly anharmonic intraband transport including dynamical Bloch oscillations as the responsible microscopic mechanisms [Sch14b].
A milestone in solid-state high-order harmonic generation is achieved by the first time-resolved observation of the emission and the underlying microscopic dynamics. It is enabled by a novel cross-correlation scheme with synchronized electro-optic sampling of the terahertz field [Hoh15a]. This way, the emission timing is clocked to the driving waveform with femtosecond-precision - twenty times shorter than one single oscillation cycle of the fundamental field. The observed pulse train is composed of few-femtosecond, nearly unchirped high-harmonic bursts which are precisely synchronized to the driving field crests of one polarity, while the emission is strongly suppressed for the opposite polarity. In combination with a numerical quantum model developed by the groups of Stephan W. Koch and Mackillo Kira in Marburg, this slow-motion picture of the sub-cycle dynamics highlights a strong-field-induced quantum interference between several interband excitation pathways, including electronic transitions below the Fermi level. The non-perturbative nature of the interference effect is proven by its robustness against a variation of the driving field parameters. Frequency and time-resolved measurements of the harmonic pulse trains are finally complemented by polarization-sensitive recordings, facilitating a systematic study of the influence of different crystallographic directions in gallium selenide.

At the beginning of this thesis, a novel high-field terahertz laboratory will be introduced, which targets sub-cycle control of ultrafast charge and spin dynamics in solids (**chapter 2**). Two beamlines deliver phase-locked, electromagnetic few- or single-cycle waveforms with peak field strengths on the order of 100 MV/cm in a broad range

[1] Varying definitions of the terahertz spectral range can be found in literature. Here, the term terahertz will be used for a broadband regime of approximately 0.1 - 100 THz, while the wording multi-THz is used to distinctly address frequencies above 10 THz.

throughout the far- and mid-infrared spectral regions. Amplitude and phase resolution of these transients together with a broadband source of near-infared-to-visible probe pulses enables high-field studies of solid-state quantum dynamics with sub-cycle time resolution.

After a brief review on high-order harmonic generation in gaseous media and its underlying electronic dynamics, the focus of the work lies on the comparably new field of solid-state high-order harmonic generation (**chapter 3**). In particular, the generation and spectral observation of high-order harmonics in bulk gallium selenide by strong multi-THz waveforms (described in more detail in the thesis [Sch14a]) is briefly summarized: Coherent interband excitation and anharmonic intraband transport result in the emission of ultrabroadband and inherently phase-locked harmonic spectra, which cover more than 12 optical octaves.

Chapter 4 presents the very first time-resolved study of high-order harmonic emission from a bulk solid [Hoh15a]. An optical cross-correlation scheme enables a full reconstruction of the temporal fine structure of high-order harmonics from gallium selenide in intensity and relative phase. Moreover, clocking the emission timing with respect to the exact phase of the driving field is achieved by precise temporal correlation with electro-optic traces of the multi-THz waveforms. The unravelled sub-cycle features shed light on a novel strong-field quantum interference between different interband polarization pathways and may provide all-optical access to details of the bandstructure far below the Fermi energy. The ultrashort pulse duration of the emitted harmonic bursts as well as unique pulse shaping possibilities spark hope for next generation solid-state sub-femtosecond sources.

Combining the complementing experimental techniques described above, a profound study of the dependence of harmonic generation on the crystallographic orientation of gallium selenide becomes possible (**chapter 5**). Including a surprising behaviour of the polarization of emitted harmonic radiation, a comprehensive phenomenological model is presented, which draws a conclusive picture of the rich photonic aspects observed for varying driving field directions. A comparison of perturbatively derived symmetry arguments deduced from the point group of the crystal lattice to the orientational dependence of the non-perturbative quantum interference completes this chapter.

As a status report on a currently ongoing project, **chapter 6** provides an outlook on a fundamentally new experimental scheme which is intended to enable the first time-resolved study of electrical spin injection into technologically relevant spintronic devices through tunneling junctions. A novel near-field antenna concept is conceived, which permits biasing epitaxially grown semiconductor heterostructures along their growth direction via single-cycle terahertz waveforms. These ultrashort voltage bursts may drive spin-polarized electrons into a light-emitting diode embedded in the antenna structure,

where the spin-polarization could finally be probed on ultrashort time scales. After a description of the antenna concept and numerical simulations of the electromagnetic response of the structure, the fabrication of a first operational prototype is outlined. Finally, first promising experiments hinting at terahertz-driven tunnel injection are presented.

A brief summary of the most important results of this thesis (**chapter 7**) is followed by a short discussion of their potential impact as well as a novel, complementing experimental approach for sub-cycle control of lightwave-driven quasiparticle dynamics in solids.

Chapter 2

Strong-field terahertz laboratory

One of the main motivations for the development of effective sources in the terahertz spectral range has always been a huge variety of elementary excitations featuring resonances in the range of 0.1 - 100 THz. From rotational and vibrational degrees of freedom in atoms and molecules via quasi-free electrons in semiconductors [Hub01] to exotic quasiparticles in solids like excitons [Poe15], magnons [Kam11], phonons [Kim12, Por14a], Cooper pairs and many more: Addressing their spectral fingerprints in the broadband terahertz range has enabled unique insights into their intrinsic dynamics [Bea02, Gan05, Ton07, Ulb11, Jep11], which typically occur on the femtosecond time scale. Above that, the relatively low photon energy of terahertz radiation ($h\nu = 4.13\,\mathrm{meV}$ for $\nu = 1\,\mathrm{THz}$) helps to selectively observe the dynamics under study without "disturbing" the system, e.g., by carrier excitation via linear absorption. Researchers all over the globe have thus put great efforts in closing the so-called THz-gap during the last decades. The availability of phase-locked pulses throughout this frequency range of the electromagnetic spectrum [Hub00, Küb04, Zen07, Sel08a, Sel08b] and the ability of their sensitive detection in amplitude and phase [Wu95, Gal99, Hub00, Sch11, Por14b] have nowadays opened up new objectives and paradigms. High-field waveforms may now serve as an ultrashort voltage bias to excite and coherently control the mentioned dynamics [Zak12, Kam13, Maa16]. Exploiting also the magnetic field component extends the range of accessible degrees of freedom and the class of potential material systems under study [Kam11]. To literally carry these thoughts to extremes, strong-field waveforms in the terahertz regime prove to be the ideal tool to even non-perturbatively drive and control highly nonlinear charge carrier dynamics far away from any resonance [Jun12, Sch14b, Lan14, Hoh15a, Lan16]. Thereby, the former THz-gap may even be closed in the context of strong-field light-matter interaction, a field that has so far been limited to the visible or near-infrared spectral range on ultrashort time scales.

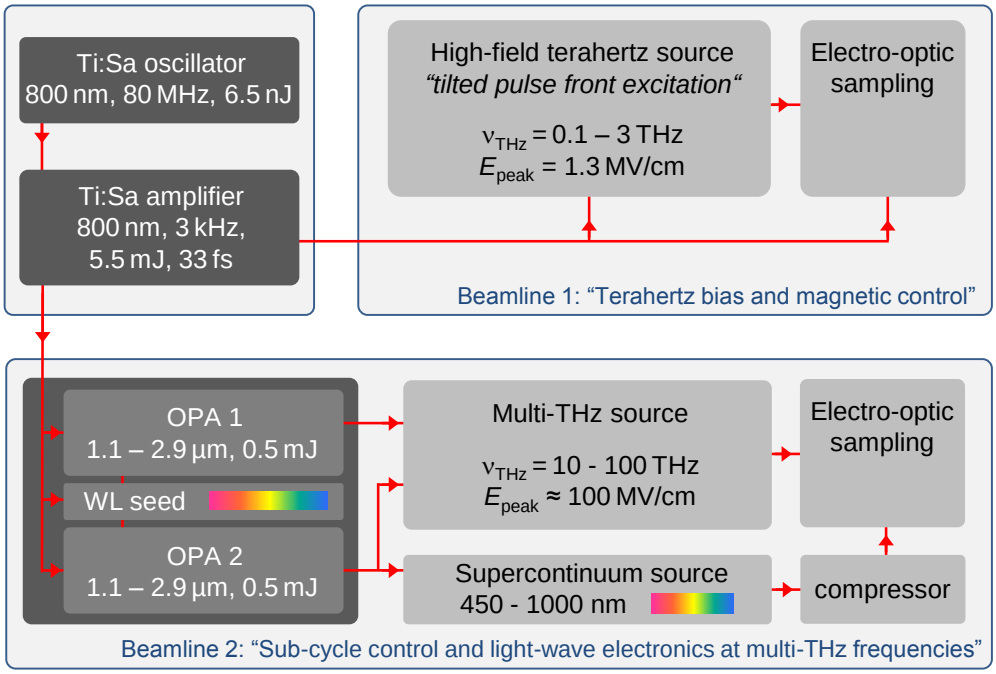

Figure 2.1: Schematic layout of the high-field terahertz source: A titanium-sapphire amplifier, seeded by a titanium-sapphire oscillator, delivers pulses with energies of 5.5 mJ at a repetition rate of 3 kHz which are guided to two experimental beamlines: A high-field source based on velocity-matching by tilted pulse fronts generates phase-locked, intense waveforms at a centre frequency of around 1 THz with peak electric field amplitudes on the order of 1 MV/cm (beamline 1). A complementary source (beamline 2) is based on difference frequency generation between two near-infrared pulse trains delivered by two parallel optical parametric amplifiers which are seeded by the same white-light pulses. Phase-controlled waveforms obtained by this setup can be tuned between approximately 10 and 100 THz. Octave-spanning supercontinua from an additional white-light source are recompressed to a pulse duration of 8 fs and are employed for electro-optic sampling and as a probe pulse for terahertz-induced dynamics on sub-cycle time scales.

The realization of such experiments calls for two main technological achievements. The first one is the generation of intense, phase-locked and long-term stable terahertz waveforms. The second one is to achieve sub-cycle time resolution, i.e., the ability to detect the high-field waveforms directly in amplitude and phase as well as to observe the field-induced dynamics on a time scale much shorter than one single oscillation cycle of the driving field. The following chapter will introduce a novel high-field terahertz source which is capable of fulfilling both requirements.

Figure 2.1 gives a schematic overview of the unique laser system: The core of the developed technology platform is a state-of-the-art titanium-sapphire (Ti:Sa) laser amplifier

based on the principle of chirped pulse amplification (a detailed description of the commercial laser system can be found in [Sch14a]). Comparably weak seed pulses delivered from a Ti:Sa oscillator (pulse energies[1] of 3.9 nJ at a repetition rate of 80 MHz) are temporally stretched in a grating assembly and subsequently amplified in two stages: A regenerative amplifier lowers the repetition rate to 3 kHz and amplifies the pulse energy to 2.8 mJ before it is further boosted to a value of 5.5 mJ in a single-pass amplifier. After re-compression of the pulses in a grating compressor, the pulse length is as short as 33 fs.

These pulses can be sent to two different beamlines which might be operated in parallel or individually. The first beamline is dedicated to controlling charge and spin dynamics in condensed matter on ultrashort time scales by applying high-field waveforms at a centre frequency of approximately 1 THz as an ultrashort voltage or magnetic bias. To this end, an intense terahertz source based on so-called tilted pulse front optical rectification has been developed, which delivers pulse energies on the order of 1 µJ and peak electric field amplitudes on the order of 1 MV/cm.

The second beamline extends the field of applications towards extremely nonlinear terahertz-driven dynamics at even higher peak fields in the ultrabroadband multi-THz range (10 - 100 THz). Two optical parametric amplifiers, which share a common white-light seed, provide signal pulses with centre wavelengths between 1.1 µm and 1.7 µm and pulse energies of up to 0.5 mJ each. The phase-stable idler pulses are tunable within a broad spectral range between 1.6 µm and 2.9 µm. Difference frequency mixing of the two phase-correlated signal pulse trains yields widely tunable, intense and phase-locked few-cycle waveforms with pulse energies of up to 30 µJ and peak electric fields on the order of 100 MV/cm. Octave-spanning supercontinua from an additional white-light source are compressed to a pulse length of only 8 fs and form an ideal tool both for tracing the generated multi-THz waveforms in amplitude and phase via electro-optic sampling and for probing THz-field-induced dynamics on a time scale shorter than one single oscillation cycle of light.

2.1 Strong fields at low terahertz frequencies

The low-frequency terahertz regime (0.1 - 10 THz) has been of great interest for fundamental research owing to a vast number of low-energy excitations [Bea02, Ton07, Ulb11, Jep11, Gan05] such as rotational modes in molecules or bound electron-hole pairs [Mén14, Poe15] as well as lattice [Kim12, Por14a] and spin [Kam11] degrees of freedom in solids. The recent development of effective terahertz sources has extended the capabilities from pure observation of these dynamics to their selective control both

[1] Only 60% of the available average power of the oscillator is used to seed the amplifier.

by resonant or non-resonant excitation. Besides large-scale facilities like free electron lasers or linear accelerators, which typically deliver intense but narrowband terahertz pulses, table-top sources based on optical rectification (OR) of femtosecond laser pulses have proven to be the tool of choice for compact, flexible and efficient generation of spectrally broad and strong single-cycle terahertz waveforms.
This section presents a brief discussion of the newly developed terahertz source based on optical rectification in lithium niobate ($LiNbO_3$). Since an introduction into the underlying nonlinear optical effects can be found elsewhere [Boy03], the focus of the discussion is on the so-called tilted pulse front scheme, a particularly effective method for velocity matching in the generation process [Heb02]. After a detailed explanation of the experimental setup and its specifications, a short outlook on some of the possible applications is given: First experiments shed light on terahertz-induced interband tunneling and non-perturbative carrier multiplication in bulk gallium arsenide [Lan14], nonlinearities in all-magnetic terahertz-driven spin dynamics [Bai16], as well as nonlinear excitation of Landau-quantized carriers in two-dimensional electron gases [Maa16].

2.1.1 Velocity matching by tilted pulse front excitation

A number of material systems for optical rectification ranging from photo-conductive switches [You93] via organic and inorganic nonlinear crystals to gases have been demonstrated to be feasible for strong-field terahertz generation [Kam13]. Organic crystals like OH1 [Ruc12], however, have shown to suffer from thermal damage at required peak intensities for efficient terahertz generation at the repetition rate of 3 kHz of the laser system used here. While terahertz air photonics [KY12] shows unprecedented performance in terms of achievable bandwidth, inorganic crystals like zink telluride (ZnTe), gallium phosphide (GaP) or lithium niobate ($LiNbO_3$) are unbeaten in terms of highest reachable peak fields [Bla07, Hir11a]. Comparing the relevant key figures of inorganic nonlinear media for efficient OR, $LiNbO_3$ takes over an outstanding position: Its nonlinear coefficient as high as $d_{\mathrm{eff}} = 168\,\mathrm{pm/V}$ surpasses the values for ZnTe and GaP by a factor of more than 2 and 6, respectively [Heb04]. The bandgap energy of $LiNbO_3$ of 3.8 eV prevents two-photon absorption of the optical or near-infrared pump pulses, and a comparably high damage threshold on the order of $500\,\mathrm{GW/cm^2}$ or more allows for elevated pump pulse intensities and thus high generation efficiencies.
However, efficient frequency conversion based on optical nonlinearities is always limited by phase matching requirements. For the case of OR, the phase velocity $v_{\mathrm{THz}}^{\mathrm{ph}}$ of the generated terahertz waveform has to equal the group velocity $v_{\mathrm{NIR}}^{\mathrm{gr}}$ of the near-infrared femtosecond pulses in order to avoid destructive interference during propagation inside

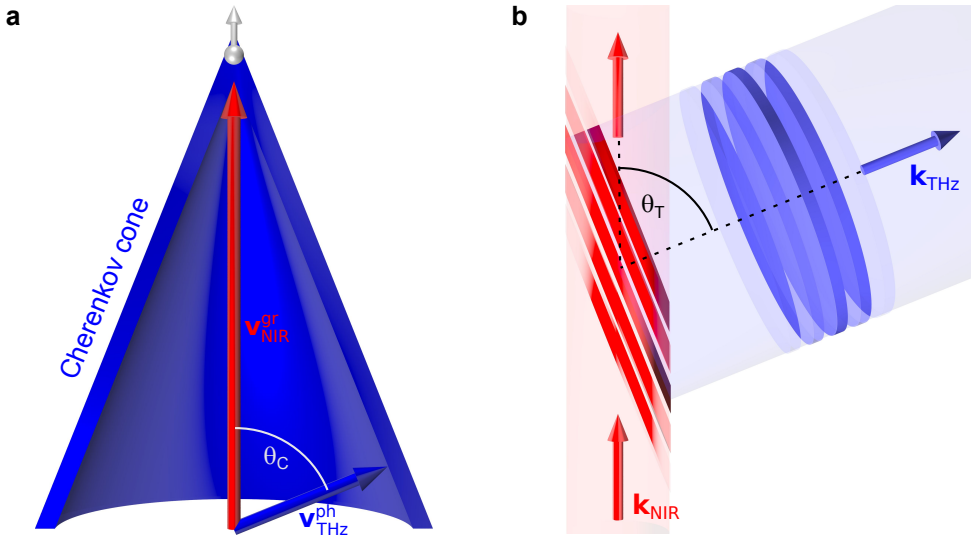

Figure 2.2: Cherenkov-type phase matching for efficient terahertz generation: a, An accelerated charged particle (grey sphere) emits electro-magnetic radiation (blue). If the propagation speed of the particle is faster than the phase velocity of the emitted radiation in the surrounding medium, the radiation forms a so-called Cherenkov cone with a characteristic angle θ_C. An analogous analysis holds for the case of non-velocity-matched OR in $LiNbO_3$, with a small spot of nonlinear polarization propagating faster (group velocity v_{NIR}^{gr}) than the phase fronts of the emitted terahertz radiation (phase velocity v_{THz}^{ph}). **b,** By tilting the intensity fronts of large-area near-infrared pump pulses, velocity matching (compare equation 2.1) can be fulfilled in a non-collinear way if the tilt angle of the pulse fronts equals the Cherenkov angle $\theta_T = \theta_C = \cos^{-1}(v_{THz}^{ph}/v_{NIR}^{gr})$. After [Heb02].

the nonlinear medium [Boy03, Heb02]:

$$v_{NIR}^{gr} = v_{THz}^{ph} \tag{2.1}$$

In $LiNbO_3$, an optical pulse at a centre wavelength of 800 nm unfortunately propagates much faster than the phase front of a generated terahertz wave at a frequency of 1 THz ($v_{NIR}^{gr} > 2v_{THz}^{ph}$). If the lateral extension of the pump spot is small compared to its longitudinal spread inside the material, a situation arises which is similar to the so-called Cherenkov radiation observed, e.g., in the water shielding of neutron reactors: An accelerated charged particle emits electromagnetic radiation. If the velocity of the charged particle is higher than the group velocity of the emitted radiation in the surrounding medium, the emission forms a cone (Cherenkov angle θ_C, compare figure 2.2a) - in perfect analogy to the well-known Mach cone for sound waves. Replacing the radiation source (charged particle depicted by the grey sphere) with the nonlinear polarization within the $LiNbO_3$-crystal induced by the propagating pump pulse yields the same situa-

tion with the emitted radiation lying in the terahertz frequency range [Aus84]. Collecting the emitted, divergent terahertz radiation forms a formidable task, however, which is practically not feasible. Furthermore, the generation efficiency is strongly limited by the requirement of a narrow transversal beam profile [Aus84].
Nevertheless, a seminal idea to make use of this non-collinear generation scheme was introduced by Hebling and co-workers in 2002 [Heb02]: If the intensity fronts of large-area near-infrared pump pulses are tilted by an angle θ_T with respect to their propagation direction $\mathbf{k}_{NIR}$ (see figure 2.2b), the excited nonlinear polarization within the medium will also follow this tilted intensity front. According to Huygen's principle, the generated terahertz radiation will constructively interfere along phase fronts parallel to the tilted pump intensity fronts and will thus propagate along $\mathbf{k}_{THz}$ at the angle θ_T with respect to $\mathbf{k}_{NIR}$. Consequently, the condition of velocity matching (equation (2.1)) has to be fulfilled for the projection of v_{NIR}^{gr} along $\mathbf{k}_{THz}$:

$$v_{NIR}^{gr} \cdot \cos\theta_T = v_{THz}^{ph} \tag{2.2}$$

From the above considerations and by comparison of figures 2.2a and b, it becomes obvious that this condition can be fulfilled if the tilt angle of the pulse fronts exactly equals the Cherenkov angle $\theta_T = \theta_C = \cos^{-1}(v_{THz}^{ph}/v_{NIR}^{gr})$. With this new approach of phase matching, the requirement of small pump spots for Cherenekov-type generation schemes do no longer limit the efficiency. In contrast to critical phase matching, the polarization direction of the pump and THz beams may additionally be chosen to be parallel to the crystal direction according to the highest nonlinear coefficient (c-axis for the case of $LiNbO_3$ [Fei85]). This way, the effective generation length inside the crystal is not limited by so-called spatial walk-off [Die06] between the near-infrared and the THz pulses, as it is the case for birefringent phase matching.

2.1.2 The tilted pulse front source - experimental setup

As discussed in the previous section, optical rectification based on tilted pulse front excitation in $LiNbO_3$ is a promising technique to efficiently generate intense, phase-locked terahertz waveforms. The novel experimental setup introduced here is based on the titanium-sapphire laser amplifier (see figure 2.1) delivering 33-fs-short pulses at a centre wavelength of approximately 800 nm. A simplified sketch including the most relevant optical elements of the setup is shown in figure 2.3a: After a mirror telescope decreasing the size of the nearly Gaussian beam profile by a factor of 0.75 to a diameter of 4.1 mm (intensity full-width at half-maximum), the pulses are split into two branches. A minor part of the pulse energy ($\approx 1\%$, illustrated by the dashed line in figure 2.3a) is used as a gating pulse for electro-optic sampling or sub-cycle probing. The major part of

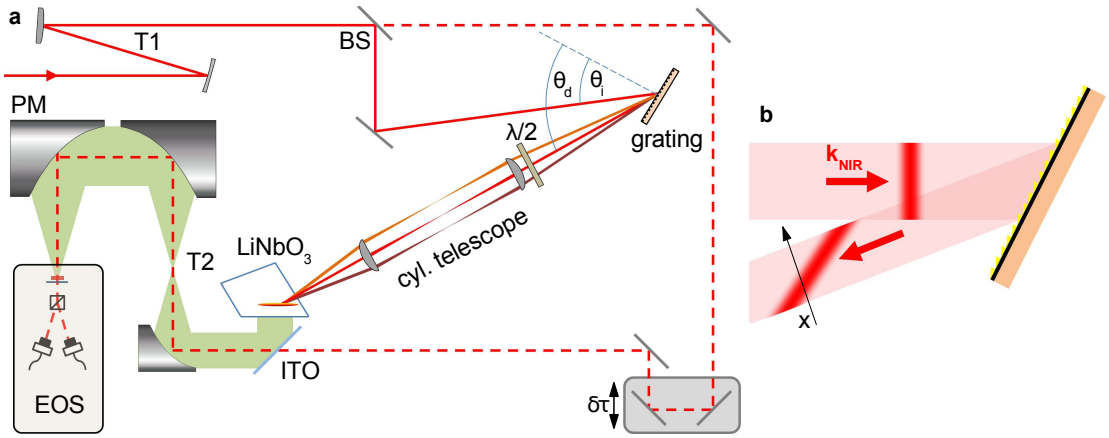

Figure 2.3: High-field terahertz source based on tilted pulse front excitation: a, Simplified sketch of the experimental setup. PM: parabolic mirror, T1: spherical mirror telescope, BS: beamsplitter, $\lambda/2$: half-wave plate, ITO: indium-tin-oxide-coated beamsplitter, T2: parabolic mirror telescope, $\delta\tau$: variable mechanical delay, EOS: electro-optic sampling. **b,** Before diffraction off a grating, the intensity front of a short near-infrared pulse is oriented perpendicular to its wave vector $\mathbf{k}_{\mathrm{NIR}}$. The diffraction induces a pulse front tilt which is analogous to a varying delay of the intensity envelope (dark red) for different lateral beam positions x.

the average power is exploited for the generation of intense terahertz pulses. To realize the pulse front tilt, the generation pulses are guided onto a grating, before focusing them into the $LiNbO_3$ prism via a second telescope composed of two cylindrical lenses (see below for a detailed description of the imaging optics). A half-wave plate rotates the initially horizontal polarization by 90 degrees in order to address the largest nonlinear tensor element of $LiNbO_3$ and to fulfil the velocity matching condition. The $LiNbO_3$ crystal is cut at an angle of 62° (pulse front tilt angle, see below), which ensures both normal incidence of the pump beam and emission of the generated terahertz pulses perpendicular to the exit facet in order to minimize reflection losses. After blocking the remaining pump stray light with a germanium waver (not shown), an indium-tin-oxide-coated beamsplitter combines the nearly collimated terahertz pulses and the near-infrared gating pulses, which are collinearly guided through a magnifying telescope (magnification factor 7) composed of gold-coated parabolic mirrors. A third parabolic mirror is used to tightly focus the terahertz waveforms to a nearly diffraction-limited spot size for electro-optic sampling [Wu95, Wu97, Gal99] of the waveforms or high-field experiments (see below).

Pulse front tilt angle and imaging system

A tilted intensity front of a femtosecond pulse can be induced by diffraction off a grating (see figure 2.3b). For the simplified case of a monochromatic wave of wavelength λ incident on a grating of groove density g, it is straightforward to show that the pulse front tilt angle θ after diffraction (first order) amounts to

$$\theta = \tan^{-1}(g\lambda/\cos\theta_\mathrm{d}), \tag{2.3}$$

with the diffracted angle θ_d as defined in figure 2.3a. Note that the phase fronts of the near-infrared pulses are still perpendicular to $\mathbf{k}_\mathrm{NIR}$, but the intensity envelope of the pulse is temporally shifted as a function of the lateral beam coordinate x (see figure 2.3b). However, angular dispersion of the broadband pulses requires an additional optical imaging system [Fül10, Pál08], which has to fulfil two major tasks in order to ensure efficient terahertz generation: The pulse front tilt angle has to be adjusted such that equation (2.2) holds, while, on the other hand, the angularly dispersed beam has to be re-focused in a way that the grating is exactly imaged onto the tilted intensity front within the crystal. In other words, the tilt angle of the grating image, which reunites the different wavelengths and guarantees short pulse lengths inside the crystal, has to equal the pulse front tilt angle of the monochromatic constituents of the pulse. A detailed analysis of the imaging requirements and the specifications of a cylindrical lens system as depicted in figure 2.3a can be found in [Hir11a]. The appropriate pulse front tilt angle θ_T within the $LiNbO_3$ prism can be determined by calculating the group and phase velocities at a wavelength of 800 nm and 1 THz, respectively, and solving equation (2.2). For the case of stoichiometric manganese-doped lithium niobate (Mg:$LiNbO_3$), which is used here owing to its enhanced resistivity against photo-refractive damage [Che69, Heb04], a pulse front tilt angle of approximately $\theta_\mathrm{T} = 62°$ has to be reached. Taking the magnification of the telescope and refraction at the entrance facet of the crystal (group index $n^\mathrm{gr}_\mathrm{NIR}$) into account, the pulse front tilt angle reads

$$\theta_\mathrm{T} = \tan^{-1}\left\{\frac{\lambda g}{n^\mathrm{gr}_\mathrm{NIR} m \cos\theta_\mathrm{d}}\right\}. \tag{2.4}$$

This condition connects the groove density of the grating, the diffracted angle as well as the horizontal magnification factor m of the cylindrical telescope. Here, a grating with a line density of $g = 1800\,\mathrm{mm}^{-1}$ and a magnification factor of $m = 0.6$ of the telescope have been chosen.

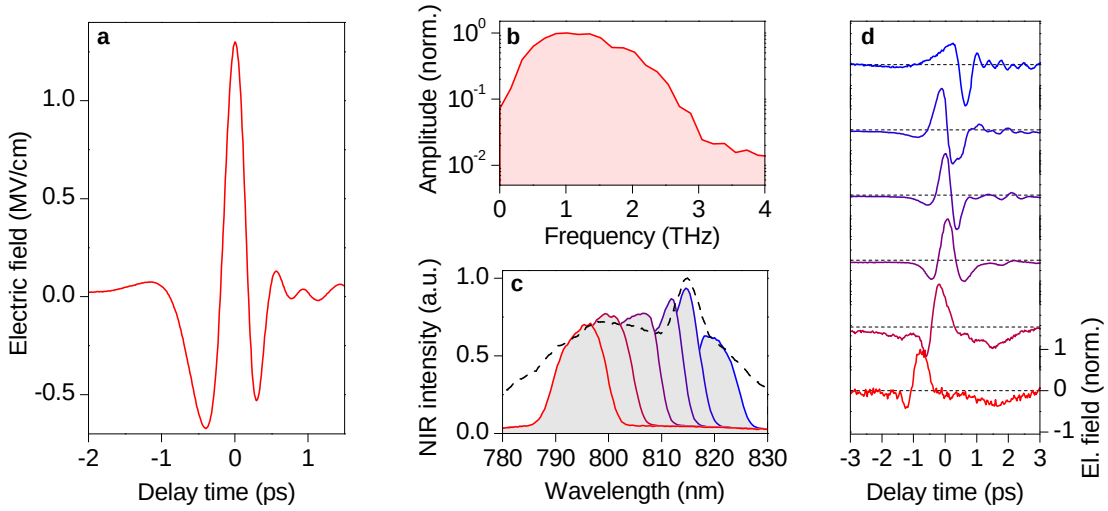

Figure 2.4: Ultrashort and intense terahertz waveforms: a, Typical waveform of an intense, single-cycle terahertz pulse featuring a peak electric field of 1.3 MV/cm. The corresponding amplitude spectrum (Fourier transform) is shown in panel b. **c,** Varying the centre wavelength of the near-infrared pump pulses (different colours) within the broad spectrum delivered by the titanium-sapphire amplifier (black dashed) changes the shape and the carrier-envelope phase of the generated terahertz waveforms (corresponding colours in panel d).

High-field terahertz pulses and waveform shaping

If the $LiNbO_3$ crystal is kept at room temperature, the novel setup delivers terahertz waveforms with pulse energies of approximately 0.5 µJ and peak electric fields on the order of 1 MV/cm (see figure 2.4a). The spectrum covers a range of 0.1 - 3 THz as can be directly seen by Fourier transformation of the electro-optic trace (figure 2.4b). These waveforms represent the ideal tool for high-field terahertz bias experiments, where an ultrashort and particularly well-defined voltage pulse is applied to a semiconductor, for instance. Especially for tunneling experiments on ultrashort time scales as described in chapter 6, it will become crucial to control the shape of the waveform and to create an ideally unidirectional voltage bias. While the integral over the whole field profile of a propagating wave has to vanish exactly, a slight chirp of the waveform (figure 2.4a) makes for an asymmetric shape with respect to positive and negative peak fields. As pointed out in reference [Fül10], a pulse duration of the pump pulses of several hundreds of femtoseconds and a corresponding narrow spectrum would be preferable for efficient terahertz generation. The ultrashort pulses (pulse length: 33 fs) used here, however, turned out to open a new perspective for controlled field shaping of the generated waveforms: Since optical rectification can be understood as difference frequency generation within the broad pump spectrum, it is obvious that changing the latter will strongly

influence the emitted waveform. Experimentally, this task can easily be achieved via spectral amplitude modulation of the broadband pump pulses (black dashed curve in figure 2.4c). By selecting different parts of the pump pulse spectrum (see colour curves in figure 2.4c) with two razor blades in the Fourier plane between the two cylindric lenses shown in figure 2.3a, the carrier-envelope phase (CEP) of the ultrashort terahertz transients can be adjusted as shown in corresponding colours in figure 2.4d. The shorter the pulse envelope, the more pronounced the impact of a variation of the CEP becomes [Bra00]. At the limit of a single-cycle pulse as generated here, the whole waveform is drastically altered. This way, switching from a field trace with a dominant positive field crest to a symmetric one or even a dominant negative peak becomes possible in a straightforward and reproducible way.

Boosting the pulse energies by cryogenic cooling

Terahertz generation by optical rectification in solids can be exploited either above or below the reststrahlen band of the employed material which is typically located in a frequency range between 6 and 10 THz for commonly used nonlinear crystals. In lithium niobate, the transversal optical phonon exhibits a resonance frequency of 7.44 THz, which leads to a drastic increase in the linear absorption when approaching the phonon frequency, as can be seen in the extinction coefficient $\kappa(\nu)$ shown in figure 2.5b. Cooling to cryogenic temperatures lowers the damping of the lattice vibration and narrows the absorption peak (see also inset to figure 2.5b), which is expected to enhance the overall efficiency of terahertz generation [Heb04, Bak08].
In order to benefit from the reduced terahertz absorption at low frequencies, a bath cryostat has been developed and manufactured[2], which cools the $LiNbO_3$ prism to a temperature of 77 K. The crystal is placed on a hollow copper finger (figure 2.5a) in direct contact with the liquid nitrogen bath, which is shielded by an insulation vacuum of a pressure on the order of 10^{-7}mbar. A technological challenge has been the choice of well-suited optical windows for the cryostat. The near-infrared pump pulses are guided through an anti-reflection coated glass window. The exit window for the generated terahertz radiation should have a large aperture while being vacuum-stable, and should not exhibit considerable absorption and dispersion in the terahertz range. A cost-effective material fulfilling these requirements is biaxially-oriented polyethylene terephthalate (BoPET), which is commercially available, e.g., under the brand name *Mylar*. An only 50-µm-thick sheet of this foil covers the exit flange and is fixed by a clamping ring. This custom-built window does not measurably influence the transmitted terahertz waveform, is sufficiently leak-tight to maintain the insulation vacuum and has

[2]Design, construction and manufacturing by Martin Furthmeier.

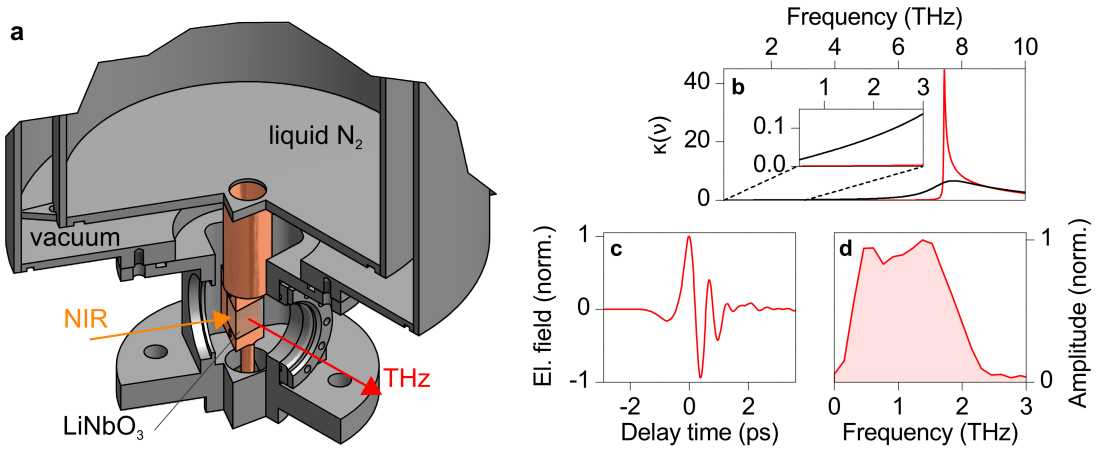

Figure 2.5: Cryogenic cooling of the $LiNbO_3$ crystal: a, Cutout of the custom-built cryostat: A vacuum-shielded reservoir of liquid nitrogen cools a hollow copper finger clutching the $LiNbO_3$-prism. The near-infrared pump beam enters the vacuum chamber via an anti-reflection coated glass window (not shown), while the terahertz exit window is realized by a thin BoPET-foil held in place by a clamping ring. **b,** Extinction coefficient κ of $LiNbO_3$ as a function of the frequency for room temperature (300 K, black) and a temperature of 10 K (red). The inset shows a magnified part of the data in the relevant range from 0.5 to 3 THz. Underlying dielectric functions have been taken from references [Bak08, Heb04]. **c,d,** Electro-optically detected waveform (c) emitted from the cooled $LiNbO_3$ crystal and its Fourier transform (d).

not shown any degradation effects over years.

Compared to the performance at room temperature, the emitted terahertz power is increased by almost a factor of three by cryogenic cooling, yielding pulse energies of approximately 1.3 µJ. As expected from the reduced absorption especially for higher frequencies (compare figure 2.5b), the generated field transients are shifted to slightly higher central frequencies (figures 2.5c and d) and feature a more symmetric waveform. Diffraction limited focusing allows for peak electric fields on the order of 1.5 MV/cm [Lan14], which correspond to magnetic peak fields on the order of 0.5 T.

2.1.3 Semiconductors under strong terahertz bias and coherent magnetic control

The performance of the novel high-field source of low-frequency terahertz waveforms has been strikingly demonstrated in a row of first experiments on ultrafast charge carrier dynamics in semiconductors [Lan14, Maa16] and nonlinear spin control in antiferromagnetic nickel oxide [Bai16]. While the experiments will be described in detail elsewhere, a brief summary of the results shall provide a first glimpse on the new experimental and physical perspectives opened up by the availability of ultrastrong waveforms in the tera-

hertz range. Beyond that, a completely new approach to electrically inject spin-polarized tunnelling currents into technologically relevant semiconductor heterostructures on ultrashort time scales will be discussed in chapter 6.
The electric field component of strong terahertz waveforms can be used to bias semiconductors on sub-cycle time scales with peak electric fields far beyond the limit of dielectric breakdown for DC-voltages. Custom-tailored antenna structures fabricated by electron-beam lithography can additionally be used to concentrate electric near fields on length scales far below the diffraction limit, thereby enhancing the peak fields even further. Using such metamaterial resonators fabricated on undoped bulk gallium arsenide, peak electric fields on the order of more than 10 MV/cm have been generated locally [Lan14]. These strong fields cause quasi-static interband tunneling across the fundamental band gap of GaAs, which features an energy almost 400 times higher than the terahertz photon energy. Massive carrier multiplication by impact ionization made visible by bright and spectrally broad photoluminescence attests to highly accelerated electrons owing to ponderomotive potentials in the keV-range.

When subjected to an external magnetic field, the density of states of electrons in a two-dimensional electron gas (2DEG) condenses on certain energy levels, which may classically be connected to distinct, collective cyclotron orbits of the electrons. The equidistant energy spacing between these so-called Landau-levels can be shifted into the terahertz spectral range by adjusting the external field. Inter-Landau-level transitions may thus be driven by resonant excitation with terahertz pulses. Despite their many-body character, the cyclotron resonances have long been thought of as being independent of the Coulomb interaction between the huge number of carriers [Koh61]. Non-perturbative excitation with strong terahertz fields from the novel setup described above has recently shown, however, that anharmonic Landau ladder climbing and pronounced four- and six-wave mixing signals can be observed, which are only explicable by taking into account the Coulomb interaction of the electrons with the ionic background in the 2DEG [Maa16]. These observations open the door towards novel quantum control schemes on ultrafast time scales [Maa16].

The quest for ever faster control schemes of the magnetic moment in solids has established the field of *femtomagnetism*. In 2011, the most direct way to selectively excite spin dynamics in magnetically ordered materials without influencing other degrees of freedom like electronic transitions has been demonstrated: The direct Zeeman coupling of the magnetic field component of phase-stable terahertz waveforms with the spin in antiferromagnetic nickel oxide enables resonant excitation and coherent control of collective magnon modes which can directly be traced in the time domain by ultrafast Faraday rotation [Kam11]. With peak magnetic fields of up to 0.4 T from the new terahertz source

and its improved signal-to-noise characteristics, it is now possible to even enter the nonlinear regime of all-magnetic terahertz spin control: Distinct nonlinearities like a second harmonic signal in the Faraday traces have been observed for the first time [Bai16]. These findings may open up new routes towards ultrafast magnetic switching.

2.2 Setup for time-resolved lightwave electronics in the multi-THz range

The broadband spectral range from 10 - 100 THz includes far- and mid-infrared wavelengths, which are of huge interest for fundamental research as well as for technological achievements, e.g., in security applications, gas sensing or high-order harmonic generation. The terminology "multi-terahertz" not only comprises these spectral regions but usually includes two additional and essential aspects: phase-stability and field-resolution of the employed ultrashort waveforms. The enabling technologies of phase-locked generation and field-resolved detection of terahertz transients have made terahertz time-domain spectroscopy a story of success. Extending these concepts step by step towards higher frequencies, they already approach the near-infrared region nowadays [Wu97, Hub00, Küb04, Zen07, Sel08a, Kei16]. On the other hand, a strong motivation to effectively generate short pulses in the mid-infrared range has arisen from the area of strong-field light-matter interaction, which has mainly been based on the use of near-infrared or visible optical pulses so far. The reasons for these efforts [Wol15] are a gain in ponderomotive potentials accompanied by a decrease in photon energies when using longer wavelengths. Both trends are favourable for well-defined strong-field control of electron dynamics [Sch14b, Hoh15a] and in particular for ballistic processes like electron acceleration [Bre13, Wim14] or high-order harmonic generation in gases [Cor07, Wol15]. The following paragraphs will give an overview on the second beamline of the terahertz high-field laboratory (compare figure 2.1), which might be capable of closing this gap between ultrafast strong-field light-matter interaction on the high-frequency side and time-resolved terahertz control of electron dynamics on the low-frequency side.

2.2.1 Ultrashort white-light pulses as a sub-cycle probe

For both field-resolved detection of multi-THz waveforms and probing terahertz-induced dynamics on a sub-cycle time scale, ultrashort pulses with durations much shorter than one oscillation cycle of the terahertz transients are crucial. To this end, a supercontinuum source based on filamentation in yttrium aluminium garnet (YAG) has been developed, which delivers octave-spanning spectra in the near-infrared and visible spectral ranges. The process of supercontinuum generation in solids relies on the complex interplay of

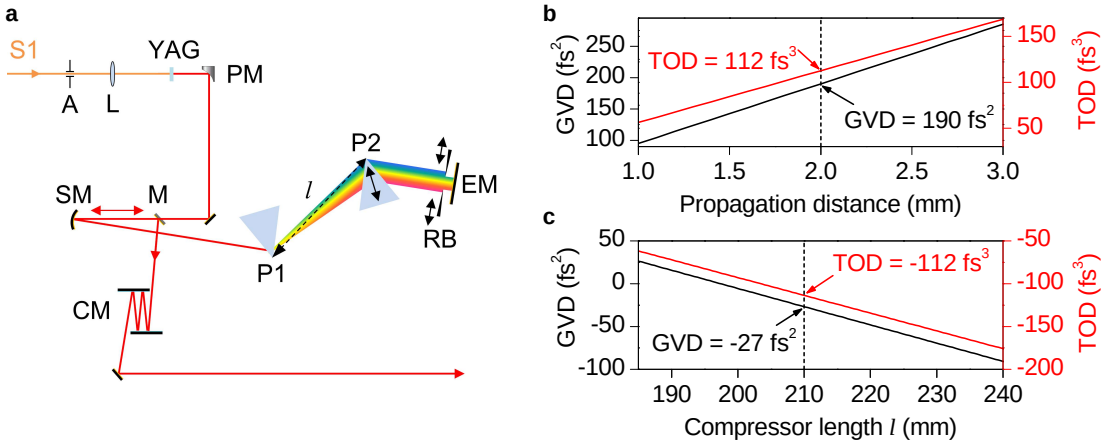

Figure 2.6: White-light source and compressor: a, Simplified sketch of the setup. S1: signal pulses from one of the optical parametric amplifiers, A: iris aperture, L: lens, YAG: yttrium aluminium garnet, PM: parabolic mirror, SM: spherical mirror, P1, P2: fused silica prisms, l: compressor length, RB: razor blades, EM: end mirror, M: pick-off mirror, CM: chirped mirror pair. **b,** The calculated second (third) order dispersion for a wavelength of 820 nm as a function of the propagation length in YAG is shown as a black (red) curve. **c,** The black (red) curve shows the calculated second (third) order dispersion collected during a double pass sequence through the prism compressor (as shown in panel a) as a function of the compressor length l for an average material passage of 3 mm per prism. Underlying refractive index data for fused silica and YAG has been taken from [Mal65] and [Bas09], respectively.

different nonlinearities and strong-field light-matter interactions, which shall only be briefly mentioned here. Extensive and detailed discussions of the topic can be found in [Alf06, Cou07, Ber07], for instance.

When a femtosecond laser pulse is tightly focused into a transparent solid (note that supercontinuum generation is not limited to solids, in principle), the third-order nonlinear effect of an intensity-dependent refractive index can lead to both spectral broadening by self-phase-modulation and a further enhancement of the peak intensity by self-focusing. Subsequent self-steepening of the pulses and finally ionization lead to the buildup of a plasma in the material, which counteracts the effect of self-focusing. A dynamic equilibrium between the focusing and de-focusing effects results in the formation of a very narrow plasma tube in the material, the so-called filament. The enormous spectral broadening which accompanies these effects can be exploited to produce white-light pulses featuring octave-spanning spectral bandwidths.

Here, a small portion (pulse energy of 3 µJ) of one of the signal outputs of the optical parametric amplifiers, usually operated at a centre wavelength of 1200 nm, is focused into a monocrystalline YAG window with a thickness of 4 mm (see figure 2.6a). Using

the OPA's signal pulses instead of the pump pulses from the titanium-sapphire amplifier helps to reduce the propagation length of both white-light and terahertz pulses between generation and experiments. Potential timing jitter between the two branches is thus significantly reduced as compared to a white-light source based on the use of the amplifier output, which would require additional delay lines in order to compensate for the beam path within the OPA. Together with a very compact and stable setup, this renders any active synchronization scheme or jitter compensation unnecessary. Instead of sapphire, which is the most common material for femtosecond continuum generation, YAG has been chosen here due to its capability of generating relatively broadband and smooth spectral plateaus in the short-wavelength region [Bra09] (compare also figure 2.7a). An adjustable iris aperture is used to tune the pump pulse energy and the focusing conditions (see figure 2.6a). After collimation of the generated continuum by a parabolic mirror, the white-light pulses are guided through a double-pass prism compressor: A spherical mirror focuses the beam through two fused silica prisms onto a planar retroreflector placed in the focal plane. Following the same path through the prisms in the opposite direction with a slight vertical offset, the re-collimated beam is picked off after the spherical mirror. Two horizontally adjustable razor blades in the Fourier plane of the compressor in front of the end-mirror are used to select the desired spectral range finally used in the experiments.

The prism compressor itself is capable of compensating the second-order dispersion [Die06], the so-called group velocity dispersion (GVD), which has initially been imprinted on the short pulses during propagation through the YAG window. For most applications, this already permits adequate re-compression to sub-10-fs pulse lengths [Sch14a]. Tuning the interplay between material dispersion in the prisms and varying optical path lengths of different wavelengths (see figure 2.6a) is not sufficient to adjust both the second- and third-order dispersion (TOD) independently, however. As shown in appendix A, the remaining TOD can lead to pronounced pre- or post-pulses. For sub-cycle experiments as introduced in chapters 4 and 5, it becomes essential to probe dynamics with a temporal resolution better than one half-cycle of the driving multi-THz waveforms. The satellite pulses stemming from remaining TOD may lead to significant overlap of probe pulse intensity with the preceding or the subsequent half-cycle. Therefore, the prism compressor had to be extended towards a more flexible solution. In order to define the requirements for the compressor, the dispersion which is imprinted on the white light pulses during propagation through the YAG window may be estimated. To this end, the GVD as well as the TOD for pulse propagation from the focal plane of the pump pulses in the YAG window to its end facet, i.e., for a distance of approximately 2 mm, is calculated (figure 2.6b). Despite its usual purpose of compensating the GVD, the new prism assembly has been designed to form a nearly zero-dispersion compressor

and to approximately compensate the third-order dispersion only. Figure 2.6c shows the calculated dispersion of second- and third-order for the prism compressor shown in panel a with an average material passage of 3 mm per prism as a function of the compressor length l. After compensating the TOD in the prism sequence, the remaining GVD of approximately 160 fs^2 is additionally removed by four reflections from a suitable chirped mirror pair, compensating a GVD of -40 fs^2 per bounce without significantly changing the TOD.
Figure 2.7 summarizes the spectral and temporal characteristics of the white-light pulses which have been generated and compressed as explained above. The broadband short-wavelength plateau generated in YAG extends from the pump spectrum centred at $\lambda_P = 1200$ nm to 450 nm and covers more than one optical octave. Note that the spectrum shown in figure 2.7a has been recorded after passage through the chirped mirror compressor, whose reflection range sets the short wavelength roll-off here. For the experiments described in the subsequent chapters, a spectral range from approximately 750 nm to 925 nm has been selected by blocking both shorter and longer wavelengths in the Fourier plane of the prism compressor (compare figure 2.6a). A second-harmonic FROG recording[3] as shown in figure 2.7b enables a full reconstruction (spectrogram in figure 2.7c) of the intensity envelope (panel e) of the compressed pulse as well as its spectral phase (panel d). The ultrashort supercontinuum pulses exhibit an intensity full-width at half-maximum of only 8 fs, while their temporal shape is very smooth and features only very minor pedestals containing less than 4% of the pulse energy of 3.5 nJ measured after the compressor. These ultrashort and broadband pulses serve as an ideal tool to electro-optically detect phase-locked waveforms up to frequencies in the mid-infrared spectral range and will allow to resolve strong-field-induced charge carrier dynamics with an accuracy of only a fraction of one single multi-terahertz oscillation cycle (see chapter 4).

2.2.2 Atomically strong and phase-controlled multi-THz waveforms

Carrier-envelope offset-free difference frequency generation

Optical rectification has proven to be the means of choice for all-optical terahertz generation in the regime below 10 THz. While OR is in principle also suitable for the generation of higher frequencies in the multi-THz range, its quantum efficiency is intrinsically limited - a fact that can easily be understood when describing optical rectification as difference frequency generation (DFG) within a broad spectrum: For a given pump pulse featuring, e.g., a Gaussian spectral shape, the highest possible terahertz frequency is given by the difference between the highest and the lowest frequency contained in this

[3] **F**requency-**R**esolved **O**ptical **G**ating [Kan93], see also section 4.1.1.

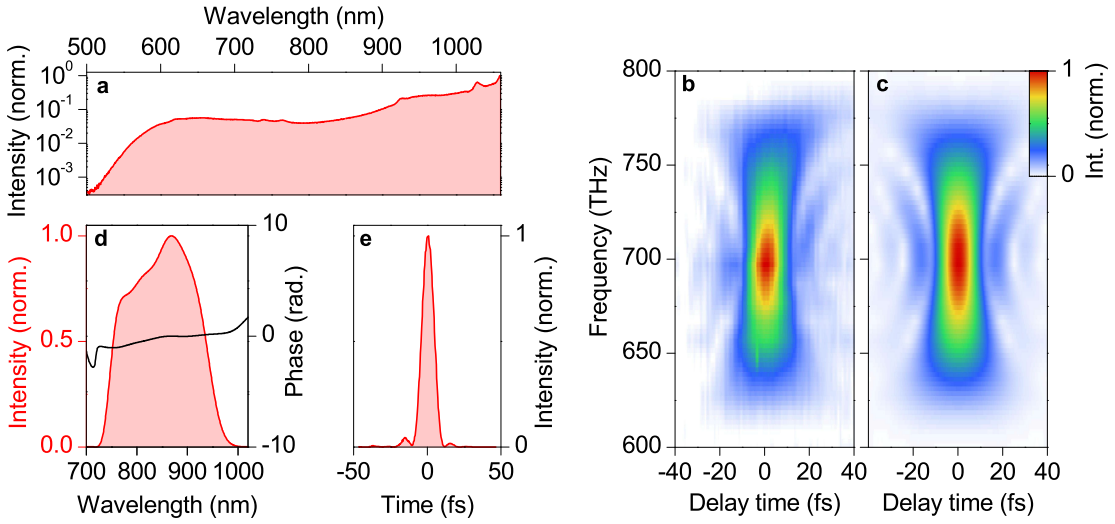

Figure 2.7: Spectral and temporal characterization of ultrashort white-light pulses: a, Short-wavelength plateau of an octave-spanning white-light pulse as detected with a spectrograph and a silicon CCD after the compressor shown in figure 2.6. The high-frequency roll-off is limited by the reflectance range of the employed chirped mirrors here. **b,c,** Measured (b) and reconstructed (c) spectrograms of a second-harmonic FROG recording of the compressed and spectrally tailored white-light pulses. **d,** Reconstructed intensity spectrum (red) and spectral phase (black) of the compressed pulses. **e,** Reconstructed temporal intensity envelope featuring an intensity FWHM of only 8 fs, a smooth shape and only very minor pre- and post-pulses.

spectrum. The spectral intensity within these flanks is always reduced compared to the central wavelengths. The quantum efficiency of OR consequently decreases for higher terahertz frequencies. Difference frequency generation between two pulses, which are spectrally detuned by the desired multi-THz frequency, circumvents this limitation and facilitates the generation of higher pulse energies and larger peak fields in the multi-terahertz range.

If the two pulses used for DFG are phase-correlated, i.e., they exhibit the same pulse-to-pulse phase slip, the generated pulse at the difference frequency will be inherently phase-stable, as it is the case for OR. The Fourier transform of a train of ultrashort pulses from a mode-locked laser is composed of equidistant, discrete lines

$$\nu_\mathrm{n} = n \cdot \nu_\mathrm{rep} + \nu_\mathrm{CEO} \tag{2.5}$$

spaced by the repetition rate ν_rep which form the so-called frequency comb. The first comb line marks the so-called carrier-envelope offset (CEO) frequency ν_CEO, which describes the pulse-to-pulse phase-slip $\Delta\phi_\mathrm{CEP} = \pi \cdot \nu_\mathrm{CEO}/\nu_\mathrm{rep}$ of the carrier wave with respect to its envelope. The difference frequency of two of these frequency combs (indi-

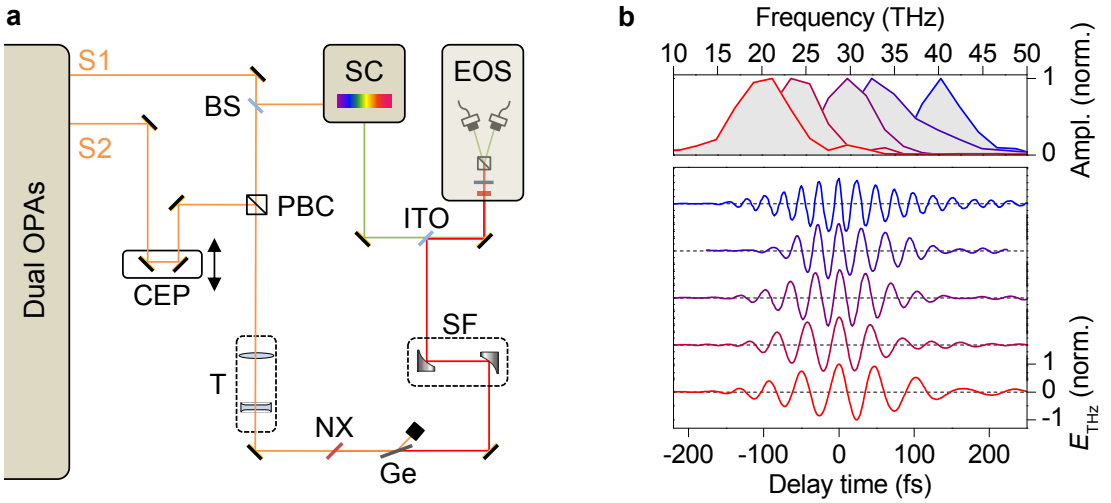

Figure 2.8: Generation and field-resolved detection of strong multi-THz waveforms: a, Simplified sketch of the multi-THz generation scheme. S1, S2: signal pulses of the two optical parametric amplifiers, BS: beam splitter, CEP: variable mechanical delay for carrier-envelope phase adjustment, PBC: polarizing beam splitter cube, T: telescope, NX: nonlinear crystal, Ge: germanium filter, SF: sample focus or customized measurement setup (see, e.g., figure 4.1), ITO: indium tin oxide coated beam splitter, SC: supercontinuum source, EOS: electro-optic sampling. **b,** Electro-optic traces of multi-THz waveforms (lower panel) featuring centre frequencies between 20 THz (red) and 40 THz (blue). The associated spectra are shown in the upper panel in corresponding colours.

cated by upper indices (1) and (2)) with the same repetition rate will be composed of the differences between the comb lines and the carrier-envelope offsets [Die06]:

$$\nu_{\mathrm{DFG}} = (n^{(1)} - n^{(2)}) \cdot \nu_{\mathrm{rep}} + (\nu_{\mathrm{CEO}}^{(1)} - \nu_{\mathrm{CEO}}^{(2)}) \tag{2.6}$$

If the CEO is the same for both pulses, it exactly vanishes for the generated difference frequency comb, yielding CEP-stable waveforms ($\Delta\phi_{\mathrm{CEP}} = 0$).
In addition to the passive CEP-stability, the DFG process enables precise control of the phase of the generated transients, which is given by $\phi_{\mathrm{DFG}} = \phi^{(1)} - \phi^{(2)} + \pi/2$, where $\phi^{(1)}$ and $\phi^{(2)}$ are the phases of the two near-infrared pulses [Bal02]. Changing one of the phases, e.g., by temporally delaying the pulses with respect to each other, thus directly influences the carrier-envelope phase of the generated waveforms.

The multi-THz high-field source - experimental setup

The multi-THz source is based on difference frequency generation between two spectrally detuned near-infrared pulse trains [Sel08a, Sch14a] delivered by two parallel optical

parametric amplifiers (compare figure 2.1), as depicted schematically in figure 2.8a. After rotating the polarization of the low-frequency signal branch (S2) in order to fulfil the requirements for type-II phase matching in the DFG process, both signal pulses from the OPAs are superimposed collinearly using a polarizing beam splitter cube and temporally overlapped by a mechanical delay stage. A lens telescope reduces the beam diameter for maximum efficient frequency conversion in the nonlinear crystal. Remaining pump light is filtered after the DFG process by a germanium waver which is put into the beam path under the Brewster angle for the generated multi-THz pulses, before the high-field transients may be exploited in a sample focus or customized experimental setup (see different experiments described in chapters 3 to 5). Ultrashort gating pulses retrieved from supercontinuum generation as described in section 2.2.1 are superimposed with the field transients for balanced electro-optic detection.
The multi-THz source is capable of delivering pulse energies in the mid-infrared of up to 30 µJ and record peak field strengths on the order of 100 MV/cm [Sel08a, Sch14a]. In addition, the DFG-based generation scheme offers uniquely flexible tuning possibilities: By changing the central wavelengths of the employed near-infrared pulse trains as well as the phase matching angle in the nonlinear crystal, the centre frequency of the generated waveforms can easily be adjusted [Sel08a]. While the lower limit of approximately 10 THz is set by the reststrahlen band of commonly used nonlinear materials, frequencies of up to 100 THz or even more should be achievable [Sel08a]. Figure 2.8b shows some typical few-cycle waveforms, which have been generated in a gallium selenide crystal of a thickness of 430 µm and feature centre frequencies between 20 and 40 THz. The pulse length of roughly 100 fs (intensity FWHM) is mainly determined by the duration of the employed signal pulses and consequently stays approximately constant for the variation of the centre frequency shown here. Changing the pre-chirp of the white-light seed within the dual-OPA [Sch14a] will permit the generation of even shorter pulses in the single-cycle regime [Jun10]. Furthermore, tuning the delay between the two signal branches precisely adjusts the carrier-envelope phase [Sch14a] of the generated high-field traces, which opens up unique perspectives for sub-cycle coherent control [Sch14b, Hoh15a] and photonic applications like pulse shaping on a sub-cycle time scale (see, e.g., figure 4.15). These features render the multi-THz source a perfect tool for high-field terahertz control of charge carrier dynamics and lightwave-driven electronics (chapters 3 to 5).

Chapter 3

High-order harmonic generation: from gases to bulk solids

High-order harmonic generation (HHG) has opened up new routes in ultrafast photonics and enabled novel spectroscopic techniques, accompanied by a gain in the basic understanding of strong-field light-matter interaction. In the following chapter, a brief overview on HHG in different systems and regimes shall be given. A classification of distinctive HHG schemes in different media and in terms of the underlying mechanism is followed by a short synopsis on recent achievements and applications of HHG. Before the latest field of HHG in bulk solids comes into focus, a short description of the underlying generation mechanism in atoms and molecules is given. Finally, new findings on terahertz-driven HHG in the frequency domain are reviewed, which have been gathered here, published in reference [Sch14b] and described in more detail in reference [Sch14a].

Optical harmonic generation generally describes a process where an intense laser beam, i.e., an electromagnetic wave E of a given, so-called fundamental frequency ν, interacts with matter in a nonlinear way such that radiation at multiples of the fundamental frequency $\nu_{\mathrm{HH}} = n \cdot \nu$ is emitted - the so-called harmonics. The first experimental detection of optically generated radiation at twice the incoming laser frequency has been reported by Franken and co-workers already in 1961 [Fra61]. This observation of the second harmonic of a laser beam can be seen as the starting point of the revolutionary development of perturbative nonlinear optics, without which modern photonics cannot be imagined today. Under the assumption that the optical field does not change the system in a substantial way, the induced nonlinearities may be theoretically described in perturbation theory. These effects can then be well-understood within a series expansion

of the macroscopic optical polarization in the material [Boy03]:

$$P(E) = \chi^{(1)}E + \chi^{(2)}E^2 + \chi^{(3)}E^3 + \dots \tag{3.1}$$

Terms in this series scaling with power n in E may lead to the generation of the n-th harmonic. As a consequence, the harmonic intensity of n-th order is expected to scale like $I_{\mathrm{HH}} \propto E^{2n}$ with the driving field. Strongly decreasing nonlinear coefficients $\chi^{(n)}$ furthermore lead to very rapidly abating intensities of emitted harmonics with growing order n.

A completely new and different class of nonlinearities has been made accessible by the development of efficient sources of intense and ultrashort laser pulses [Bra00]. When optical electromagnetic fields in such few-cycle pulses become strong enough, their interaction with matter may no longer be regarded as a small perturbation - a distinction which defines the group of so-called non-perturbative nonlinearities. This strong-field regime of light-matter interaction has gained huge interest during the past decades, not least because of non-perturbative HHG, which finds a wealth of applications as described below. The first high-order harmonic (HH) signal, which may be assigned to this non-perturbative regime, has been detected as emitted light from a laser-induced plasma on the surface of a solid aluminium sample [Bur77]. This technique has been revived during the last years for efficient HHG at so-called plasma mirrors using low-repetition-rate but high-power (Tera- to Petawatt) laser facilities [Dro06, Tha07, Nom09]. Nevertheless, the most prominent and widely proliferated way of producing HH is based on the use of atomic or molecular gases as the interaction medium. This approach enables the generation of extremely broadband radiation up to the extreme ultraviolet (XUV) spectral range and even the soft X-ray regime [Ser05] based on comparably compact table-top laser sources. A variety of spectroscopic techniques including XUV-, photon-emission- or XMCD[1]-spectroscopy have immensely benefited from the achievable high photon energies. On the other hand, HHG in gases has enabled the production and use of the shortest laser pulses possible so far and forms the backbone of attosecond science [Cor07, Chi14, Kra14]. In addition, analysing emitted high-harmonics has successfully been used to probe the structure of atoms and molecules as well as to infer the underlying electronic dynamics [Dre02, Gou07, Sha09, Smi09].

Quite recently, the concept of exploiting few-cycle, intense waveforms to drive HHG has been transferred to bulk solids. In a seminal experiment, Ghimire and co-workers demonstrated that HHG can be driven in zinc oxide and high-order harmonics up to an order $n = 25$ with photon energies above the fundamental band gap of the material may

[1] Acronym for *X-ray Magnetic Circular Dichroism*

be observed [Ghi10]. The authors proved the non-perturbative character of the driving mechanism by showing a clear deviation from a perturbative scaling of the emitted HH intensity with the applied driving field strength E as given in equation (3.1). While potential applications or a precise understanding of the complex underlying mechanism may have been regarded as to be far away, this demonstration can surely be seen as the starting point of a rapid development during the last years keeping up with new experimental and theoretical studies on solid-state HHG (see chapter 4).

3.1 Underlying microscopic generation mechanisms

In contrast to the perturbative regime, where the macroscopic polarization describes how bound electrons are weakly deflected from their equilibrium positions under the influence of the external electric field E, a model of non-perturbative HHG has to deal with ionization effects and strong-field-driven acceleration of quasi-free electrons. For atoms and molecules, the underlying dynamics are well-understood and can be described sufficiently in an intuitive semiclassical model. This so-called three-step model was put forth more than 20 years ago [Cor93, Lew94] and has been proven to correctly predict a row of characteristics intrinsic to atomic HHG [Cor07, Chi14, Kra14], which shall briefly be discussed in the following.
For a simplistic picture, one may consider a single electron in real space, which is bound to an ion core via the atomic Coulomb potential, as illustrated in figure 3.1a. The strong, linearly polarized electric field of the applied optical pulse drives three subsequent processes (compare figure 3.1a, b):

(1) **Ionization:** The Coulomb potential gets massively modified by the strong light field, allowing the electron to tunnel into the continuum of states.

(2) **Acceleration:** Still subjected to the strong electric field, the free electron gets accelerated away from the ion core and cumulates kinetic energy which is given by the ponderomotive potential

$$U_\mathrm{P} = \frac{eE^2}{4m(2\pi\nu)^2}, \tag{3.2}$$

where e defines the electron's charge and m its mass.

(3) **Recollision:** When the sign of the driving field changes, the electron gets decelerated and finally inverts its direction of motion. Driven back to its mother core, it may eventually recollide with the positively charged ion, thereby releasing its excess kinetic energy via emission of high-frequency photons - the high-harmonic radiation.

A typical HH intensity spectrum from gases, as schematically illustrated in figure 3.1c, exhibits some characteristic features which can be well-understood within the intuitive semiclassical picture. Since atomic or molecular gases are inversion-symmetric on macroscopic length scales, there is no field direction which would be favourable for the process of HHG. High-harmonics will consequently be emitted during every half-cycle of the driving wave, resulting in the appearance of odd harmonic orders only (see also chapter 4 and 5). A rapidly decaying intensity of the lowest orders reflects the perturbative regime of harmonic generation. A subsequent plateau-like region in the spectrum is a hallmark for the non-perturbative character of HHG and can be explained by an interplay of different electron pathways during the acceleration phase which may lead to the same emitted photon energies at the recollision. These so-called long and short trajectories can be understood by looking into the three-step sequence on a sub-cycle time scale: As evident from the description above, the probability of an electron recolliding with the ion core will sensitively depend on several quantities. First and foremost, the exact phase of the driving field at the time of ionization will decide whether the electron is set on a recollision path or will simply be driven away without turning back to its ion core. The maximum gain in kinetic energy is reached if the ponderomotive force applied by the driving field half-cycle, which precedes the recollision, is maximized. For a continuous wave excitation, an assumption which might be justified for few-cycle pulses where the envelope changes on a much slower time scale than the driving field, this maximum recollision speed is reached for an ionization at a phase of 17° after a crest of the light wave (trajectory 'l' in figure 3.1b). The highest photon energy released for this maximum efficient trajectory defines the so-called cut-off frequency [Cor93] (see figure 3.1c)

$$h\nu_{\mathrm{cutoff}} = U_{\mathrm{ion}} + 3.17 \cdot U_{\mathrm{P}}, \tag{3.3}$$

where U_{ion} is the ionization potential of the bound electron. Trajectories starting at earlier ionization times feature larger maximum deflections and later recollision times and are called long trajectories, whereas the ones starting later and ending earlier are named short trajectories [Mai03]. While the cut-off energy is only reached for the most efficient trajectory, lower photon energies may be emitted twice per driving half-cycle, once for the corresponding short trajectory and once for the long one. In summary, the ballistic acceleration of electrons during atomic HHG leads to a characteristic delay between the driving field extrema and the peak of HH emission. Additionally, this delay depends on the HH photon energy, leading to the so-called *atto-chirp* [Chi14] as an inherent property of high-order harmonics from gases.

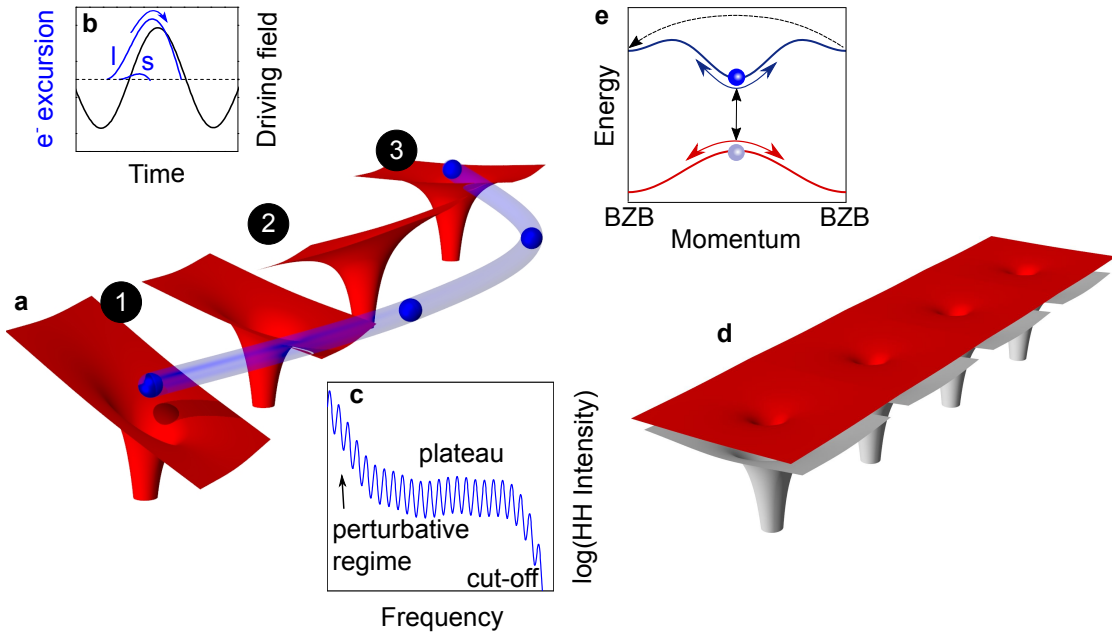

Figure 3.1: Driving mechanisms of high-order harmonic generation: **a,** Schematic illustration of the three-step model explaining HHG in atoms and molecules. A single electron (blue sphere) is initially bound to the atom core via the Coulomb potential (depicted in red). A strong lightwave may ionize (1) the atom, accelerate (2) and subsequently recollide (3) the electron with the ion core after sign reversal of the electric light field. **b,** Schematic of the electron's deflection (blue) for two different ionization times relative to the phase of the driving field (black). l: long trajectory; s: short trajectory. **c,** Typical HH spectrum from gases with a perturbative regime for low frequencies, a plateau-like intermediate region and a sharp cut-off at the highest reachable photon energies. **d,** Illustration of the continuous potential landscape (red) in a solid formed by the Coulomb potentials (grey) of the periodically arranged ion cores. **e,** Simplified band structure of a semiconductor with one valence band (red) and one conduction band (blue). Electrons may be promoted to the conduction band (black arrow) under a strong external light field, while generated electrons and holes are simultaneously accelerated (blue and red arrows). Once the electron reaches the Brillouin zone boundary (BZB), it enters the Brillouin zone from the other side again (dashed arrow), giving rise to Bloch oscillations.

HHG driving mechanism in bulk solids

In contrast to atomic HHG, the understanding of its solid-state counterpart is still in its infancy. Transferring concepts of the three-step picture of HHG in gases to the case of solid-state high-order harmonic generation may help as a starting point for framing an intuitive model and to find useful analogies. In a bulk semiconductor, valence electrons can be compared to the Coulomb-bound electrons in atomic potentials. A strong light

field may also ionize this electron, i.e., promote it to a higher lying energy level.
An estimate of the strong-field-driven deflection of a quasi-free crystal electron renders the atomic acceleration scenario questionable, however: For realistic internal peak field amplitudes of 40 MV/cm at a driving field frequency of 30 THz, equation (3.2) yields ponderomotive energies on the order of 20 eV and maximum electron deflections on the order of 20 nm, i.e., tens of lattice constants of a typical solid. In a periodic crystal lattice, electronic states of neighbouring ions are combined to form electronic bands (see schematic illustration in figure 3.1d, e). Electrons may no longer be described as spatially localized carriers but their wave functions are extended over the whole crystal lattice. As a consequence, their quantum-mechanical wave nature will dominate high-field driven charge transport in bulk semiconductors. A convenient way to describe the dynamics of delocalized Bloch electrons in solids is given in reciprocal space, where the electron's motion is governed by the dispersion of electronic bands $\mathcal{E}(k)$ (see figure 3.1e). A description of the intraband dynamics of a quasi-free crystal electron under the influence of a constant electric field E_{DC}, which was derived by Felix Bloch more than 85 years ago [Blo29], leads to the conclusion that an electron will be driven through the band with a constant rate of its wave vector k [Zen34]:

$$\hbar\dot{k} = -eE_{\mathrm{DC}} \tag{3.4}$$

Neglecting any scattering channels, for the moment, this equation implies that the electron reaches the boundary of the Brilloiun zone (BZB), enters it from the other side in the reduced zone scheme (black dashed arrow in figure 3.1e) and traverses the whole Brillouin zone again. This oscillatory motion in reciprocal space directly translates into real-space oscillations, although the external field is assumed to be constant and unidirectional here. This absolutely fascinating and counter-intuitive phenomenon was named Bloch oscillations and has been extremely challenging to observe experimentally. The reason for these difficulties is the invalid assumption to neglect scattering of the accelerated electron. Once the electron scatters, its momentum is changed and it is precluded from reaching the Brillouin zone boundary. An estimate of the required experimental conditions can be derived[2] from the Bloch period $\tau_{\mathrm{B}} = 1/\nu_{\mathrm{B}}$:

$$\tau_B = \frac{h}{aeE} \tag{3.5}$$

Typical scattering times on the order of $\tau_{\mathrm{scatter}} = 10\text{ - }100$ fs in bulk semiconductors [Lei99, Su09, Hir11b] require electric field strengths on the order of several 10 MV/cm or arti-

[2] The formula given here is valid for cubic lattices, where the full width of the first Brillouin zone amounts to $4\pi/a$ with the lattice constant a.

ficially increased lattice constants a in order to fulfil $\tau_{\mathrm{B}} \lesssim \tau_{\mathrm{scatter}}$, which is necessary to observe a full Bloch oscillation before scattering destroys the coherence [Fel92, Ros02]. Replacing the constant electric field E_{DC} by an oscillating lightwave E leaves most of the results above unchanged but implies that carriers are driven back and forth in the Brilloiun zone following the fundamental frequency ν of the driving field. When the field is sufficiently strong to displace carriers to the BZB within a single half-cycle of the driving field, the harmonic carrier motion will be strongly distorted due to so-called dynamical Bloch oscillations, leading to the emission of high-frequency radiation detectable as high-order harmonics. Furthermore, even anharmonicities in the electronic bands within the Brillouin zone already translate into a distortion of the harmonic carrier motion. On top of this, the direction of motion of crystal electrons is changed whenever the sign of their effective mass changes. Since the latter is proportional to the curvature of the electronic dispersion $\frac{\partial^2}{\partial k^2}\mathcal{E}(k)$, inflection points in $\mathcal{E}(k)$ further enhance the emission of higher frequencies.

A complementing possible driving mechanism of HHG in solids has been neglected in the derivation so far. The interband excitation leading to a carrier population in the conduction band is not only a prerequisite for high-field driven intraband charge transport but may also contribute significantly to high-order harmonic generation. Similar to atoms, a strong light field may promote electrons from the valence into the conduction band via Zener tunneling or multi-photon processes. A strong mutual coupling of coherent interband polarization and simultaneously driven intraband acceleration during terahertz-driven HHG in bulk solids was already predicted theoretically in 2008 [Gol08]. An experimental evidence or a way to disentangle both contributions has been missing, however.

3.2 Terahertz-driven high-order harmonic generation in gallium selenide

Here, multi-THz transients with atomic field strengths have been employed to drive HHG in the bulk semiconductor gallium selenide. A delicate combination of coherent interband excitation and simultaneous carrier acceleration within the bands results in the emission of record-bandwidth, inherently phase-locked HH spectra which cover more than 12 optical octaves. A many-body quantum theory developed by the groups of Mackillo Kira and Stephan W. Koch in Marburg (see section 4.3.1) explains even faint details in the spectral emission properties and suggests dynamical Bloch oscillations along with non-resonantly driven, coherent interband polarization as the underlying microscopic generation mechanism. These findings were published in a joint study in

reference [Sch14b]. A detailed examination of the experiment can be found in the dissertation [Sch14a], which is why only a brief review on the most important findings shall be given here, based on references [Sch14b] and [Hoh15b].
Gallium selenide (GaSe) is a layered III-VI compound consisting of van-der-Waals bound layers which are composed of two gallium (Ga) sheets sandwiched in-between two rows of selenium (Se) atoms (see chapter 5.1). The semiconductor is one of the most commonly used materials for nonlinear frequency conversion throughout the near- and mid-infrared spectral range due to its highly beneficial optical properties, i.e., a large transmission range and relatively high nonlinear coefficients. GaSe is supposed to be particularly well-suited for high-field studies of intraband charge transport, since it features comparably narrow conduction bands with respect to its fundamental band gap energy $E_\mathrm{g} = 2\,\mathrm{eV} = h \cdot 476\,\mathrm{THz}$, rendering impact ionization as an unwanted scattering channel less serious. High-field multi-THz waveforms as delivered by the source described in section 2.2.2, featuring a centre frequency of 30 THz and peak electric field strengths of 72 MV/cm in air (figure 3.2a), are focused down onto an undoped, single-crystalline GaSe window. The thickness of the cleaved sample has been determined to be 220 µm. Electro-optic sampling of the transmitted waveform after the sample reveals a drastic distortion of the field trace directly visible in the time domain (figure 3.2b): An asymmetric shape with respect to the sign of the field as well as high-frequency components attest to strong nonlinearities during interaction with the GaSe sample. The amplitude spectrum shown in panel c indeed confirms both spectral components at the second harmonic, i.e., around 60 THz, as well as low-frequency signatures around 0.1 THz stemming from optical rectification of the multi-THz transients. These very intriguing field-resolved nonlinearities may still be described within a perturbative model of nonlinear optics. However, broadband electro-optic traces yield intensity spectra of emitted waveforms which unravel even spectral signatures at the third and fourth harmonic order (blue shaded curve in figure 3.2d). Switching to time-integrated detectors, i.e., grating spectrographs equipped with an indium gallium arsenide detector array and a cooled silicon CCD (*charged coupled device*) camera, respectively, surprisingly uncovers an extremely broadband HH spectrum. Showing a distinct modulation with a periodicity corresponding to the fundamental driving frequency, the spectrum contains both even and odd order harmonics up to the 22^{nd} order extending even above the fundamental band gap of GaSe, where strong interband absorption sets in (band gap energy marked by the black arrow in figure 3.2d). The single pulse train encompasses spectral components ranging from 0.1 THz to the detection limit at 675 THz and spans more than 12 optical octaves, including the terahertz, far-, mid-, and near-infrared range as well as the whole visible regime. A plateau-like region in the spectra below the band gap is indicative of a non-perturbative driving mechanism. Furthermore, the scaling of the HH intensity of

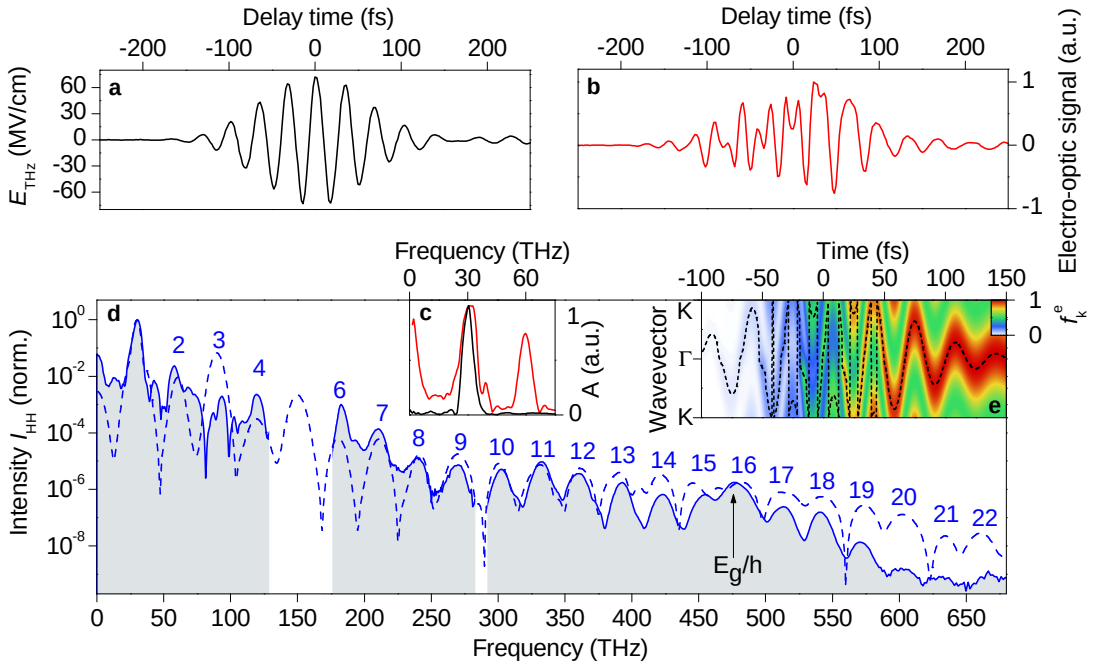

Figure 3.2: Frequency domain study of high-order harmonic generation in bulk gallium selenide: a, Multi-THz driving field featuring a centre frequency of 30 THz and peak electric field strengths of 72 MV/cm in air. **b,** Electro-optic trace of the waveform after transmission through a 220-µm-thick gallium selenide sample. **c,** Amplitude spectra of the waveforms shown in panel a (black) and b (red). **d,** The blue shaded area depicts a typical high-order harmonic intensity spectrum driven by the waveform shown in panel a, as detected electro-optically (below 120 THz) and recorded with grating spectrometers equipped with an indium gallium arsenide detector array (below 280 THz) and a cooled silicon CCD camera, respectively. The dashed blue line shows the calculated HH intensity spectrum, which has been numerically simulated based on a quantum-mechanical many-body theory (compare section 4.3.1). **e,** Colour-coded representation of the simulated electronic occupation f_k^e of the first conduction band within the first Brillouin zone. The black dashed curve highlights the centre of mass of the electron distribution.

different orders with the driving field strength (not shown here, compare figure 4.11) shows a pronounced deviation from the perturbative power law given in equation (3.1). A huge amount of carriers promoted to the initially empty conduction bands can be anticipated from the strong photoluminescence peak at the band gap energy. Remarkably, electro-optic sampling of the lowest orders and subsequent f-$2f$-interferometry (not shown, see [Sch14b]) within the ultrabroadband HH frequency comb prove inherent phase-stability of all spectral components.

While one may already infer an all-coherent and non-perturbative driving mechanism from these characteristics, a sophisticated theory is needed to gain a deeper understand-

ing of the microscopic dynamics. To this end, a quantum-mechanical many-body theory taking into account both the interband carrier creation as well as the simultaneously driven intraband high-field transport within five electronic bands of GaSe based on the model developed in references [Gol08, Gol11] has been customized to the experiment (see section 4.3.1 for details on the numerical model). Given the enormous bandwidth, the theory reproduces the experimentally recorded HH spectrum remarkably well (theoretical spectrum shown as a dashed blue curve in figure 3.2d). Promoted to the conduction band via coherent interband polarization, the electrons are strongly accelerated through the whole Brillouin zone, as evident from figure 3.2e: The simulated dynamic occupation of the first conduction band f_k^{e} for a peak internal driving field of 14 MV/cm shows that the electron distribution gets enhanced step by step at the driving field crests and is deflected to higher momenta at the same time. For highest peak fields, not only the tales of this envelope function but even its centre of mass (as highlighted by the black dashed curve in figure 3.2e) reaches the Brillouin zone boundary twice during one driving half-cycle, where it gets Bragg-reflected and enters the Brillouin zone from the other side again. This large deflection in reciprocal space including even dynamical Bloch oscillations translates to a strongly anharmonic real-space motion of the Bloch-electrons which gives rise to the emission of high-frequency electromagnetic radiation. The intraband dynamics, however, presuppose strongly non-resonantly driven interband carrier creation. A delicate interplay of both effects has theoretically been shown to strongly enhance HH emission [Gol08, Gol11] and is expected to cause a sensitive dependence of emitted spectra on the exact driving field shape, governed, e.g., by its carrier-envelope phase. Indeed the emitted spectra are found to exhibit a phase-dependent modulation (not shown), which is also well-reproduced by the numerical model. The appearance of even order harmonics, the asymmetric carrier injection (compare figure 3.2e) as well as the observed phase-dependence, suggests interference effects in the coherent interband polarization, which will be explained in detail by the time-resolved measurements discussed in chapter 4.

The frequency-domain study of terahertz-driven high-order harmonic generation in gallium selenide has opened the door to a novel regime of high-field transport in bulk semiconductors and highlights quantum phenomena which might become relevant for future semiconductor devices. The experimental findings sketched above not only promise novel, solid-based sources of ultrashort, extremely broadband and phase-locked laser pulses, but also set the stage for lightwave electronics at terahertz clock rates.

Chapter 4

Time-resolved solid-state high-order harmonic generation

Exploiting strong and phase-locked laser pulses to explore lightwave-driven charge transport in atoms and molecules has opened fascinating vistas and forms the backbone of attosecond science [Gou07, Kra14, Chi14]. As sketched in the previous chapter, this concept has recently been extended to solids. New extremes in ultrabroadband, phase-stable photonics [Sch14b] and photon energies already reaching the extreme ultraviolet spectral range [Ghi14, Luu15] may inspire a variety of conceivable photonic applications and spark hope for next-generation sub-femtosecond pulse sources [Ghi14, Hig14]. These experimental breakthroughs [Ghi10, Sch14b, Vam15a, Luu15] have triggered a large number of theoretical studies on solid-state HHG during the last few years [Müc11, Gol11, Ben13, Föl13, Kem13, Hig14, Vam14, She14, Vam15b, Haw15, Moi15, Wu15]. Different models and physical interpretations of the underlying generation mechanisms are proposed, complemented by ideas on how to extract fundamental information about the structure of solids or the strong-field quantum dynamics occuring during HHG. Along this line, latest studies have suggested HHG in solids as a novel, all-optical way to reconstruct the band structure of the material [Vam15a, Vam15b, Haw15]. Although most authors agree on the perception that a delicate combination of interband excitation and simultaneous intraband acceleration underlies HHG in solids, there is still an ongoing discussion on, e.g., the influence of the interband polarization, the analogy to ballistic recollision models as in the atomic case of HHG, or different frequency and intensity regimes of solid-state HHG. A precise understanding of the underlying electronic dynamics as well as potential applications thus strongly urge for a time-resolved observation of the HH emission from solids [Hig14, Ghi14], which has been out of reach so far.

In the following chapter, the very first direct time-domain study of HHG in bulk solids will be presented [Hoh15a]. The detailed temporal structure of solid-state harmonics has been revealed and precisely correlated to the driving waveform without the need for any a-priori assumptions, a measurement that had not been achieved for HHG in any system before. As corroborated by a full quantum theory based on the semiconductor Bloch equations, the observed intriguing temporal properties as well as the timing of the emission attest to a novel strong-field quantum interference between different interband excitation pathways including electronic bands below the Fermi level.

4.1 Sub-cycle cross-correlation with synchronized electro-optic sampling

Resolving the temporal structure of high-order harmonics from solids and their underlying electronic dynamics presents a formidable task and raises some experimental challenges. First, the intensity or even the electromagnetic field shape of the HH has to be detected on a time scale shorter than one half-cycle of the driving field in order to probe single emission events instead of integrating over several ones, thereby smearing out the information about what is happening during one half-cycle. Deducing the underlying charge carrier dynamics from this time-resolved observation, which is crucial in order to realize the idea of lightwave electronics sketched in the introductory chapter, raises the second and even more important task: The HH emission has to be correlated temporally with the driving field to directly link the dynamics to the momentary field amplitude which is present inside the sample. This ability will prove to be decisive for a distinction between different possible strong field-driven processes [Hoh15a, Lan16] which may lead to the emission of high-frequency electromagnetic radiation.
To this end, a novel cross-correlation scheme has been set up, which enables a time-resolved measurement of the HH emission in intensity and relative phase as well as a precise determination of the exact driving field shape on the same absolute time scale. The basic principle of the experimental scheme is depicted in figure 4.1: Strong multi-THz waveforms are focused onto a thin gallium selenide crystal in order to generate octave-spanning HH pulse trains. A metallic beamsplitter is used to collinearly superimpose these with an ultrashort gating pulse (duration of 8 fs, see chapter 2.2.1). Temporal overlap between the two pulses may be adjusted by a mechanical delay stage in the beam path of the gating pulses (not shown in figure 4.1). Both pulses are focused down tightly into a thin nonlinear crystal. Frequency mixing signals from this crystal encode both electro-optic traces of the driving waveform and the high-order harmonic time structure. For the latter, the sum frequency (SF) signal of HH and gating pulses is

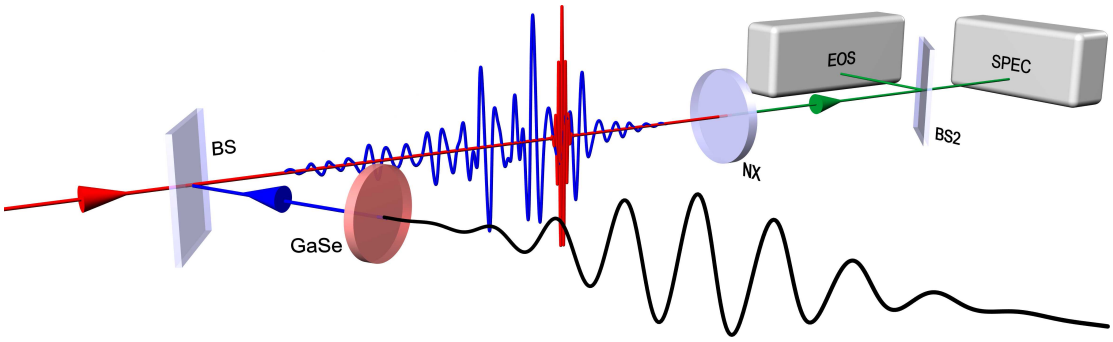

Figure 4.1: Cross-correlation scheme with synchronized electro-optic sampling: A strong multi-THz waveform (black) is focused onto a thin gallium selenide crystal (GaSe) to generate a high-order harmonic pulse train (blue). A beamsplitter (BS) is used to collinearly superimpose an ultrashort gating pulse (red), whose temporal delay with respect to the HH pulse can be varied via a mechanical delay stage (not shown). The sum frequency of gating and HH pulses is generated in a thin nonlinear crystal (NX) and spectrally resolved using a spectrograph and a silicon CCD (SPEC). A second beamsplitter (BS2) is used for parallel electro-optic-sampling (EOS) within the same nonlinear material.

recorded with a grating spectrograph and a cooled silicon CCD camera. The driving field amplitude is extracted by placing a second beamsplitter in front of the spectrograph, which guides a fraction of the emitted gating pulse into a balanced eletro-optic sampling setup. By varying the delay time between HH and gating pulses, the driving waveform may be traced in amplitude and phase in perfect synchronization with a recording of the full spectrally-resolved cross-correlation signal encoding the HH time structure.

4.1.1 Cross-correlation frequency-resolved optical gating of ultrabroadband harmonics

In order to unravel the time structure of HH, a very thin gallium selenide crystal of a thickness of only 60 µm is chosen for HHG to avoid phase matching or other propagation effects inside the sample, which might smear out the initial temporal structure. Whereas phase matching plays a crucial role during HHG for a sample thickness of 220 µm [Sch14b], the thickness used here is found to be sufficiently thin (see section 5.2). Figure 4.2a shows a typical spectrum emitted from the thin GaSe window for a driving field featuring peak amplitudes of 48 MV/cm and a centre frequency of 33 THz (see inset). To cover the enormous bandwidth of the HH pulses, several detectors have been employed: A grating monochromator in combination with a pyro-electric detector and a lead sulphide diode covers the first orders, while a compact spectrometer with a cooled indium gallium arsenide diode array is employed for intermediate orders. The vis-

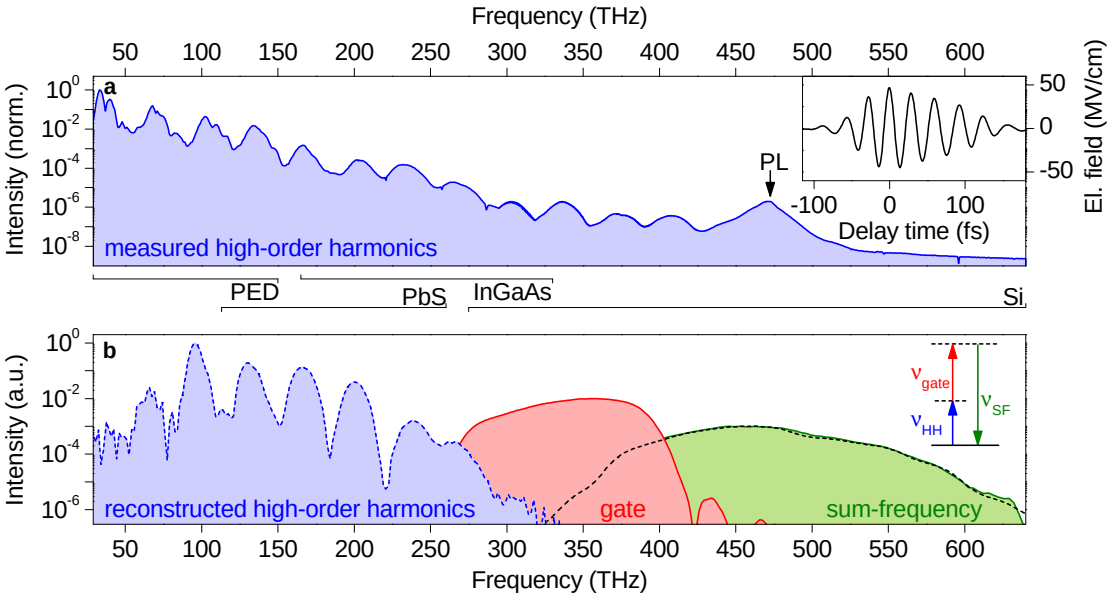

Figure 4.2: High-order harmonic cross-correlation spectra: a, The blue shaded area shows the normalized intensity spectrum of a typical HH pulse train generated by a multi-terahertz waveform featuring a centre frequency of 33 THz and peak electric field amplitudes of 48 MV/cm (field trace: see inset). The ultrabroadband spectrum has been measured using a monochromator with a pyro-electric detector (PED) or a lead sulphide photo diode (PbS) as well as spectrometers with an indium gallium arsenide (InGaAs) and a silicon (Si) detector array, respectively. The spectral efficiencies of the employed gratings and detectors have been accounted for. The peak at 476 THz stems from interband photoluminescence (PL) at the fundamental band gap of gallium selenide. **b,** The measured sum-frequency intensity (frequency-mixing process schematically depicted in the inset) for maximum efficient time overlap (green) of the HH pulse and an ultrashort gating pulse features a smooth and broad spectral shape, partially hidden underneath the gating spectrum (red, reconstructed). The reconstructed HH spectrum (dashed blue curve) includes frequencies up to 300 THz, while the retrieved sum-frequency spectrum (dashed black curve) closely follows the measured one, proving a high quality of the XFROG reconstruction. The spectra have been normalized individually and subsequently shifted in intensity for illustration purposes, i.e., the relative intensities are not comparable here.

ible regime is captured by a grating spectrograph equipped with a cooled silicon CCD camera. The quantum efficiencies of the detectors as well as the spectral response of the gratings have been accounted for. The individually recorded parts of the spectrum shown in figure 4.2a have been shifted in intensity to match the spectral intensity at the overlapping regions of the different detector ranges. The whole spectrum shows a distinct modulation, which is typical for time-integrated recordings (see below). The HH intensity decreases with increasing order with an approximately constant slope in

the logarithmic representation before the decrease seems to flatten around the photoluminescence peak marking the fundamental band gap energy of gallium selenide of approximately 2 eV.
For a broad detection range of the cross-correlation experiment, phase matching of the sum-frequency process between the gating pulse centred at a wavelength of approximately 830 nm (≈ 360 THz, see red curve in figure 4.2b) and a preferably wide spectral region within the octave-spanning high-order harmonic spectrum should be achieved. One of the most commonly used nonlinear materials for frequency mixing processes is β-barium borate (β-BaB_2O_4, short: BBO), owing to its convenient transmission range and flat spectral dispersion [Eim87]. Here, a 10-µm-thin BBO crystal is employed under type-I phase matching conditions to ensure maximally broadband phase matching (see appendix B).
A short-pass filter, which blocks all spectral components with wavelengths longer than 725 nm (i.e., frequencies below 410 THz), and a Glan-Thompson polarizer have been placed in front of the spectrometer to attenuate the gating pulses. This way, the sum frequency signal, which is much weaker than the intensity of the gating pulse, may be detected while exploiting the full dynamic range of the spectrometer. If the temporal delay between the gating pulse and the HH pulse train is optimized for most efficient sum-frequency generation, a broadband and spectrally smooth SF signal is recorded, as shown in figure 4.2b (green curve). Remarkably, this SF spectrum lacks the typical spectral modulation of time-integrated recordings, a finding that proves the sub-cycle resolution achieved with the new cross-correlation setup: If the gating pulse overlapped temporally with two or more high-order harmonic bursts emitted during different half-cycles of the driving waveform, this repeated time structure would be imprinted on the nonlinear mixing signals. As following from the principles of Fourier transformation, the observed spectrum would thus exhibit a spectral modulation with a periodicity of the inverse temporal spacing (see also section 5.4).

Broadband XFROG reconstruction

Recording such sum-frequency spectra for different delay times τ between the HH pulse train and the gating pulse yields a full 2D-spectrogram as shown in figure 4.3a. The false-colour plot represents the SF intensity $I_{\mathrm{SF}}(\tau, \nu_{\mathrm{SF}})$ as a function of τ and the sum-frequency ν_{SF}. The delay time is defined such that negative values $\tau \ll 0$ mean that the gating pulse arrives before the HH pulse, while $\tau = 0$ has been set as the delay time where the spectrally integrated SF intensity (figure 4.3c) peaks. Already here, some basic features in the time structure of the emitted HH train become obvious: Starting with relatively weak and narrowband signals at around $\tau = -65$ fs, periodically repeating

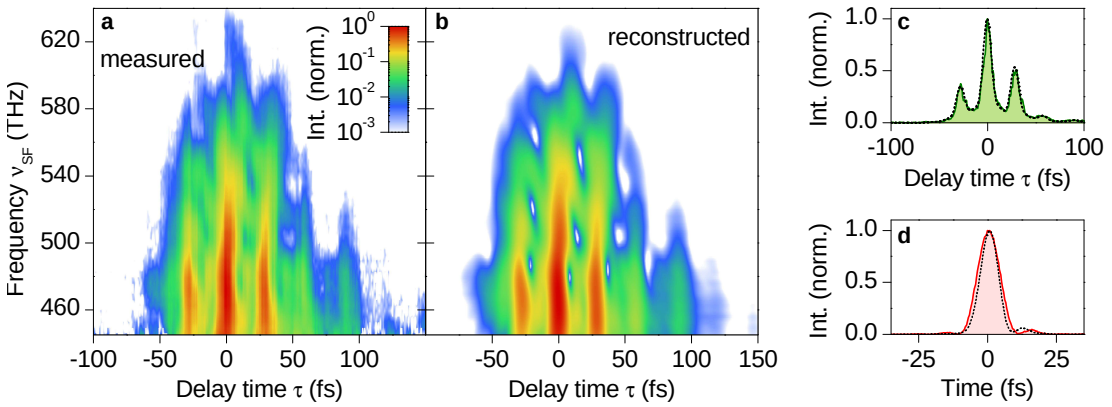

Figure 4.3: Broadband XFROG reconstruction: a,b, Colour-coded plot of the measured (a) and reconstructed (b) sum-frequency intensity as a function of frequency and the delay time between the HH pulse train and the gating pulse. **c,** Temporal shape of the spectrally integrated sum-frequency intensity as measured (green shaded) and reconstructed (black dashed). **d,** Intensity envelope of the gating pulse as retrieved from the XFROG algorithm (black dashed) as well as from an independent second-harmonic FROG measurement and reconstruction based on a different algorithm (red shaded).

bursts with increasing ($\tau \leq 0$) and finally decaying ($\tau \geq 0$) intensity and bandwidth occur. Interestingly, most of the spectral components within the detection bandwidth seem to be emitted at the same instant of time, as indicated by the nearly unchirped SF bursts (e.g., around $\tau = 0$).

The SF signal discussed so far is still a convolution of the gating and the HH pulse, however, and extracting the actual temporal shape of the emitted high-harmonics requires a thorough separation of both signals. As shown by Kane et al., this separation is indeed feasible via an iterative numerical algorithm [Kan93]. Based on this reconstruction scheme, a technique called ***F**requency-**R**esolved **O**ptical **G**ating* (acronym FROG or XFROG in this case, where X stands for cross-correlation) has been developed [Kan93] and settled as a well-established method to resolve the temporal structure of ultrashort light pulses in intensity and relative phase. While the data processing steps and the basic principles of the customized algorithm employed here [Wya] are sketched in appendix C, the discussion here purely focuses on the general capabilities of the scheme as well as its results.

The goal of the algorithm is to reconstruct the shape of the unknown pulse [Kan98], which is the HH pulse in this case:

$$E_{\mathrm{HH}}(t) = \mathrm{Re}\left\{\sqrt{I_{\mathrm{HH}}(t)}\exp\left[i\omega_0 t + i\varphi_{\mathrm{HH}}(t)\right]\right\} \tag{4.1}$$

$I_{\mathrm{HH}}(t)$ and $\varphi_{\mathrm{HH}}(t)$ are the time-dependent HH intensity and phase, respectively, and ω_0

is the carrier frequency. The generated frequency mixing signal for a given delay time τ is then represented by the product of the HH field with the delayed field of the gating pulse, $E_{\mathrm{HH}}(t)E_{\mathrm{gate}}(t-\tau)$. The recorded 2D sum-frequency spectrogram may consequently be written as the magnitude squared of the Fourier transform of this nonlinear signal:

$$I_{\mathrm{SF}}(\omega,\tau) = \left| \int_{-\infty}^{\infty} E_{\mathrm{HH}}(t) E_{\mathrm{gate}}(t-\tau) \exp(-i\omega t) dt \right|^2 \tag{4.2}$$

Starting with a guess for $E_{\mathrm{HH}}(t)$, the algorithm calculates $I_{\mathrm{SF}}(\omega,\tau)$ by performing a Fourier transformation and compares the reconstructed spectrogram with the measured one. The deviation between both is minimized in an iterative way (see appendix C), finally yielding both the intensity $I_{\mathrm{HH}}(t)$ and the relative phase $\varphi_{\mathrm{HH}}(t)$ of the emitted high-order harmonic pulse train.
As a measure for the quality of the reconstruction scheme, one may thus compare the original measured spectrogram with the retrieved one. As can be seen by comparison of figures 4.3a and b, the reconstructed spectrogram resembles the measured one to a very high degree of congruency. The good match between the datasets is further corroborated by the similarity of the two spectrally integrated SF traces shown in figure 4.3c. In addition, the retrieved intensity envelope of the gating pulse (figure 4.3d) closely follows the one reconstructed from an independent second harmonic FROG measurement. The squared magnitude of the Fourier transform of the extracted HH field profile (equation (4.1)) yields the time-integrated HH intensity spectrum within the detection bandwidth of the experimental setting. As can be seen in figure 4.2b, the typical spectral modulation of the HH frequency comb can be well reproduced, with harmonics up to the ninth order being clearly discernible. The relative attenuation of the second order can be attributed to the mentioned transparency range of the employed BBO crystal, while the high-frequency limit is set by the drastic decrease of HH intensity with increasing frequency, limiting the efficiency of the nonlinear mixing process (see appendix B).
The reconstruction scheme reliably converges for arbitrary runs and datasets, allowing for a faithful extraction of the temporal fine structure of solid-state high-order harmonics including even subtle features in their relative phase on a sub-cycle time scale (see sections 4.2 to 4.4).

4.1.2 Precise temporal correlation with the driving field

As explained above, tapping the full potential of the concept of lightwave-driven electronics requires a direct and precise temporal correlation of the applied electric waveform with the probed processes, i.e., high-order harmonic generation. The new cross-correlation setup (figure 4.1) is capable of detecting the sum-frequency signal between

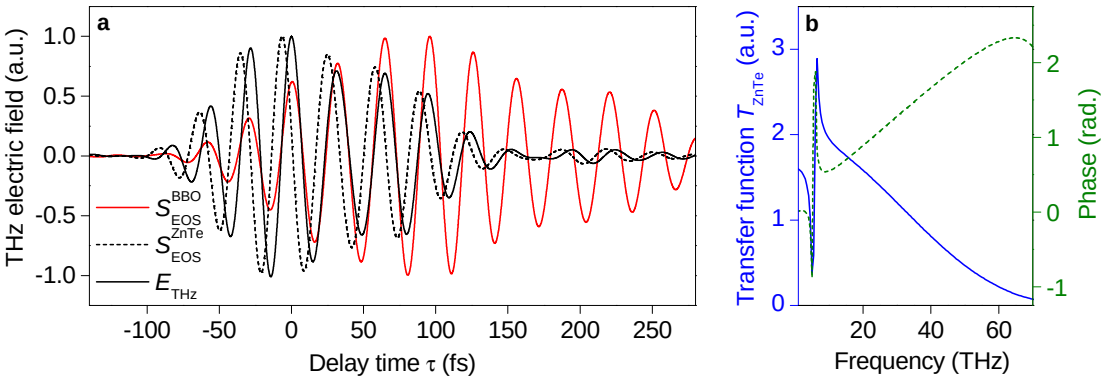

Figure 4.4: Correlation of EOS time scales: a, Electro-optic signal of the multi-terahertz driving field as recorded using a 10-µm-thin BBO detector (red) and a 6.5-µm-thick ZnTe crystal (black dashed) for spectral components within 12 - 45 THz. The black solid curve represents the corresponding terahertz electric field E_{THz} as a function of delay time after correction for the complex-valued detector response of the ZnTe crystal displayed in panel b. **b,** Absolute value (blue) and phase (green dashed) of the transfer function T_{ZnTe} in the multi-terahertz frequency range for a crystal thickness of 6.5 µm.

the HH and the gating pulse as well as the electric field trace of the applied multi-THz transient at the same time. For every single step of the mechanical delay stage, i.e., a given temporal delay time τ, a full spectrum of the sum-frequency, yielding the temporal HH envelope after XFROG reconstruction, and the instantaneous field amplitude of the driving waveform are recorded. Both signals are mediated by the same 10-µm-thin BBO crystal. This passive synchronization, however, is not yet sufficient for a precise correlation of the emitted HH with the applied field inside the generation crystal. In fact, there are several aspects influencing the relative timing between the two signals as well as the shape and the phase of the detected transient. First, the detector response of BBO significantly influences the detected electro-optic field trace. Second, the detected waveform reflects the field inside the detector crystal, not the one applied to the GaSe sample where HHG takes place. Finally, propagation inside the crystals and in between as well as focusing effects will have to be taken into account. The following paragraphs will provide a comprehensive step by step treatment of all effects influencing the timing between the measured signals.

Detector response of the electro-optic sampling crystal

The measured electro-optic trace of the multi-THz waveform $S_{\mathrm{EOS}}(\tau)$ (see figure 4.4a) in principle depends on the bandwidth of the gating pulse, the linear dispersion of the employed detector material as well as the dispersion of its nonlinear $\chi^{(2)}$-coefficient. Extracting the actual profile of the applied electric field $E_{\mathrm{THz}}(\tau)$ is possible via numerically

correcting for these effects: Following a well-established formalism [Gal99], the complex transfer function $T(\nu)$ of the material may be calculated, which connects the measured and the actual waveform in the frequency domain via

$$\tilde{E}_{\mathrm{THz}}(\nu) = \tilde{S}_{\mathrm{EOS}}(\nu) \cdot T(\nu)^{-1}, \tag{4.3}$$

where symbols with a tilde denote the Fourier transform of the corresponding temporal quantities.

While BBO has been chosen here as a nonlinear material due to its enormous phase matching bandwidth in the near-infrared range (compare appendix B), its transmission drastically decreases for wavelengths longer than approximately 3.5 µm, accompanied by a steep increase in the refractive index [Eim87]. The electro-optic traces detected in BBO are consequently expected to differ from the incoming waveforms, which feature central wavelengths around 9 µm. Moreover, the dispersion of BBO is not well known within the absorbing mid-infrared range, rendering a determination of the transfer function $T_{\mathrm{BBO}}(\nu)$ challenging. Circumventing these difficulties requires an additional reference measurement. For a faithful determination of the actual terahertz waveform, the BBO crystal is replaced by a ⟨110⟩-oriented zinc telluride crystal (ZnTe) of a thickness of 6.5 µm, whose transfer function in the relevant spectral range is established [Gal99]. Figure 4.4 shows an example of this procedure: The electro-optic trace recorded in BBO ($S_{\mathrm{EOS}}^{\mathrm{BBO}}(\tau)$, red waveform) is strongly delayed with respect to the one measured in ZnTe ($S_{\mathrm{EOS}}^{\mathrm{ZnTe}}(\tau)$, black dashed curve). Applying the complex detector response function $T_{\mathrm{ZnTe}}(\tau)$ shown in panel b yields the actual terahertz field transient at the detection focus $E_{\mathrm{THz}}(\tau)$ (black waveform). Provided that the two crystals are placed at exactly the same longitudinal position in the focus (z-coordinate, see next paragraph), the relative delay between the traces measured in BBO and ZnTe, respectively, may be extracted statistically after repeating this sequence several times. This way, the electro-optic trace recorded in parallel with the cross-correlation signal may be used as a precise temporal reference marker. The accuracy of this procedure is estimated to be 1.2 fs by calculating the standard deviation of the relative temporal delay between the detected traces $S_{\mathrm{EOS}}^{\mathrm{BBO}}$ and $S_{\mathrm{EOS}}^{\mathrm{ZnTe}}$ for 17 subsequent recordings. The crystal thickness of the ZnTe detector, which is glued on a 300-µm-thin, electro-optically inactive ⟨100⟩-oriented ZnTe substrate, has been determined by Fabry-Perot interferometry. The absolute error in this measurement translates to a standard deviation of the relative temporal delay between the measured waveforms of 0.9 fs. Alltogether, the accuracy of the temporal correlation thus amounts to $\sigma = 1.5$ fs, which is 20 times shorter than one oscillation period of the terahertz driving waveform.

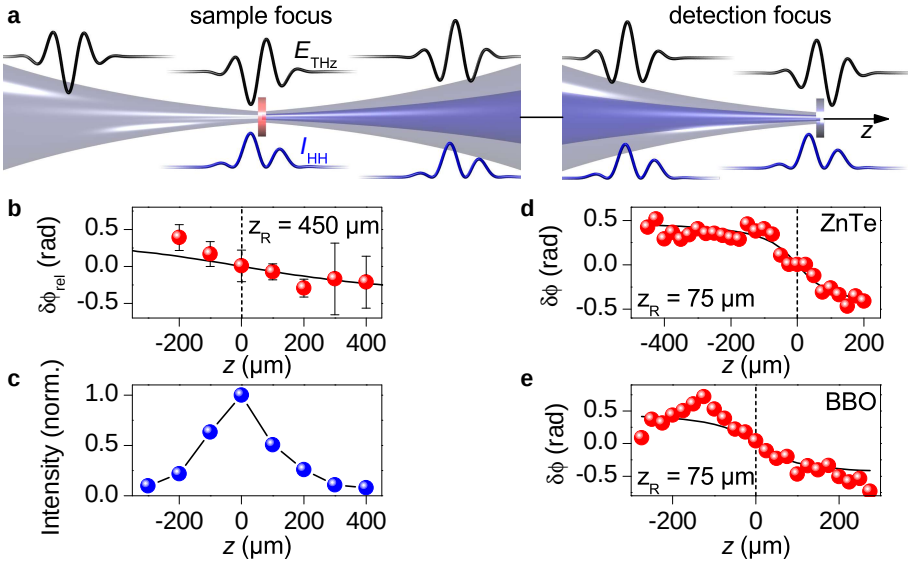

Figure 4.5: Gouy phase shift of the driving waveform between sample and detection focus: a, Schematic illustration of the phase change imprinted on the driving waveform during propagation through the cross-correlation setup. While the multi-THz transient (black waveform) experiences a Gouy phase shift in both foci, the shape of the recorded sum-frequency signal encoding the HH intensity (I_{HH}, blue curve) does not change. **b,** Red dots depict the temporal shift of the peaks of the recorded SF intensity relative to the peaks of electro-optic traces detected in parallel as a function of the sample position z. Vertical error bars represent the standard deviation of the extracted phase shift for the different SF peaks within one spectrogram. Due to the decreased SF intensity, a faithful extraction of the relative phase shift has not been possible for positions $z < -200\,\mu\mathrm{m}$. The black curve shows the expected phase shift for the geometrical focusing conditions (Rayleigh length $z_R = 450\,\mu\mathrm{m}$). **c,** Overall intensity of the recorded SF signal as a function of the z-position of the sample (data points shown as blue dots). **d,e,** Phase change of the recorded waveforms as extracted from their zero-crossings (red dots) for different positions z of a 10-µm-thin BBO crystal (d) and a 6.5-µm-thin ZnTe crystal (e). The theoretical Gouy phase shift for a Rayleigh length of 75 µm, as estimated from the geometrical focusing conditions, is shown as a black curve.

Propagation effects and Gouy phase shift

With the correlation technique described above, the measured sum-frequency signal and thus the temporal shape of the emitted high-order harmonics may be exactly correlated with the terahertz waveform at the detector crystal placed in the detection focus. The field shape of interest, in contrast, is the one which is applied to the gallium selenide sample. Within the GaSe crystal, group velocity dispersion, i.e., a different propagation speed of the fundamental multi-THz waveform and the generated HH pulse train, may lead to a measurable delay between both, which would alter the measured emission

timing. Phase matching has indeed been found to influence HHG in samples with a thickness on the order of 200 µm. In the thin sample used here (thickness of only 60 µm), however, phase matching does not play a significant role (see discussion of figure 5.2) and is deliberately avoided by choosing normal incidence. In addition, the emitted harmonics do not feature a significant chirp (figure 4.3), which would indicate reasonable group velocity delay in the sample. These facts may lead to the conclusion that HHG is confined to a thin region near the back facet of the GaSe window, with a coherence length of, e.g., 6 µm for the 9th harmonic order. Using only reflective optics excludes any further group velocity delay collected between the generation and the detection focus.
When dealing with phase-sensitive techniques like electro-optic sampling, however, an often ignored property of focussed Gaussian beams becomes essential. During propagation through a focus, the so-called Gouy phase gets imprinted on the carrier wave of a light pulse [Boy03]:

$$\delta\phi_{\mathrm{Gouy}}(z) = \arctan(z/z_{\mathrm{R}}) \tag{4.4}$$

As defined in figure 4.5a, z denotes the axial distance from the beam waist. The so-called Rayleigh length $z_{\mathrm{R}} = \pi\omega_0^2/\lambda$ is defined as the axial distance where the on-axis peak intensity of a Gaussian beam of wavelength λ and beam waist ω_0 is one half of the maximum value at the focus plane $I(z_{\mathrm{R}}) = I(z = 0)/2$.
In the experiment, this Gouy phase modulation leads to an overall phase shift of $\delta\phi_{\mathrm{Gouy}} = \pi$ [You97, Ruf99] of the multi-THz waveform between HHG in the gallium selenide sample and its detection in the ZnTe detector, if both the detector and the generation crystal are placed exactly at their respective focal planes (compare schematic illustration in figure 4.5a). For the sample focus, a Rayleigh length $z_{\mathrm{R}} = 450\,\mu\mathrm{m}$ is estimated from the geometrical focusing conditions. To ensure correct positioning of the thin GaSe window, a series of both cross-correlation spectrograms and electro-optic traces of the transmitted waveforms has been recorded for different z-positions of the sample (so called z-scan). While the measured multi-THz transients do not depend on the sample position, the peaks of the sum-frequency time traces are temporally shifted with respect to the transient following the evolving Gouy phase for different values of z. Figure 4.5b shows the relative phase change between the peaks of the sum-frequency signal and the field crests of the detected waveform (red dots) in comparison with the theoretically expected phase shift (black curve). In line with the recorded phase change, the overall intensity of the generated sum-frequency peaks at $z = 0$, as displayed in figure 4.5c. The remaining uncertainty in the sample position can be neglected due to the large Rayleigh length compared to the sample thickness.
Analogous z-scans have been recorded for the detector position. Here, electro-optic traces of the multi-THz transients have been measured for different focus positions of the

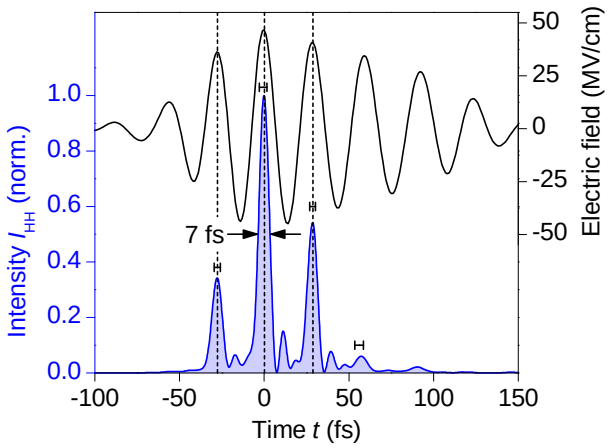

Figure 4.6: Time-resolved HH emission and precise correlation with the driving field: The blue shaded area displays the temporal shape of the emitted HH intensity $I_{\mathrm{HH}}(t)$ on the same absolute time scale as the driving field (black waveform). The vertical dashed lines highlight the terahertz peak amplitudes. Horizontal error bars mark the standard deviation in the timing of the HH peak intensity for 12 consecutive scans.

10-µm-thin BBO crystal and the 6.5-µm-thin ZnTe crystal, respectively. The observed phase shift, as extracted from the zero crossings of the electromagnetic waveforms (red dots in figure 4.5d, e), matches the calculated Gouy phase change for a geometrically determined Rayleigh length of 75 µm. This way, the crystals may be placed at exactly the same z-position with respect to the focal plane, which is crucial for a temporal correlation of the electro-optic traces (see above) as well as the determination of the collected Gouy phase shift between the two foci.

4.2 Temporal fine structure of solid-state high-order harmonics

Putting together the experimental achievements sketched in the preceding sections, the novel cross-correlation scheme with synchronized electro-optic sampling enables the very first time-resolved observation of high-order harmonics from a bulk solid. Furthermore, a direct, precise and purely experimental temporal correlation with the driving field becomes possible, which has not been achieved for HHG in any system, so far.
Figure 4.6 shows the high-order harmonic intensity envelope $I_{\mathrm{HH}}(t)$ (blue) together with the multi-THz driving field (black) on the same absolute time scale. The displayed intensity trace, which has been reconstructed from the spectrogram shown in figure 4.3a, reveals a rich time structure and some remarkable properties:

(i) The emitted harmonics form a pulse train of three dominant, ultrashort bursts featuring an intensity full-width at half-maximum of only 7 fs. This pulse length corresponds to the duration of approximately only one oscillation cycle of the fourth harmonic order. Such ultrashort bursts are only possible if all the frequency components within the detection bandwidth are emitted almost simultaneously, which is consistent with the observed unchirped sum-frequency signal (compare figure 4.3).

In contrast to atomic HHG, which leads to the so-called *atto-chirp* [Chi14], the HH observed here can thus not exhibit significant chirp, as also corroborated in figure 4.7 below.

(ii) Efficient HH emission in gallium selenide only occurs during every second half-cycle of the strong driving field. While positive field crests[1] of the driving waveform produce pronounced and comparably intense HH bursts, the emission is strongly suppressed for the negative field extrema. This unipolar emission contrasts with atomic HHG, where every half-cycle of the driving waveform contributes to the emission. Recent theoretical studies [Ghi12, Hig14] have consistently predicted HH emission from bulk solids in a bipolar way, too.

(iii) Surprisingly, the correlation with the terahertz waveform unravels a precise synchronization of the HH emission bursts with the driving field crests of positive polarity: $I_{\mathrm{HH}}(t)$ peaks within ± 2 fs around the terahertz field peaks which are highlighted by the dashed vertical lines in figure 4.6. Recollision models [Cor93, Lew94], as they apply for HHG in atoms [Chi14, Kra14] or electron-hole collisions in solids [Zak12, Lan16], predict a distinct delay between the driving field crests and the maximum HH emission, which reflects the ballistic acceleration of charge carriers before the emission occurs.

Instantaneous frequency of solid-state high-harmonics

The XFROG reconstruction scheme introduced in section 4.1.1 reveals even more detailed information on the sub-cycle time structure of emitted high-harmonics. Besides the intensity $I_{\mathrm{HH}}(t)$, the relative phase $\varphi_{\mathrm{HH}}(t)$ as defined in equation (4.1) may also be determined. As expected from the unchirped sum-frequency signal and the ultrashort HH bursts, the relative phase of typical HH emission traces as shown in figure 4.7a (blue: $I_{\mathrm{HH}}(t)$, black: $\varphi_{\mathrm{HH}}(t)$) exhibits a very subtle, but reproducible modulation. This slight phase evolution translates into a variation of the instantaneous emitted frequency ν_{i}, which may be derived by numerical differentiation of the phase term in equation (4.1):

$$\nu_{\mathrm{i}}(t) = (2\pi)^{-1} \frac{\mathrm{d}}{\mathrm{d}t} \Phi(t) = (2\pi)^{-1} \frac{\mathrm{d}}{\mathrm{d}t} \left(\omega_0 t + \varphi_{\mathrm{HH}}(t)\right) \tag{4.5}$$

The quantity ν_{i} defines the weighted instantaneous frequency of the emitted high-order harmonics within the detection bandwidth of the cross-correlation experiment (compare figure 4.2b). As can be seen in figure 4.7a, the instantaneous frequency (red curves) repeatedly evolves in a well-defined and reproducible fashion during the individual HH

[1] Note that the sign of the terahertz driving field is not experimentally determined, e.g., with respect to the crystallographic direction and may be arbitrarily chosen without loss of generality.

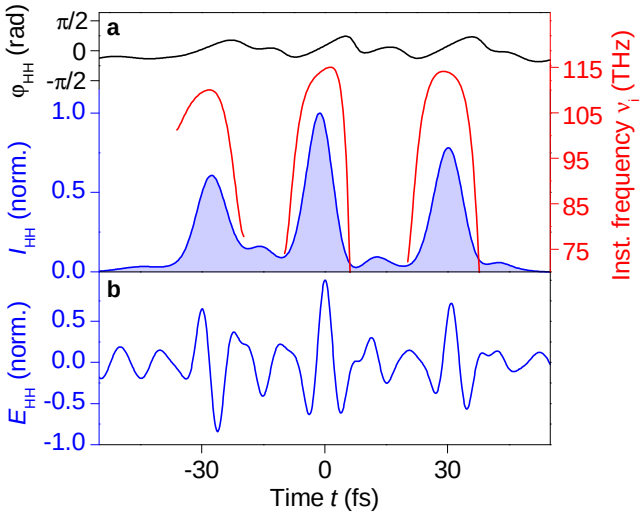

Figure 4.7: Relative phase and instantaneous frequency of high-order harmonics: a, Temporal intensity I_{HH} (blue), relative phase φ_{HH} (black) and instantaneous frequency ν_{i} (red) of a typical HH pulse train for a peak driving field of 33 MV/cm. The instantaneous frequency is not well-defined for very low intensities, which is why ν_{i} is only shown around the three dominant peaks. **b,** Corresponding HH field E_{HH} with a carrier-envelope phase artificially set to zero.

emission bursts: It is ramped up when the HH intensity increases (i.e., while the driving field amplitude grows), reaches its maximum at about the emission peak and finally decays again with decreasing driving field and HH intensity. This qualitative behaviour strongly resembles the Bloch frequency ν_{B}, which is directly proportional to the externally applied electric field (compare equation (3.5)). The observed subtle frequency modulation may thus be a direct fingerprint of the charge carrier acceleration within the electronic bands following Bloch's seminal theorem [Blo29, Zen34] (see also section 4.4). Finally, the extracted information about the temporal intensity and relative phase may prospectively even enable a reconstruction of the full electromagnetic field profile $E_{\mathrm{HH}}(t)$ of the high-order harmonics. The XFROG algorithm does not yet deliver the absolute temporal phase, however, but $\varphi_{\mathrm{HH}}(t)$ is only defined up to a constant additive phase φ_0, which defines the carrier envelope phase of the emitted HH burst. As an example, figure 4.7b displays the extracted field profile where φ_0 has been set to zero. Since the emitted HH are inherently phase-stable and the lowest orders have already been detected electro-optically [Sch14b, Sch14a], the carrier-envelope phase may also be determined in the future by comparing the reconstructed field shape at spectral overlap with electro-optically detected waveforms. The ability to trace octave-spanning high-order harmonics in amplitude and phase would open new perspectives for extremely broadband, field-resolved spectroscopy.

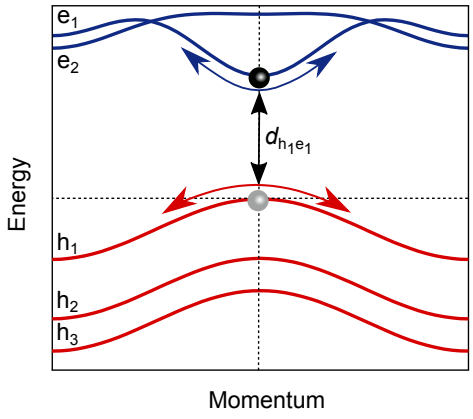

Figure 4.8: Reciprocal space schematic of the five-band model: The numerical quantum model includes five electronic bands, three valence bands h_1, h_2 and h_3, as well as two conduction bands e_1 and e_2. Bandstructure parameters from gallium selenide are taken from reference [Sch76]. The model treats interband excitation (black arrow and dipole matrix element $d_{h_1e_1}$ shown as an example) and simultaneous intraband charge transport (red and blue arrows) on equal footing, thereby capturing their delicate interplay.

4.3 Strong-field quantum interference during high-harmonic generation in solids

The revealed temporal structure of high-order harmonics from gallium selenide as well as their emission timing with respect to the driving waveform suggests a unipolar and quasi-instantaneous generation mechanism. As shown in the following, these findings strongly indicate a novel quantum interference between different interband polarization pathways, which will by explained by a quantum-mechanical many-body theory based on the semiconductor Bloch equations [Gol08, Gol11]. If not mentioned otherwise, all theoretical data shown in this chapter presents the results of these numerical simulations, which have been performed by Ulrich Huttner [Hoh15a].

4.3.1 Quantum many-body model of HHG in semiconductors

The electronic dynamics in a semiconductor under the influence of a strong terahertz field $E_{\mathrm{THz}}(t)$ may be simulated by solving the general semiconductor Hamiltonian [Hau09]

$$\hat{\mathrm{H}} = \hat{\mathrm{H}}_0 + \hat{\mathrm{H}}_{\mathrm{inter}} + \hat{\mathrm{H}}_{\mathrm{intra}} + \hat{\mathrm{V}}, \tag{4.6}$$

which contains the band structure of the semiconductor ($\hat{\mathrm{H}}_0$) and includes both interband excitation between different electronic bands ($\hat{\mathrm{H}}_{\mathrm{inter}}$) as well as carrier acceleration within single bands ($\hat{\mathrm{H}}_{\mathrm{intra}}$). The Coulomb potential $\hat{\mathrm{V}}$ describes the mutual electromagnetic interaction of the electrons and is usually modelled via electronic dephasing. The interband term

$$\hat{\mathrm{H}}_{\mathrm{inter}} = -E_{\mathrm{THz}}(t) \sum_{\lambda,\lambda',k} d_{\lambda,\lambda'}(k) \hat{a}^{\dagger}_{\lambda,k} \hat{a}_{\lambda',k} \tag{4.7}$$

describes the transition of an electron from one band λ' to another band λ via the annihilation and creation operators $\hat{a}$ and $\hat{a}^\dagger$, respectively, while the dipole matrix element $d_{\lambda,\lambda'}(k)$ defines the strength of this transition (see figure 4.8). The intraband acceleration of electrons within a single band λ is included via the term

$$\hat{\mathrm{H}}_{\mathrm{intra}} = i|e|E_{\mathrm{THz}}(t)\sum_{\lambda,k}\hat{a}^\dagger_{\lambda,k}\nabla_k\hat{a}_{\lambda,k}. \tag{4.8}$$

The Heisenberg equation of motion allows for evaluating the operator dynamics, which leads to the so-called semiconductor Bloch equations [Hau09]. This set of coupled differential equations is solved numerically and describes the time-dependent electron and hole occupations $f_k^\lambda = \langle\hat{a}^\dagger_{\lambda,k}\hat{a}_{\lambda,k}\rangle$ and the microscopic polarizations $p_k^{\lambda,\lambda'} = \langle\hat{a}^\dagger_{\lambda,k}\hat{a}_{\lambda',k}\rangle$ for $\lambda \neq \lambda'$.

To customize the model described in [Gol08, Gol11], the uppermost three valance bands and the lowermost two conduction bands of gallium selenide are implemented following a one-dimensional tight binding approach [Gol11] with parameters from reference [Sch76]. A driving field profile $E_{\mathrm{THz}}(t)$ closely matching the experimental one is used to calculate the electronic dynamics without falling back on the rotating wave approximation [Hau09]. The emitted high-order harmonic field is finally evaluated via the equation

$$E_{\mathrm{HH}}(t) = \frac{\partial}{\partial t}P(t) + J(t), \tag{4.9}$$

which accounts for both the polarization source $P(t) = \sum_{\lambda,\lambda',k} d_{\lambda,\lambda'}(k)p_k^{\lambda,\lambda'}$ and the current source $J(t) = \sum_{\lambda,k} j_\lambda(k)f_k^\lambda$. The current matrix element $j_\lambda(k) = |e|\hbar^{-1}\nabla_k\varepsilon_k^\lambda$ is governed by the dispersion of the electronic band ε_k^λ (for simplicity, the k-dependence of the bands is denoted by an index k from now on).

This approach has been proven to explain the enormously broadband spectral HH emission, thereby reproducing even details in the emitted spectra (see figure 3.2d, e and reference [Sch14b]). The theory captures a series of important features of the underlying dynamics which are crucial for a complete picture of HHG in bulk solids. First, terahertz-induced band mixing as well as the influence of changing occupations during the generation mechanism is dynamically accounted for, which means that a modulation of the band structure owing to the enormous potentials induced by the strong terahertz fields is included in the simulations. Second, interband excitation and simultaneous intraband acceleration are treated on equal footing (see figure 4.8), which renders ad-hoc assumptions about the carrier creation unnecessary. Finally, several electronic bands (up to five in the current simulations) may be accounted for, which is crucial for explaining the observed temporal characteristics of HH emission from gallium selenide, as explained below.

4.3.2 Quantum interference of different interband polarization pathways

The observed temporal characteristics of the emitted high-order harmonics from gallium selenide imply some important, so far unknown constraints on the underlying dynamics (compare section 4.2). (i) The nearly unchirped phase of ultrashort HH bursts attests to a microscopic generation process, where most of the frequency components within the broadband spectrum are emitted simultaneously. (ii) The unipolar nature of the emitted pulse train with respect to the sign of the driving field suggests a strong asymmetry within the underlying mechanism. (iii) The synchronization to the driving field maxima hints to a quasi-instantaneous emission source, which is not compatible with retarded, ballistic effects as expected from a recollision-based generation scheme. These observations rule out a number of recent theoretical attempts to explain solid-state HHG. Strong analogies to the three-step model of atomic HHG [Cor93, Lew94] have been suggested, where the excess energy of electrons and holes which collide at spatial overlap after acceleration within the bands is released as high-order harmonic radiation [Vam15a]. This kind of ballistic motion implies a distinct delay between maximum HH emission and the driving field peaks, reflecting the time needed to accelerate, reverse and recollide the electrons and holes (see chapter 3). Simple intraband models based on the Bloch-acceleration of carriers [Ghi10, Müc11, Fre12, Ghi12] within the bands have been shown to reproduce spectral features of solid-state high-harmonics but suffer from the need of ad-hoc assumptions on the carrier creation, i.e., the transition from a bound electronic state in a valence band to a continuum-like free state in the conduction band. Furthermore, many-body effects like the mutual Coulomb interaction of electrons cannot be accounted for in these straightforward models. Even more sophisticated models, which also take into account the interband excitation of carriers, fail to explain the unipolar emission, if only two electronic bands are included in the simulations [Hig14]: As following from Kramer's seminal theorem [Kra30], the reciprocal space representation of electronic bands in a solid is always inversion-symmetric with respect to the crystal momentum k if the spin-degeneracy is not lifted, e.g., by strong spin-orbit coupling or external magnetic fields. Consequently, intraband charge transport within the bands cannot solely explain the strongly asymmetric behaviour observed in the experiment.

As soon as more than two electronic bands are involved, however, electrons can be excited via different pathways of microscopic interband polarization, which may interfere within their ultrashort coherence time. As shown in the following, this quantum interference influences the total amount of carrier population in the respective bands and drastically alters the temporal shape of emitted harmonics on a sub-cycle time scale.
While all calculations have been performed with five electronic bands as shown in figure 4.8, it is more intuitive to understand the interband dynamics within a minimal

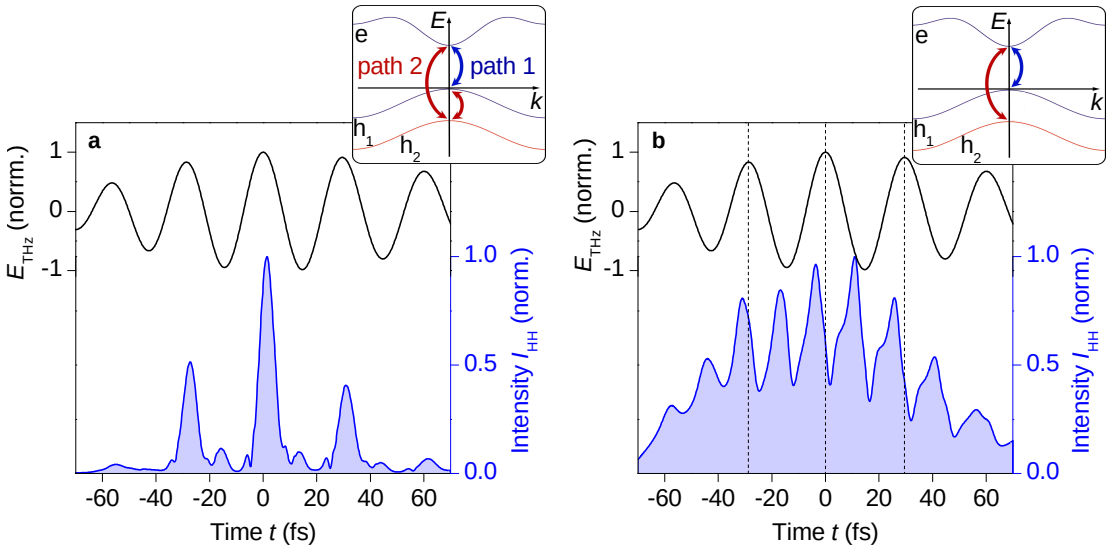

Figure 4.9: Interband quantum interference during HHG in gallium selenide: a, Result of the full numerical simulation including all possible transitions between the five bands included in the many-body calculation. The HH intensity $I_{\mathrm{HH}}(t)$ (blue shaded) is shown on the same absolute time scale as the driving field (black) used in the calculations. Closely resembling the experimental data, $I_{\mathrm{HH}}(t)$ peaks within 2 fs around the driving field maxima, while it is strongly suppressed for negative half-cycles. The inset schematically depicts a minimal three-band model (two valence bands h_1, h_2 and one conduction band e), supporting quantum interference between a *direct* polarization path ("1") and an *indirect* one ("2"), both connecting valence band h_1 with the conduction band e. **b,** When the *indirect* paths are suppressed by setting all relevant dipole matrix elements to zero (inter-valence band transition $\mathrm{h}_1 \rightarrow \mathrm{h}_2$ closed in the minimal model, see inset), the calculation neither reproduces the unipolar fashion of $I_{\mathrm{HH}}(t)$ (blue) nor the synchronization to the crests of the driving field (black, maxima highlighted by the vertical black dahsed lines).

model of two valance bands "h_1", "h_2" and one conduction band "e" as depicted in the inset of figure 4.9a: Initially, electronic transitions may only occur via the *direct* paths from the respective valence bands to the conduction band ($\mathrm{h}_1 \rightarrow \mathrm{e}$ and $\mathrm{h}_2 \rightarrow \mathrm{e}$), since transitions between the valence bands are Pauli-blocked for the field-free case. The strong, non-resonant terahertz field may significantly empty h_2, however, clearing the inter-valence band transition $\mathrm{h}_1 \rightarrow \mathrm{h}_2$. This new situation now supports two different pathways from the uppermost valence band h_1 to the conduction band e, the one of which ("path 1") represents a *direct* transition, whereas the other one ("path 2") couples two direct transitions and will be referred to as the *indirect* path $\mathrm{h}_1 \rightarrow \mathrm{h}_2 \rightarrow \mathrm{e}$. As derived in more detail below, the transition amplitudes of *direct* and *indirect* paths feature different symmetries with respect to the driving field signs. Since the total amount

of carriers promoted to the conduction band is defined by the coherent superposition of both transition amplitudes, the HHG efficiency also depends on the sign of the terahertz field, which might explain the unipolar emission.
To test the validity of this concept, a systematic switch-off analysis is performed, which compares the temporal features of HH emission with and without the possibility of interference between *direct* and *indirect* polarization paths, respectively. Taking into account all possible transitions, the calculations portray the experimentally recorded HH intensity envelope to a very high degree of congruency, which can be seen in figure 4.9a. The global emission shape featuring three ultrashort, dominant bursts is properly reproduced. Even the rich temporal sub-cycle structure matches the experimental observation very well. In particular, $I_{\mathrm{HH}}(t)$ is strongly suppressed for negative half-cycles of the driving waveform (black curve in figure 4.9a) and peaks within $\pm 2\,\mathrm{fs}$ around the field crests. In a second step, all *indirect* paths between the five electronics bands are artificially disabled by setting the corresponding dipole matrix elements to zero. Within the minimal three-band model, this implies a vanishing inter-valence band matrix element $d_{\mathrm{h}_1,\mathrm{h}_2} = 0$ and only allows the two *direct* paths connecting the respective valence bands with the conduction band (see inset to figure 4.9b). The numerical result of this scenario is presented in figure 4.9b: Neither the unipolar emission nor the synchronization of the peaks of $I_{\mathrm{HH}}(t)$ (blue shaded) with the driving field maxima (highlighted by vertical, black dashed lines) can be reproduced. In contrast, the shape of $I_{\mathrm{HH}}(t)$ now resembles atomic HH traces, where the emission occurs during every half-cycle of the driving field and peaks at a distinct time delay after the field crests.

Coherent control level

For a more comprehensive theoretical analysis on the influence of the quantum interference on the temporal emission characteristics, one may gradually decrease the influence of all *indirect* paths. To this end, the corresponding dipole matrix elements are multiplied with a numerical factor between 1 and 0, which will be called the coherent control level F_{cc} in the following. A complete suppression of the *indirect* paths as shown in figure 4.9b would thus correspond to $F_{\mathrm{cc}} = 0$, while the results of a full calculation including all possible pathways, as depicted in figure 4.9a, correspond to $F_{\mathrm{cc}} = 1$. Figure 4.10 presents false-colour plots of the calculated HH time structure $I_{\mathrm{HH}}(t)$ on the same time scale as the driving waveform (black curves) for a continuous variation of the coherent control level F_{cc} from 0 to 1. When every time trace is individually normalized (panel a), the transition between two different regimes becomes obvious: Starting with a bipolar and delayed emission for $F_{\mathrm{cc}} = 0$, a second, unipolar and synchronized contribution slowly arises with increasing coherent control level which finally dominates

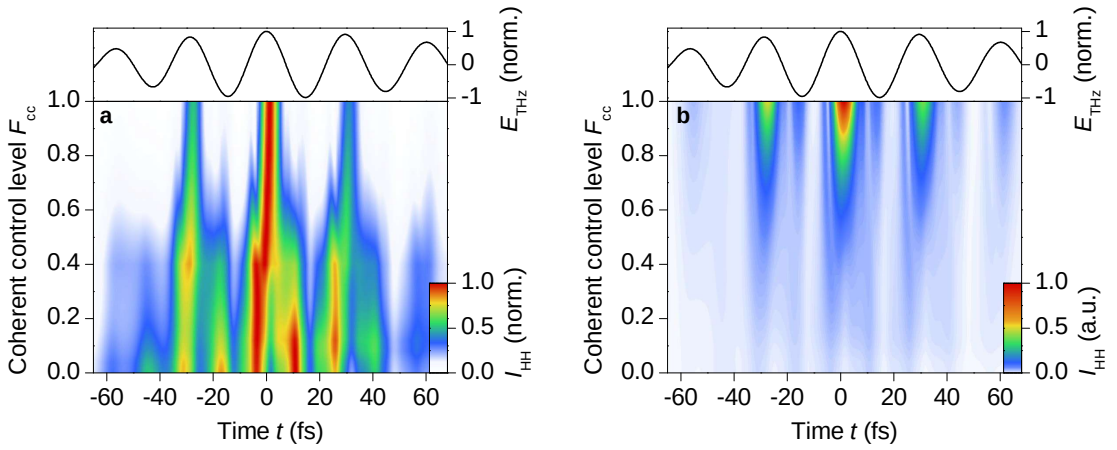

Figure 4.10: Effect of multiple polarization pathways during HHG in gallium selenide: Driving waveforms (black curves) and false-colour representations of numerically simulated high-order harmonic time traces $I_{\mathrm{HH}}(F_{\mathrm{cc}}, t)$ for a continuous variation of the coherent control level F_{cc} from 1 to 0, i.e., for a gradual switch-off of indirect polarization pathways between all five electronic bands included in the many-body model. All temporal emission profiles $I_{\mathrm{HH}}(F_{\mathrm{cc}} = \mathrm{const.}, t)$ have been normalized individually in panel a, while panel b shows the same data set normalized to the global intensity peak for $F_{\mathrm{cc}} = 1$.

the whole time trace for $F_{\mathrm{cc}} = 1$. In an intermediate region, a rich structure including bifurcations occurs. These features are caused by terahertz-induced band mixing, which modulates electronic populations and underpins the non-perturbative character of the interband excitations. The absolute efficiency of HH emission can be compared for the different cases in panel b, where all traces of $I_{\mathrm{HH}}(t)$ have been globally normalized to the peak value of $I_{\mathrm{HH}}(t)$ at $F_{\mathrm{cc}} = 1$: The gradual switch-on of *indirect* paths not only changes the temporal structure of the emitted pulse train, but also strongly enhances the HH peak intensity by a factor of almost 30. This remarkable efficiency increase can be understood by the large number of additional paths which open up between the five bands, when all *indirect* paths are permitted. Furthermore, the inter-valence band dipole matrix element $d_{\mathrm{h}_1,\mathrm{h}_2}$ has been found to be approximately one order of magnitude larger than the one bridging the fundamental band gap in gallium selenide [Seg97], which renders this transition particularly effective. The global normalization of the data shown in panel b also clarifies the origin of remaining, slightly asymmetric intermediate peaks at negative driving field half-cycles in figure 4.9a as remnants of the ballistic regime dominating the emission around $F_{\mathrm{cc}} = 0$.

Symmetry of direct and indirect polarization paths

The switch-off analysis described above strikingly underlines the importance of multiple polarization pathways during strong-field-driven HHG in gallium selenide. In particluar, a distinct dependence of the HHG efficiency on the driving field sign has been shown to arise from interfering *direct* and *indirect* polarization paths. In the following, this behaviour is qualitatively explained by an analytical comparison of the expected symmetry of the involved transition amplitudes within the minimal three-band model (see inset to figure 4.9a). The total interband transition $\mathrm{h}_1 \rightarrow \mathrm{e}$ has to be composed of both the *direct* path 1 and the *indirect* path 2. For an initially unexcited system, the microscopic polarization of the *direct* path $\mathrm{h}_1 \rightarrow \mathrm{e}$ is given by $p_k^{\mathrm{h}_1,\mathrm{e}}|_{\mathrm{direct}} \propto d_{\mathrm{h}_1,\mathrm{e}} E_{\mathrm{THz}}(t)$, where the k-dependence of the dipole matrix element has been omitted for simplicity. A significant change in the occupation of the bands given by $f_k^{\mathrm{e}}|_{\mathrm{direct}} \propto d_{\mathrm{h}_1,\mathrm{e}} (p_k^{\mathrm{h}_1,\mathrm{e}}|_{\mathrm{direct}})^* \propto d_{\mathrm{h}_1,\mathrm{e}}^2 E_{\mathrm{THz}}$ [Kir12] will react upon the polarization via $p_k^{\mathrm{h}_1,\mathrm{e}}|_{\mathrm{direct}} \propto d_{\mathrm{h}_1,\mathrm{e}} E_{\mathrm{THz}}(t) \cdot (1 - f_k^{\mathrm{e}}|_{\mathrm{direct}})$. By inserting these equations into each other, it becomes obvious that the mutual coupling between carrier occupations and the microscopic polarization leads to a series of terms which are all of **odd order** in the electric driving field E_{THz}:

$$p_k^{\mathrm{h}_1,\mathrm{e}}|_{\mathrm{direct}} \propto d_{\mathrm{h}_1,\mathrm{e}} E_{\mathrm{THz}}(t) - d_{\mathrm{h}_1,\mathrm{e}}^3 E_{\mathrm{THz}}(t)^3 + \ldots \tag{4.10}$$

The same analysis holds for the *direct* path $\mathrm{h}_2 \rightarrow \mathrm{e}$. Once a microscopic polarization between the two valence bands has been established, $p_k^{\mathrm{h}_2,\mathrm{e}}$ may mediate the *indirect* path $\mathrm{h}_1 \rightarrow \mathrm{h}_2 \rightarrow \mathrm{e}$, which consequently features a transition amplitude proportional to the product of the amplitudes of the two *direct* paths it is composed of:

$$p_k^{\mathrm{h}_1,\mathrm{e}}|_{\mathrm{indirect}} \propto [d_{\mathrm{h}_2,\mathrm{e}} E_{\mathrm{THz}}(t)] \cdot [d_{\mathrm{h}_1,\mathrm{h}_2} E_{\mathrm{THz}}(t)] = d_{\mathrm{h}_2,\mathrm{e}} d_{\mathrm{h}_1,\mathrm{h}_2} E_{\mathrm{THz}}(t)^2 \tag{4.11}$$

An analogous argumentation as for the *direct* transitions shows that this dependence is replaced by a series of **even order** terms in the electric driving field for non-perturbative strong-field excitations substantially changing electronic occupations.
The previous derivation holds for any arbitrary pair of initial and final states, i.e., electronic bands, and is valid beyond the simplification of the minimal three-band model or the limitation to the arbitrarily chosen transition $\mathrm{h}_1 \rightarrow \mathrm{e}$. In summary, *direct* polarization paths feature an odd-order transition amplitude $A_{\mathrm{direct}}(-E_{\mathrm{THz}}) = -A_{\mathrm{direct}}(E_{\mathrm{THz}})$, while the amplitude of *indirect* paths $A_{\mathrm{indirect}}(-E_{\mathrm{THz}}) = A_{\mathrm{indirect}}(E_{\mathrm{THz}})$ does not depend on the sign of the electric field. The linear superposition of both yields the total

transition amplitude

$$A_{\text{total}}(|E_{\text{THz}}|) = A_{\text{indirect}}(|E_{\text{THz}}|) + A_{\text{direct}}(|E_{\text{THz}}|) \quad \text{for} \quad E_{\text{THz}} > 0, \text{ and} \tag{4.12}$$

$$A_{\text{total}}(|E_{\text{THz}}|) = A_{\text{indirect}}(|E_{\text{THz}}|) - A_{\text{direct}}(|E_{\text{THz}}|) \quad \text{for} \quad E_{\text{THz}} < 0. \tag{4.13}$$

This asymmetry with respect to the driving field sign finally determines the HH emission efficiency via both the polarization source and the amount of free carriers available for intraband acceleration.

4.3.3 Tunability and robustness of non-perturbative quantum interference

In chapter 3, a classification of HHG in perturbative and non-perturbative regimes has been sketched. The following section will revisit this topic via an experimental and theoretical investigation of the relevant aspects in spectrally and temporally resolved HHG from gallium selenide, that permit distinguishing both regimes. In particular, the purely non-perturbative nature of the novel quantum interference will be underlined. Writing up a set of minimal requirements for such an interference to be observable will additionally facilitate a classification of the effect in a broader, general context.

Non-perturbative character of high-harmonic generation in gallium selenide

First, the non-perturbative nature of the underlying driving mechanism has been analysed by recording the efficiency of HH emission for different peak driving fields for a sample of a thickness of only 40 µm. The external peak terahertz amplitude has been adjusted from $E_{\text{peak}} = 13\,\text{MV/cm}$ to $37\,\text{MV/cm}$ by angle tuning of a pair of wire-grid polarizers, without changing the shape of the waveform or its polarization. Figure 4.11a shows the corresponing time-integrated HH spectra in the visible spectral range including harmonic orders $n = 9$ to 16 as recorded with a grating spectrograph equipped with a cooled silicon CCD (compare panel d for the exact applied field amplitudes). Panel b depicts the same data as a false-colour plot. The peak intensity of the harmonic orders $n = 9$ to 13 is plotted as a function of the peak driving field in panel c. A comparison to the dotted lines, which indicate a perturbative scaling law ($I_{\text{HH}}^{(n)} \propto E_{\text{peak}}^{2n}$), unravels a pronounced deviation with increasing peak fields. For highest driving fields, a saturation-like flattening of the efficiency curve is observed, suggesting a proportionality $I_{\text{HH}}^{(n)} \propto E_{\text{peak}}$ common to all harmonic orders under study.
The strong photoluminescence peak observed in all spectral recordings of the emitted high-order harmonics (see figure 4.11a, b) further proves the non-perturbative nature of HHG since it implies a massive carrier occupation of the conduction band, which has initially been empty in the undoped gallium selenide sample.

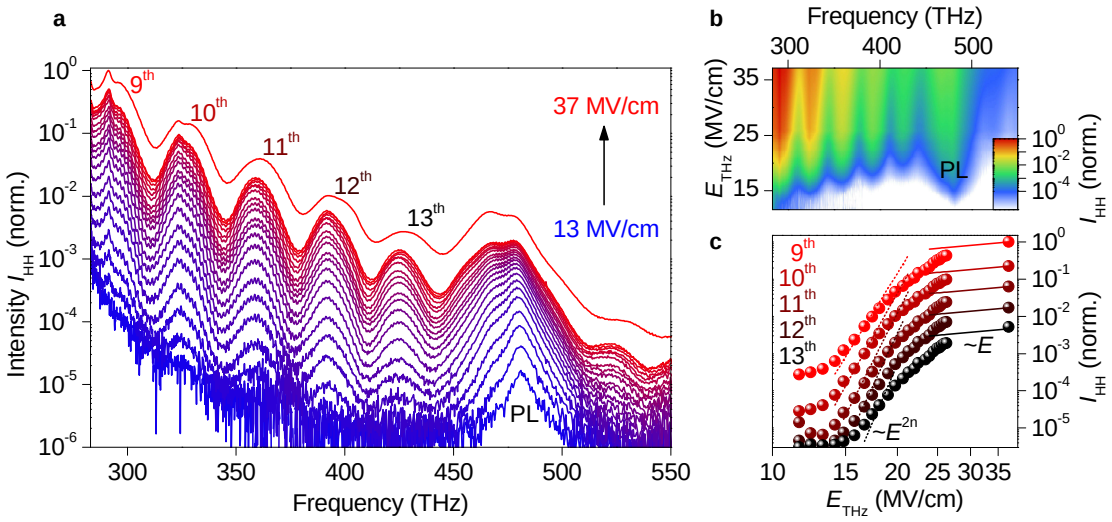

Figure 4.11: Field scaling of high-order harmonic emission from a 40-µm-thin gallium selenide crystal: a, Intensity spectra of emitted high-order harmonics in the visible spectral range for a driving waveform featuring a centre frequency of 33 THz and varying external peak field amplitudes between 13 and 37 MV/cm. Distinct harmonic orders are visible even above the photoluminescence peak (PL) marking the fundamental band gap energy of GaSe. See panel c for the exact applied peak field values. **b,** False-colour plot of the intensity spectra (shown in panel a) as a function of the peak field strength E_{peak}. **c,** Field-scaling of harmonic orders $n = 9$ to 13 as extracted from the corresponding spectral peaks shown in panel a. Dotted lines serve as guides-to-the-eye indicating a perturbative scaling, while solid lines follow a slope $I_{\mathrm{HH}}^{(\mathrm{n})} \propto E_{\mathrm{peak}}$.

Universality of the strong-field quantum interference

While the stable spectral modulation on the time-integrated spectra for different driving field strengths already hints at a robustness of the observed temporal properties of the emitted harmonics, a sophisticated study of the influence of different driving field parameters is crucial to get a comprehensive picture of the universality and tunability of this quantum interference. It is important to note that the concept does not rely on a delicate interference of perturbative multi-photon effects like one- versus two-photon absorption [Zha06], where subtle changes of the initial excitation parameters would lead to an unbalancing of the incidentally matching set of parameters and destroy the interference. In sharp contrast, the terahertz driving field is far off-resonant to any of the involved electronic transitions, since the fundamental band gap energy of gallium selenide $E_{\mathrm{g}} \approx 2\,\mathrm{eV}$ is more than 14 times higher than the terahertz photon energy. It is thus expected that the interference should be quite robust against variations in the excitation conditions. To test this scenario, the time structure of emitted harmonics has

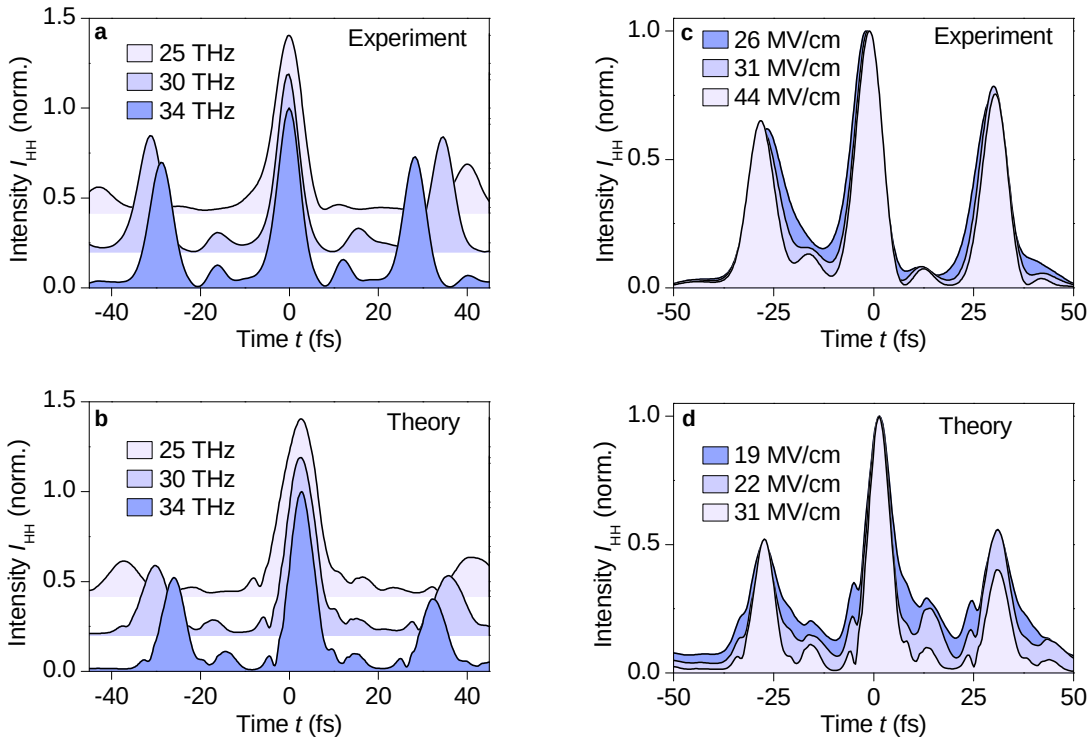

Figure 4.12: Robust strong-field quantum interference: a,b, Experimentally recorded (a) and simulated (b) time traces of the emitted HH intensity $I_{\mathrm{HH}}(t)$ for driving waveforms (not shown) featuring central frequencies of 25, 30 and 34 THz, respectively. **c,d,** High-order harmonic intensity profiles $I_{\mathrm{HH}}(t)$ for terahertz waveforms featuring a central frequency of 33 THz and external peak field strengths of 26, 31 and 44 MV/cm (a, experiment) and 19, 22 and 31 MV/cm (b, theory), respectively.

been recorded and calculated for a systematic variation of the accessible parameters of the driving field. Indeed, the characteristic features in both experimental and theoretical emission traces $I_{\mathrm{HH}}(t)$ stay absolutely robust when the fundamental frequency of the driving field is changed, as can be seen in figure 4.12a and b: While the temporal spacing of the ultrashort HH bursts increases with decreasing terahertz frequencies, the unipolar emission as well as the synchronization to the driving field crests (not shown) is preserved. The same holds true for changing the peak amplitude of the driving field (figure 4.12c and d). An increase of the visibility of the temporal intensity modulation can be seen both in theoretical and experimental time traces.

The convincing robustness against variations of the excitation parameters of the quantum interference governing the temporal emission characteristics proves its non-perturbative nature and allows for a note on the universality of the novel concept: In principle, such an interference between multiple polarization pathways may occur in a huge class of systems and materials. In solids, coherent interband polarization may simultaneously

be driven at varying wave vectors k throughout the whole Brillouin zone in the case of a strong, non-resonant driving field. In atoms or molecules, where ionization takes place at a well-defined momentum of the electron, high-harmonic interferometry has already successfully been used to extract information about the internal dynamics and structure owing to signatures of different ionization paths [Smi09, Sha09, Voz11]. Similar quantum interference effects in gaseous media may thus not be excluded in general. Nevertheless, a set of minimal prerequisites as defined in the following has to be fulfilled:

(1) The system has to include at least three energetic states (electronic bands in solids) that are mutually dipole-coupled in order to support interference between multiple pathways as sketched in the minimal three-band model (compare inset of figure 4.9a). This constraint connects the reciprocal space representation with the real-space structure of the material. It is straightforward to show that all eigenstates of an inversion-symmetric system can only possess even or odd parity. From the dipole selection rules, the dipole matrix elements connecting two states of equal parity vanish, however. It is consequently not possible to connect all three states of only two possible parities via dipole coupling. By implication, an inversion symmetric system cannot support the observed quantum interference, which may also intuitively be expected from the asymmetric emission profile as well as the occurrence of even order harmonics. As atomic or molecular gases generally exhibit long-range inversion symmetry, similar quantum interference effects should consequently only be observable macroscopically if the symmetry is broken, e.g., by pre-alignment of the molecules [RP01, Kan05].

(2) The employed electric field strengths have to be sufficiently large to non-perturbatively excite the system and thereby massively change the carrier populations within a time span shorter than one half-cycle of the driving waveform (compare discussion in section 4.3.2).

(3) The fundamental driving field has to be off-resonant to any of the involved electronic transitions. Non-perturbative high-field excitation tends to balance the weights of different possible polarization paths, since the strong field forces the electrons to oscillate between the non-resonantly coupled states.

Field-scaling of the emitted instantaneous frequency

The findings reported in the last sections shed light on the importance of coherent interband excitations during HHG in bulk solids. On the other hand, the created carriers are simultaneously accelerated through the entire Brillouin zone and Bragg-reflected at its boundaries. This highly nonlinear intraband transport in the regime of dynamical Bloch

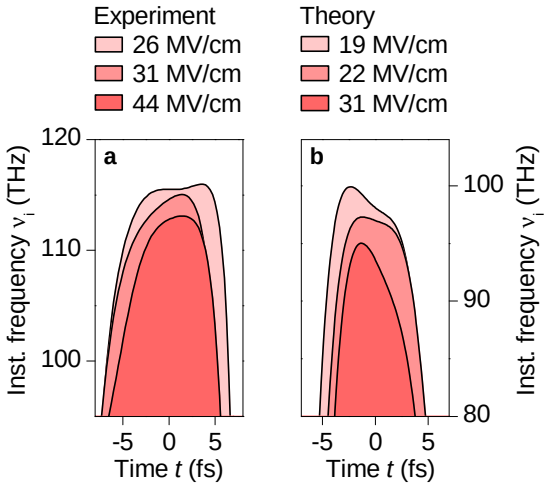

Figure 4.13: Field-scaling of the instantaneous frequency: a, Instantaneous frequency $\nu_\mathrm{i}(t)$ as extracted from the relative phase of reconstructed experimental high-order harmonic traces for driving field waveforms featuring a centre frequency of 33 THz and peak amplitudes of 26, 31 and 44 MV/cm. **b,** Theoretical counterpart of the data shown in panel a for terahertz field strengths of 19, 22 and 31 MV/cm.

oscillations still has to be regarded as a key mechanism strongly contributing to HHG. As already theoretically shown in 2008, the interplay of both inter- and intraband dynamics is responsible for a drastic enhancement of the emission efficiency. As it becomes clear from the considerations above, however, these dynamics are highly intertwined and may not be experimentally separated easily in the current setting (see chapter 7 for another experimental approach which might facilitate disentangling both [Lan16]).
Nevertheless, figure 4.7 already revealed an intriguing feature in the HH sub-cycle structure, which might be a hint to the Bloch acceleration of carriers within the bands: The instantaneous emitted frequency $\nu_\mathrm{i}(t)$ of emitted HH bursts closely follows the qualitative behaviour expected from a field dependent Bloch frequency (compare section 4.2). A remarkable trend comes to light when tracing the instantaneous frequency for different driving field strengths as shown in figure 4.13. Both in experimental recordings (panel a) as well as in theoretical calculations (panel b), the initially smooth peak of $\nu_\mathrm{i}(t)$, roughly following the driving field, gets broadened with increasing peak fields and finally morphs into a non-monotonic shape with a plateau or even a slight dip at maximum driving peak fields. While this subtle but reproducibly observable feature has not been fully understood yet, one might speculate about its microscopic origin: In an intuitive picture of accelerated Bloch electrons within the bands, an increasing Bloch frequency yields a decrease in the maximum real space excursion of the electrons. This dynamic localization would be accompanied by a decrease of the effective dipole eventually resulting in a reduced emission efficiency. For future intraband studies of lightwave-driven charge transport, it may thus be extremely interesting to study this quantity in more detail.

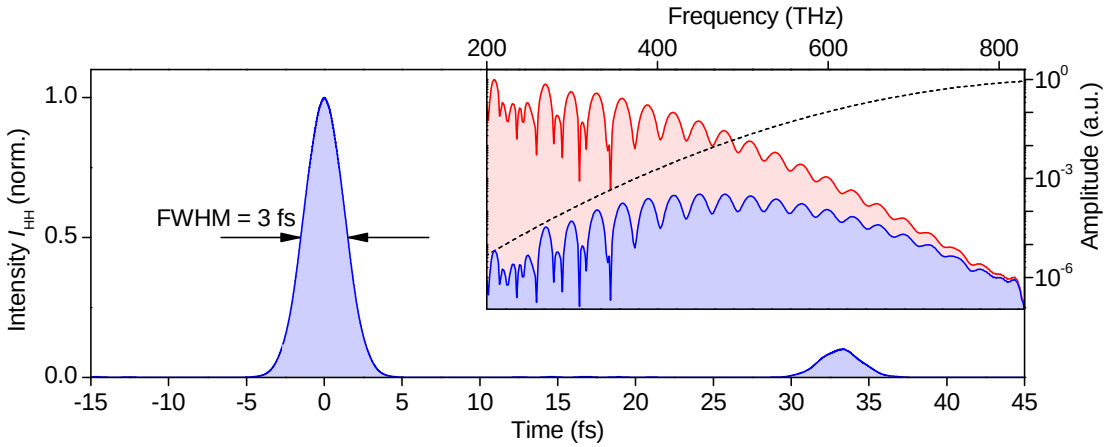

Figure 4.14: Pulse-shaping via spectral amplitude filtering: Temporal shape of high-order harmonic pulses after spectral amplitude filtering as calculated within the framework of a semiclassical intraband model (see Supplementary Information to reference [Sch14b]). Inset: Calculated HH intensity spectrum as emitted from gallium selenide (red) and after applying a spectral high-pass filter (blue). The assumed transmission curve of the filter is shown as a black dashed curve.

4.4 Sub-cycle high-order harmonic pulse shaping

The precise picture of the temporal sub-cycle structure of high-order harmonics from bulk solids presents a milestone en route towards a comprehensive understanding of the underlying quantum physics. Not only fundamental solid state physics but also conceivable photonic applications may benefit from this knowledge gain. For the 220-µm-thick sample used in the experiments of section 3.2, THz-to-HH power conversion efficiencies of approximately 7% have been measured, including all spectral components of the HH spectrum above 45 THz. This value results in HH pulse energies as high as 350 nJ, which might already be sufficient for the use as probe light in a variety of spectroscopic techniques.

As shown above, HH from gallium selenide are already emitted as ultrashort bursts without significant frequency chirp. A comparison to the quantum model, which reproduces the experimentally observed temporal structure very well, suggests that the spectral phase remains flat throughout the whole bandwidth of emitted frequencies, even beyond the experimental detection range. This inherent property sparks hope for easy-to-implement, stable few- or even sub-femtosecond sources complementing atomic-based HHG setups. An estimate of the reachable pulse lengths from HHG in gallium selenide is given on the basis of a straightforward model describing the field-driven intraband transport of a single electron following Bloch's theorem (equation (3.4), see Supplementary Information of reference [Sch14b] for details). Knowing about the limitations of this

model (see above), it might still be sufficient to get an estimate of the possible pulse lengths. By the example shown in figure 4.14, suitable spectral filtering of broadband high-order harmonics emitted from gallium selenide may already enable pulse durations on the order of only 3 fs without external compression. Note that the observed high-frequency edge of time-integrated HH spectra from gallium selenide is likely only set by the bandwidth and dynamical range of the detectors employed here. While HH orders up to $n = 47$ at a frequency exceeding 1000 THz have been observed from tungsten diselenide [Lan16] employing the multi-THz source explained here, HH from wide-gap semiconductors or dielectrics support even higher photon energies [Ghi14, Luu15].
The versatility of the multi-THz source which has been introduced in chapter 2 additionally submits shaping the sub-cycle structure of emitted harmonics. While the temporal spacing of the ultrashort bursts is given by the applied frequency of the fundamental waveforms, the peak field amplitudes of the latter reproducibly set the sub-cycle relative phase of emitted harmonics, as shown in figure 4.13. The number of emitted bursts can be defined by the pulse length, i.e., the number of driving half-cycles of the employed transient. Dispersion-managed difference frequency generation leading to single-cycle strong-field waveforms [Jun10] may thus be exploited to produce isolated, ultrashort HH bursts without the need for external gating techniques [Chi14] frequently used in attosecond pulse generation schemes based on atomic HH sources.
The few-cycle waveforms demonstrated here, however, enable us to control the precise timing of the emitted pulse train via tuning the carrier-envelope phase ϕ_{CEP} of the multi-terahertz waveforms. Figure 4.15a depicts a false-colour representation of recorded HH intensity envelopes $I_{\mathrm{HH}}(t)$ for a continuous variation of ϕ_{CEP}. Starting from a pulse train featuring three symmetrically arranged HH bursts for $\phi_{\mathrm{CEP}} = 0, 2\pi, \ldots$ (see also panel b), the pulse train temporally shifts under a common envelope defined by the intensity shape of the driving waveform. For $\phi_{\mathrm{CEP}} = \pi, 3\pi, \ldots$, which corresponds to a sign-flip of the multi-THz transient, the emitted HH pulse train consequently features a complementary intensity trace (figure 4.15b). Extracting the carrier envelope phase change from the HH traces shown in panel a by comparing the timing of their peak values with respect to the one extracted for $\phi_{\mathrm{CEP}} = 0$ underlines the precision of this procedure. The determined CEP values (red dots in figure 4.15c) closely line up on the expected linear dependence (black dashed line) on the incremental steps of the piezo delay stage used to adjust ϕ_{CEP}.

The revealed temporal structure of emitted harmonics from bulk gallium selenide brings the practical use of few-femtosecond solid-state high-harmonic sources into reach. The unique tuning possibilities introduced in the preceding section furthermore spark hope for unparalleled sub-cycle pulse shaping of ultrabroadband waveforms for phase-locked

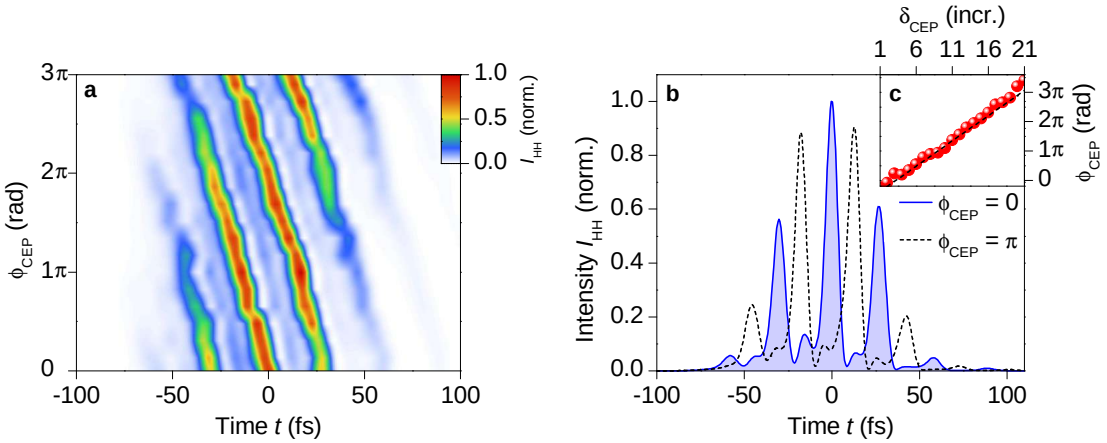

Figure 4.15: CEP-control of sub-cycle timing during HH emission: a, False-colour representation of reconstructed experimental traces of the HH intensity envelope $I_{\mathrm{HH}}(t)$ for a continuous variation of the carrier-envelope phase ϕ_{CEP} of the driving multi-THz waveforms. **b,** Selected HH intensity envelopes for $\phi_{\mathrm{CEP}} = 0$ (blue shaded) and $\phi_{\mathrm{CEP}} = \pi$ (black dashed). **c,** Carrier-envelope phase ϕ_{CEP} as extracted from the timing of the HH peaks in panel a (red dots). The black dashed line represents a linear scaling as expected from the step by step increment δ_{CEP} of the piezo delay stage used for precise CEP-tuning (compare figure 2.8).

spectroscopy. On a more fundamental level, the novel insights into the coupled dynamics of coherent interband excitation and simultaneous intraband acceleration mark a milestone on the route towards a complete quantum picture of strong-field-driven solid-state high-order harmonic generation.

Chapter 5

Polarization and orientational symmetry of strong-field-driven harmonics

Except for the time-resolved study introduced in the previous chapter, the few experimental studies of solid-state HHG [Ghi10, Vam15a, Luu15] have always been performed in the frequency domain so far, i.e., only the spectral features of emitted harmonics have been captured. In gallium selenide, high-order harmonic generation driven by strong terahertz fields has been shown to rest upon anharmonic intraband carrier dynamics (chapter 3, [Sch14b]) and non-resonantly driven interband polarization via several interfering quantum paths (chapter 4, [Hoh15a]). In a further step, the ability to combine frequency- and time-resolved measurements shall now be exploited to connect specific features of HHG to the crystal structure of the sample. In perturbative nonlinear optics, the crystal symmetry is straightforwardly connected to the occurrence of distinct nonlinear optical processes [Boy03]. Analogous symmetry arguments have not yet been established for non-perturbative solid-state HHG, in contrast.

The following chapter introduces the first comprehensive study of the dependence of solid-state HHG on the crystallographic orientation of the sample. Intriguing properties of HH emission along certain high-symmetry directions in gallium selenide are unveiled and studied in detail. Bringing together frequency-, time- and finally also polarization-resolved experimental recordings allows for drawing a conclusive picture of HHG along different crystallographic directions. In light of an intuitive model based on well-known concepts borrowed from so-called frequency combs, initially surprising experimental results can be understood and reproduced with good quantitative agreement. Finally, a first discussion on the applicability and limitations of perturbatively assigned symmetry arguments is given.

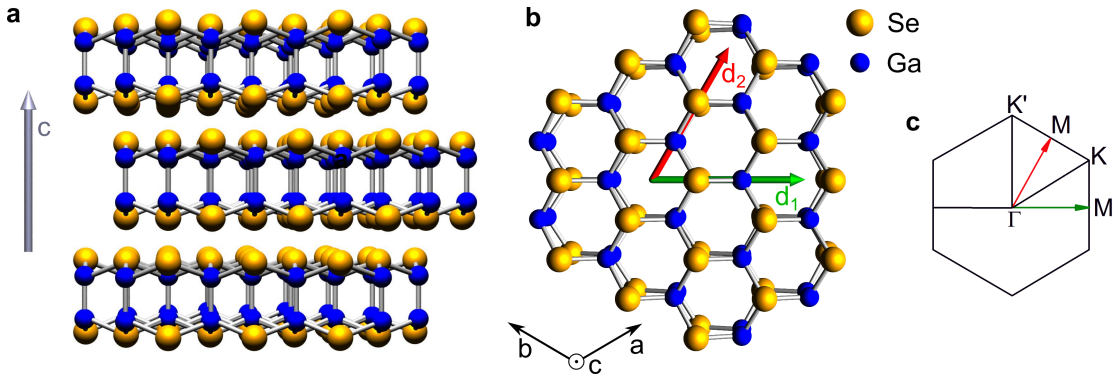

Figure 5.1: Crystal structure of ε-type gallium selenide: a, Schematic illustration of the hexagonally structured layers of gallium selenide, each consisting of two sheets of gallium atoms (blue) sandwiched between two sheets of selenium atoms (yellow). The shown stacking sequence along the crystallographic c-axis defines the polytype ε-GaSe used here. **b,** In-plane structure of GaSe with the equivalent Bravais lattice vectors a and b (black arrows). The directions along the in-plane projections of the connection between neighbouring Ga and Se atoms are highlighted by the green (d_1) and the red arrow (d_2). **c,** Sketch of the hexagonal Brillouin zone of GaSe with the related high-symmetry directions connecting the Γ-point with the M-point shown in corresponding colours.

5.1 The crystal structure of gallium selenide

Gallium selenide features a hexagonal crystal lattice [Kuh75, Fer94] and consists of single layers which are composed of two sheets of gallium atoms sandwiched between two sheets of selenium atoms (see figure 5.1). While the bonds between neighbouring atoms within the layers are of strong, covalent nature, the interlayer coupling along the crystallographic c-axis (grey arrow in figure 5.1a) is comparably weak and mediated by van-der-Waals forces only. This structural anisotropy exclusively facilitates cleaving thin sheets of GaSe with surfaces perpendicular to the c-axis, which is also the orientation of all samples studied here. A single layer of GaSe features D_3^{h}-symmetry and thus does not possess inversion symmetry. The stacking order of the layers along c defines different polytypes of gallium selenide. The samples used here belong to the polytype ε-GaSe, which exhibits A-B-A...-stacking, as depicted in figure 5.1a. This type of GaSe still belongs to the symmetry group D_3^{h}, i.e., it features a three-fold rotational symmetry around the c-axis and a horizontal (in-plane) mirror plane. It is thus sufficient to discuss relevant symmetry arguments by reference to a single layer of GaSe only (see figure 5.1b). The in-plane geometry is commonly described with the aid of the equivalent lattice vectors **a** and **b** of the hexagonal Bravais lattice (see black arrows). For the following discussion, however, it is most convenient to define two in-plane directions d_1 and d_2

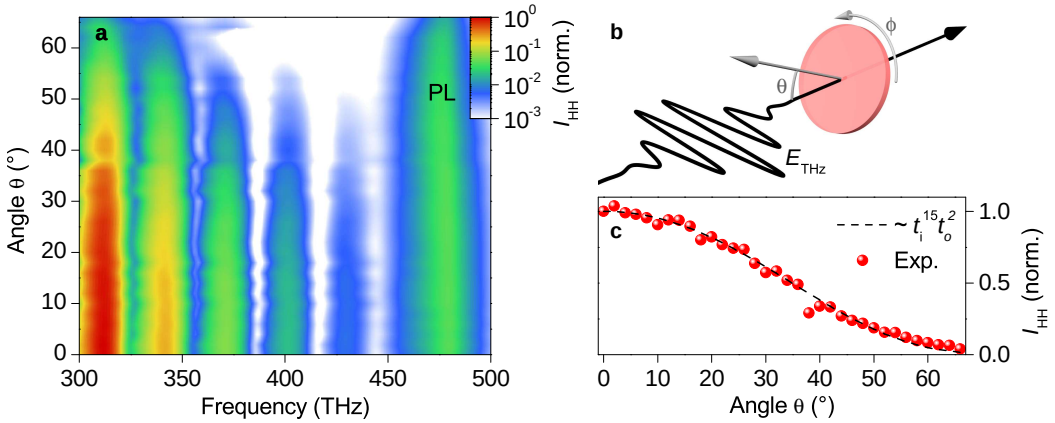

Figure 5.2: High-order harmonic emission as a function of the angle of incidence θ: a, False-colour representation of emitted high-order harmonic intensity spectra I_{HH} from a 40-µm-thin gallium selenide sample as a function of the angle of incidence θ as defined in the schematic in panel b. PL: photoluminescence peak around 476 THz. **b,** Illustration of the experimental geometry defining the angle of incidence θ and the in-plane azimuthal angle ϕ. **c,** Spectrally integrated intensity I_{HH} as extracted from the data shown in panel a (red dots) and normalized to the intensity measured for $\theta = 0°$. The black dashed curve follows the theoretically estimated intensity evolution for a HHG field-scaling $I_{\mathrm{HH}} \propto E_{\mathrm{THz}}^{15}$ and for taking into account the dependence of transmission coefficients $t_{\mathrm{i}}, t_{\mathrm{o}}$ at the facets of the GaSe window on the angle of incidence θ.

perpendicular to these lattice vectors pointing along the in-plane projections of the connection between two neighbouring but different atoms, i.e., along the Ga-Se axis or vice versa (see red and green arrows). Note that due to the 120° symmetry, these two directions are equivalent to the inverse of each other, i.e., pointing along d_1 is the same as pointing along $-\mathrm{d}_2$. The corresponding high-symmetry directions may consequently not be distinguished in reciprocal space, where they connect the Γ-point with neighbouring M-points of the hexagonal Brillouin zone (figure 5.1c).

5.2 Variation of the angle of incidence

For an in-depth understanding of the influence of the sample's crystallographic orientation on the HHG mechanism, the first step is to exclude macroscopic propagation effects in the sample like phase matching, which would conceal the microscopic behaviour. To this end, HH intensity spectra in the visible spectral range have been recorded with a grating spectrograph and a silicon CCD camera, while the angle of incidence θ (compare schematic illustration of the experimental setting in figure 5.2b) has been continuously varied[1]. Figure 5.2a shows a colour-coded map of the collected spectra as a function of θ.

[1]The in-plane angle ϕ has been adjusted for highest HHG efficiency (compare section 5.3).

The comb of high-harmonic peaks is clearly visible and a gradual decrease of the emitted intensity is found for all orders with increasing angle of incidence. This behaviour is in sharp contrast to the experimental observation in references [Sch14b, Sch14a], where a 220-µm-thick GaSe window has been used and the HH intensity got enhanced with growing angle θ due to phase matching effects, which were found to play a significant role in these comparably thick samples. Here, the sample under study features a thickness of only 40 µm which seems to be sufficiently thin to avoid any phase matching effects. This assumption is further corroborated by an estimate of the reduction in HHG efficiency due to increasing reflection losses at the facets of the sample for higher angles of incidence: The transmission coefficients for the terahertz field at the entrance facet t_i and the HH field at the rear facet t_o may be derived from the Fresnel equations for s-polarized waves. The refractive index of GaSe is known in the multi-THz and visible spectral range [Kat13] and has been set to $n_\mathrm{HH} = 2.86$ as an average value for the emitted harmonics (value corresponds to a wavelength of 800 nm) and $n_\mathrm{THz} = 2.70$ for the driving field centred at a frequency of 34 THz. When the field-dependence of HHG on the internal driving field within the sample, i.e., the field after reflection losses at the entrance surface, is used as a fit-parameter, the overall emitted HH intensity can be quantitatively well reproduced as a function of the angle of incidence (see figure 5.2c). The resulting dependency $I_\mathrm{HH} \propto E_\mathrm{THz}^{15}$ represents a reasonable power-law for intermediate peak-fields, as corroborated by a comparison to the experimental data shown in figure 4.11. Along with the observed polarization behaviour of emitted harmonics (see section 5.3.3), these findings imply that phase matching effects can be explicitely excluded and suggest that the reduced HH emission with growing angles of incidence may purely be related to higher reflection losses at the sample facets. All experiments described before this section and in the following have been performed under normal incidence ($\theta = 0°$).

5.3 Harmonic generation along different in-plane directions

5.3.1 Angular dependence in the frequency domain

As a next step towards a comprehensive investigation of the crystallographic influence on HHG, the strong-field terahertz bias may be applied along different in-plane directions. For this purpose, the GaSe window has been placed in a rotation mount to be able to vary the azimuthal angle ϕ as defined in figure 5.2b, while the angle of incidence has been kept constant at $\theta = 0°$.

In a first experiment, the crystallographic orientation of the sample has been determined via recording the generated second harmonic intensity as a function of ϕ. To this

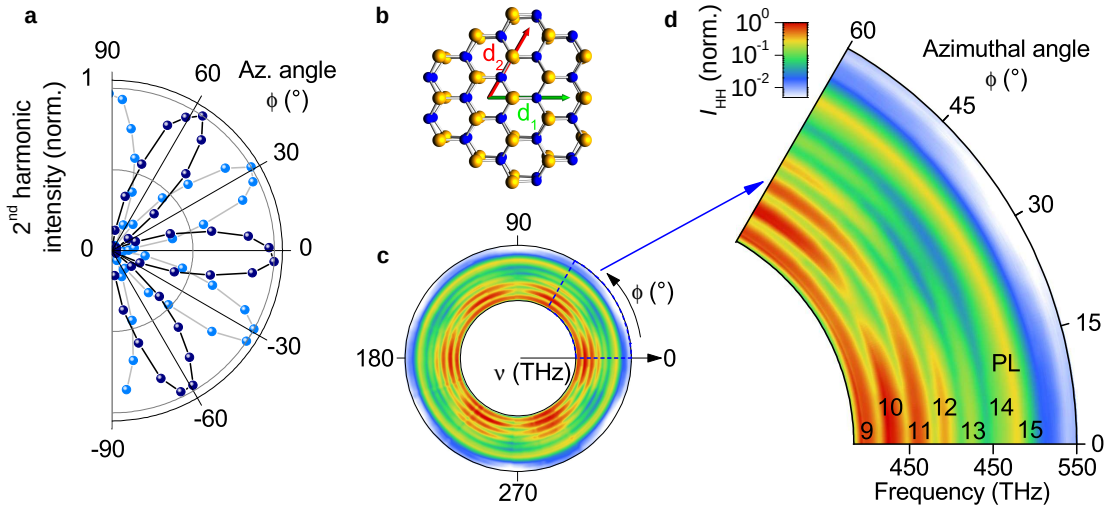

Figure 5.3: Dependency of HHG on the in-plane crystal direction in GaSe: a,b, Measured intensity (a) of the parallel (dark blue dots) and perpendicular (bright blue dots) polarization component of the emitted second harmonic intensity as a function of the azimuthal angle ϕ, as depicted in figure 5.2b. $\phi = 0°$ corresponds to a driving field polarization along the d_1-direction (compare orientation of hexagonal lattice sketched in panel b). *Parallel* (*perpendicular*) refers to an angle of 0° (90°) between the polarizations of the fundamental and the second harmonic wave. **c,d,** Colour-coded polar plot of high-order harmonic spectra as a function of ϕ for a full rotation of the sample, i.e., ϕ is varied from 0° to 360° (c), and zoom-in to the data for a sector $\phi = 0° \ldots 60°$ (d). Numerals denote the harmonic orders; PL marks the photoluminescence peak.

end, a suitable spectral bandpass has been set in the beam path of emitted harmonics, which consists of a combination of a sapphire crystal and a calcium fluoride window blocking the fundamental terahertz transient, and an indium arsenide waver absorbing the higher-order harmonics. Additionally, a wire-grid polarizer has been used to analyse the polarization of the second harmonic. The result is summarized in figure 5.3a, showing the emitted second harmonic intensity in dependence of the in-plane angle ϕ for both polarizations, parallel (dark blue) and perpendicular (bright blue) to the incident waveform. A six-fold symmetry for both polarization directions becomes obvious, which matches the rotational symmetry of the crystal lattice. Note that the field-profile of the second harmonic, which is not resolved here, changes its sign every 60 degrees, thereby lowering the symmetry to D_3^{h}. From a comparison of the emitted polarization to the expected behaviour [Cat78] following the nonlinear $\chi^{(2)}$-tensor of GaSe, which can be easily derived from its point group symmetry (compare appendix D), the orientation of the crystal may be determined up to a remaining uncertainty of 60° owing to the six-fold symmetry of the observed signals. Figure 5.3b again depicts the crystal lattice of GaSe (compare figure 5.1), whose orientation is matched to the data shown in panels

a, c and d. The azimuthal angle ϕ is consequently defined such that $\phi = 0$ implies that the driving field polarization is oriented along the direction d_1 defined above. More precisely, a distinction between d_1 and d_2 is not possible in the current experimental setting. For simplicity and without loss of generality, however, $\phi = 0°$ will be discussed as the d_1-direction from now on.
The HHG efficiency in dependence on the in-plane crystallographic direction may now be determined by removing the spectral filters and recording emitted HH intensity spectra in the visible spectral range via a grating spectrograph and a cooled-silicon CCD camera. The high quality of the cleaved sample surfaces enables recording a full 360°-scan of emitted spectra even if the focal spot may slightly move on the sample during rotation. The corresponding data set depicted in a false-colour representation in figure 5.3c clearly reflects the global six-fold symmetry expected from a sign-independent measurement. The repeated behaviour of the emitted high-order harmonic intensity can be analysed in greater detail based on the zoom-in to the sector between $\phi = 0°$ and $\phi = 60°$ given in figure 5.3d. High-order harmonics of orders $n = 9$ to 13 can be distinguished below the band gap energy of GaSe, while the 14^{th} and 15^{th} orders are dominated by the photoluminescence peak around 476 THz. Remarkably, the emitted HH intensity of all orders peaks when the driving field points along the d_1- or the d_2-direction, while a decrease of the HH efficiency is observed for intermediate directions with a minimum for $\phi = 30°$. During the experiments described in chapter 4, the driving terahertz field has always been applied along $\phi = 0°$ or equivalent crystallographic directions, where the emitted HH intensity gets maximized. While all orders are suppressed by several 10% along $\phi = 30°$, a slightly stronger decrease might be conjectured for even order harmonics compared to the odd orders, which will be discussed in more detail in section 5.4. Importantly, both even and odd order harmonics are observed, irrespective of the in-plane orientation ϕ, i.e., the modulation of the emitted spectra always features a periodicity exactly corresponding to the fundamental driving frequency ν_{THz}.

5.3.2 Angular dependence in the time domain

The experimental observations in the frequency domain discussed in the previous section may suggest that the quantum interference as the mechanism responsible for the asymmetry in temporal HH traces and thus the appearance of even orders (compare chapter 4), occurs irrespective of the in-plane orientation of the sample. To check this assumption, a time-resolved study of the dependence on the azimuthal angle is crucial. Therefore, cross-correlation experiments as described in detail in section 4.1.1 have been performed for the relevant sector of in-plane angles between $\phi = 0°$ and $\phi = 60°$. The spectrally integrated intensity $I_{\text{SF}}(t)$ of the sum-frequency signal of high-order harmon-

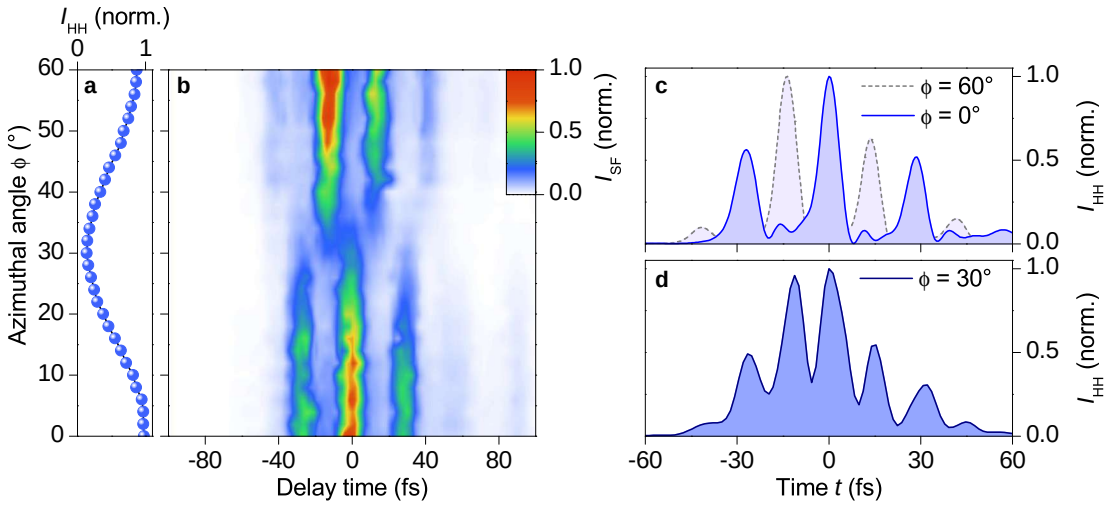

Figure 5.4: Time-resolved study of HHG along different in-plane crystal directions: a, Absolute HH intensity I_{HH} as extracted by spectral integration of the data shown in figure 5.3d as a function of the in-plane angle ϕ. **b,** Colour-coded time traces of the spectrally integrated cross-correlation signal (intensity I_{SF} of the sum-frequency signal of HH and gating pulses, compare section 4.1.1) as a function of the azimuthal angle ϕ. **c,d,** Reconstructed temporal HH intensity envelopes for $\phi = 0°$ (c, solid curve), $\phi = 60°$ (c, dashed curve) and $\phi = 30°$ (d).

ics and the gating pulse is presented as a function of the azimuthal angle ϕ in figure 5.4b. These time traces of the cross-correlation signal already exhibit some fascinating properties: Consistent with the time-integrated measurements discussed above (the spectrally integrated HH intensity is shown in panel a for comparison), the sum-frequency signal decreases about almost one order of magnitude when the crystal is rotated from $\phi = 0°$ to $\phi = 30°$. Furthermore, the polarity of the emitted HH pulse train seems to change between the two high-efficiency regions around $\phi = 0°$ and $\phi = 60°$, as corroborated by the reconstructed high-order harmonic time traces shown in panel c. While three dominant peaks of $I_{\mathrm{HH}}(t)$ are observed for $\phi = 0°$, only two prevailing peaks in-between the initial ones are visible for $\phi = 60°$. This observation nicely reflects the in-plane crystal symmetry of GaSe (compare figure 5.1b). As explained above, switching from $\phi = 0°$ to $\phi = 60°$, i.e., from direction d_1 to d_2, is equivalent to an in-plane rotation about 180°. This, in turn, is analogous to changing the sign of the driving waveform, for instance by changing the carrier-envelope phase of the latter by π, a scenario shown in figure 4.15.

A surprising behaviour of the HH time traces is observed in the intermediate, low-efficiency region around $\phi = 30°$, however. As can be seen in figure 5.4d, $I_{\mathrm{HH}}(t)$ peaks for every half cycle of the driving waveform centred at a frequency of 33 THz (not shown),

with a temporal spacing of only 15 fs. At first sight, this observation is at odds with the observed spectral features: By the principles of Fourier transformation, a temporally periodic signal with periodicity $T/2$, where T is the fundamental terahertz period, yields a spectrum featuring a modulation of periodicity $1/(2T) = 2\nu_{\mathrm{THz}}$. In contrast to this expectation, however, all recorded spectra presented in figure 5.3d show a modulation with periodicity ν_{THz}. This obvious discrepancy hints to the existence of another piece of the puzzle, which has not been incorporated yet. As demonstrated in the following section, analysing the polarization of HH from gallium selenide - a degree of freedom that has not been discussed thoroughly, so far - will help to resolve this alleged contradiction.

5.3.3 Polarization of emitted harmonics

No experimental study of the polarization of high-order harmonics from bulk solids has been reported, so far. Here, a Glan-Thompson polarizer is placed in front of the spectrograph, which serves as an analyser for polarization-resolved spectral recordings of high-order harmonics in the visible domain. Similar to the measurement discussed in figure 5.3, different in-plane angles ϕ have been adjusted by rotating the sample about its crystallographic c-axis, while the analyser has additionally been rotated by 180° for every single setting of ϕ. Following this scheme, the peak intensity values of harmonic orders $n = 9$ to $n = 13$ have been extracted from the measured spectra for every combination of the in-plane angle and the analyser setting. Along $\phi = 0°, 60°, 120°, \ldots$ the polarization of all harmonic orders is found to follow the polarization of the driving field. The radial intensity distribution of the 10^{th} and 11^{th} harmonics is shown in figure 5.5a as an example, while other recorded harmonic orders feature the same polarization. A very intriguing behaviour can be observed for intermediate angles. When changing the azimuthal angle of the sample, the polarization of odd order harmonics stays the same, i.e., remains parallel to the fundamental field direction. The polarization of even order harmonics, in contrast, is gradually rotated out of the initial, parallel polarization direction (see also figure 5.7) and finally lies perpendicular to the driving field for $\phi = 30°$ as depicted in figure 5.5b.

At this juncture, the findings of the preceding sections may have to be reconsidered. In particular, emitted high-harmonics for a driving field oriented along $\phi = 30°$ have been shown to feature a variety of unexpected properties. In section 4.1.1, the subcycle emission characteristics have proven that a smooth and broad spectrum is emitted during individual half-cycles of the driving field. The spectral modulation observed in time-integrated HH spectra, forming the typical comb of distinct harmonic orders, arises from averaging over repeated emission events. The appearance of differing polarizations of different harmonic orders does not seem to be compatible with this picture at first

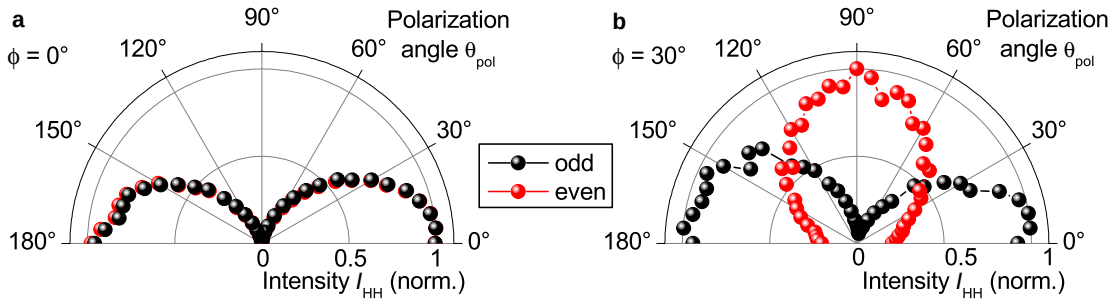

Figure 5.5: Polarization of high-order harmonics from GaSe: Polar diagram of the measured radial intensity distribution of harmonics of order $n = 10$ (red) and $n = 11$ (black) for a driving field polarization oriented along $\phi = 0°$ (a) and $\phi = 30°$ (b). The polarization angle is determined by adjusting the orientation of the analyser (Glan-Thompson polarizer) in front of the spectrograph and is defined such that 0° corresponds to horizontal polarization, i.e., parallel to the driving field direction.

glance. Furthermore, the periodicity of temporal HH traces of $T/2$ instead of T along $\phi = 30°$ seems to be at odds with the spectral modulation with a periodicity of ν_{THz} observed in time-integrated recordings. While these observations might seem to question the picture of HHG in gallium selenide developed so far, the following section will introduce a straightforward model based on concepts borrowed from the established frequency comb which will be able to reconcile the apparent contradictions and further corroborate the implications derived up to now.

5.4 Frequency-comb analysis of high-order harmonics

Bringing together the findings of frequency-, time- and polarization-resolved measurements of the emitted harmonics will draw a conclusive picture of HHG in different crystallographic directions in gallium selenide. To this end, concepts well-known from frequency combs (compare section 2.6) are employed to explain the rich features in the angle-resolved measurements discussed in the preceding sections.

First, the basic findings and conclusions stated so far for the comparably well-understood scenario along the most efficient crystal directions shall be recapitulated here. The time-resolved study of HHG in GaSe exposes a novel strong-field quantum interference between different ionization paths which leads to a strong asymmetry in the emission, i.e., dominant HH bursts are emitted during every second half-cycle of the driving field only. The assignment to the in-plane crystallographic directions via the polarization-resolved second harmonic emission (section 5.3) allows for rephrasing this condition and connect it to the crystal structure in a simplified way: Without loss of generality, one may state that HH emission is strongly enhanced when the driving field vector

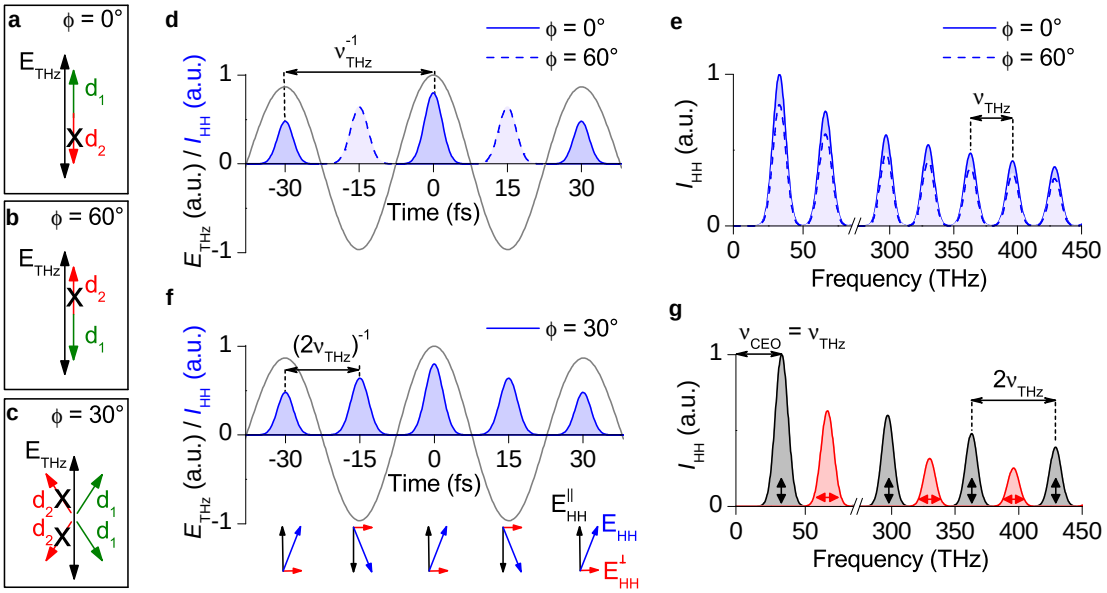

Figure 5.6: Schematic illustration of the frequency comb model of HHG: a-c, Vectorial sketches of the scenario for a driving field polarization (E_{THz}, black arrow) along $\phi = 0°$ (a), $\phi = 60°$ (b) and $\phi = 30°$ (c). **d,** For $\phi = 0°$ ($\phi = 60°$), only positive (negative) half-cycles of the driving field (grey curve), i.e., when the field vector points along the d_1-direction, contribute to HH emission. Both cases result in a unipolar pulse train (I_{HH}, blue) with a temporal spacing of the HH bursts of $1/\nu_{\mathrm{THz}}$. **e,** The Fourier transforms of the HH field corresponding to the cases shown in panel d both form a frequency comb of even and odd orders (spectral periodicity ν_{THz}). **f,** For $\phi = 30°$, every half-cycle of the driving field (grey curve) exhibits a vector component along one of the d_1-directions (compare panel c), resulting in a bipolar pulse train I_{HH} (blue shaded) with a periodictity of $1/(2\nu_{\mathrm{THz}})$. The HH field vector E_{HH} consequently switches between these d_1-directions for subsequent driving half-cycles, resulting in polarization components parallel ($E^{\parallel}_{\mathrm{HH}}$, black arrows) and perpendicular ($E^{\perp}_{\mathrm{HH}}$, red arrows) to the fundamental field. **g,** The corresponding Fourier transforms of the polarization components both form a frequency comb of periodicity $2\nu_{\mathrm{THz}}$ with carrier-envelope offset frequencies $\nu_{\mathrm{CEO}} = 0$ ($\nu_{\mathrm{CEO}} = \nu_{\mathrm{THz}}$) for the perpendicular (parallel) component. Double arrows depict the polarization of the spectral peaks.

points along the d_1-direction defined in figure 5.1b and is strongly suppressed for the opposite direction, which is equivalent to d_2. This straightforward scenario is depicted in figure 5.6a and b for the two cases $\phi = 0°$ and $\phi = 60°$, respectively. When the field E_{THz} (black arrow) is positive (negative) in case a (b), HH emission occurs, while it is suppressed along the opposite directions. Both scenarios thus lead to HH pulse trains $I_{\mathrm{HH}}(t)$ with a temporal spacing between the bursts corresponding to $\Delta\tau = 1/(\nu_{\mathrm{THz}})$, which are temporally offset by one half-cycle with respect to each other (see figure 5.6d). As explained in section 2.2.2, a train of subsequent femtosecond pulses emitted with a

certain repetition rate will feature a series of well-defined lines in the Fourier domain separated by this repetition rate - the so-called frequency comb. Here, the HH bursts are emitted with a repetition rate given by the fundamental terahertz frequency. Consequently, the Fourier transform of the HH pulse train forms a frequency comb of spacing ν_{THz} as shown schematically in figure 5.6e. Note that the width of the comb teeth decreases with an increasing number of pulses. Due to the appearance of maximally three dominant HH bursts, the temporal interference leads to relatively broad harmonic peaks compared to the usually narrow comb lines observed in ordinary frequency combs. So far, this model is perfectly in line with the observed behaviour of emitted harmonics along $\phi = 0°$ and $60°$ without the need for any further assumptions not yet corroborated by the experimental findings: In both directions, a unipolar emission is observed, while the polarity alternates when switching between the two angles (compare figure 5.4), both even and odd order spectral peaks are observed in time-integrated recordings (compare figure 5.3) and the polarization of the HH pulse train is expected to follow the fundamental driving field orientation (compare figure 5.5).
To explain the interesting regime along $\phi = 30°$, an assumption shall be stated for the moment, which will be justified retrospectively in the conclusion. Starting from the premise that the condition of dominant HHG along the three equivalent d_1-direction is exclusive, i.e., they are the **only** in-plane directions contributing to HHG, a vectorial scenario ma be drawn also for the case of the fundamental driving field pointing along $\phi = 30°$ (figure 5.6c). The three-fold in-plane symmetry ensures that one of the equivalent d_1-directions may be addressed by a vector component of the driving field for every half-cycle, irrespective of its sign. Consequently, HH emission should occur in a bipolar way, i.e., with a temporal periodicity $\Delta\tau = 1/(2\nu_{\mathrm{THz}})$ as depicted in figure 5.6f. The HH field vector E_{HH} (blue arrows), however, does not follow the driving field in this scenario but rather bounces between the two neighbouring d_1-directions for subsequent half-cycles. Analysing the polarization of the pulse train thus leads to contributions both parallel (black arrows) and perpendicular (red arrows) to the driving field direction. In the Fourier domain, these polarization components both form a frequency comb of periodicity $2\nu_{\mathrm{THz}}$ (panel g). A closer look on the behaviour of both polarization vectors reveals an additional feature which is connected to a property of frequency combs neglected so far, however: While the perpendicular (red) polarization vector always points along the same direction, the parallel one (black) changes its sign from burst to burst. This sign-flip corresponds to a slip of the carrier envelope phase of $\Delta\phi_{\mathrm{CEP}} = \pi$ between two subsequent HH pulses, which defines the carrier envelope offset frequency $\nu_{\mathrm{CEO}} = \nu_{\mathrm{THz}}$ (compare section 2.2.2). The full Fourier domain representation of the pulse train thus consists of two intermeshed, perpendicularly polarized frequency combs featuring the same spectral periodicity but different carrier-envelope

offset frequencies. In spectral recordings of emitted HH along $\phi = 30°$, these interlinked combs appear as a single one featuring a spacing ν_{THz}.
This straightforward model is indeed capable of capturing all qualitative experimental observations in time-, frequency- and polarization-resolved recordings. First, the alleged discrepancy between the temporal and spectral modulation is solved: Irrespective of the polarization component under study, HH time traces along $\phi = 30°$ should always be bipolar, as observed in figure 5.4. In spectral recordings without polarization sensitivity as discussed in figure 5.3d, however, a frequency comb of spacing ν_{THz} is expected to be observed. Furthermore, the polarization of even order harmonics is supposed to be perpendicular to the polarization of the driving field and the odd order harmonics, as shown in figure 5.5.

5.4.1 Quantitative modelling of the HH frequency comb

The model sketched above has shown to reproduce all qualitative features of the orientation-dependent HH emission observed in the experiment so far and suggests a quite surprising behaviour: Along certain crystal directions, the single HH bursts emitted during subsequent half-cycles of the driving field alternate between two different polarization directions differing by 60°, none of them oriented along the fundamental driving field polarization. To check the validity of this scenario, a quantitative analysis of HH emission along all in-plane directions based on the frequency comb model is performed in the following.
For the above-mentioned assumption that HHG exclusively occurs for a driving field polarization parallel to the d_1-direction, the projection of the terahertz field E_{THz} onto the two equivalent d_1-directions is determined for an arbitrary in-plane angle ϕ (see figure 5.7a and inset to panel b). For a quantitative analysis, the experimentally observed field-scaling of high-order harmonic emission (compare figure 4.11) is extracted for different HH orders. Numerical interpolation of this curve facilitates connecting the field projection for different azimuthal angles with the emitted HH intensity (see figure 5.7b). This straightforward test already reveals a good match between the expected HH intensity and the HH emission efficiency as extracted from the spectral recordings shown in figure 5.3d.
In order to test the validity of the frequency comb model, the emitted HH pulse train is artificially recreated numerically. To this end, the electric field of a series of ultrashort pulses centred at a frequency of 375 THz with Gaussian envelopes is generated for both signs of the terahertz field individually. The intensity of the artificial HH bursts is controlled via the driving field projections along the equivalent d_1-directions multiplied by the extracted field-scaling and is adjusted to follow the experimentally observed

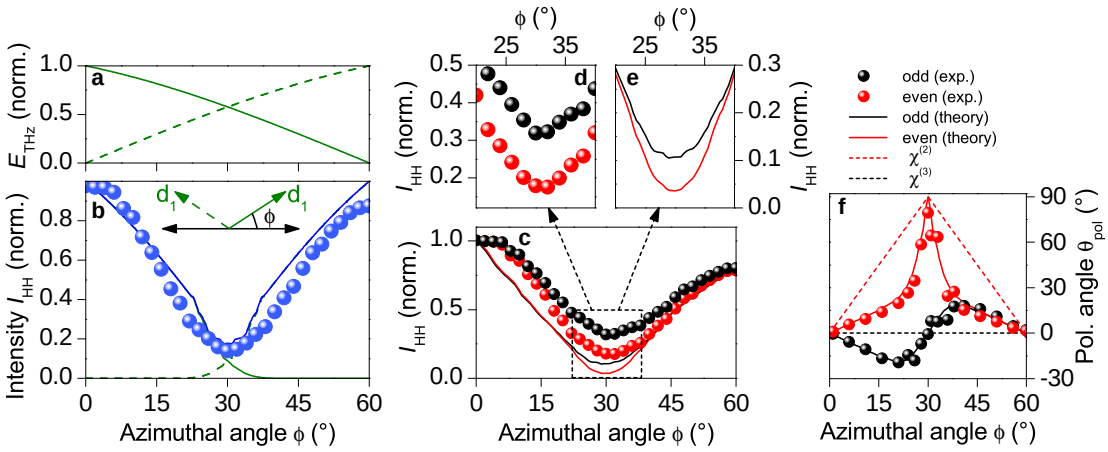

Figure 5.7: Quantitative analysis of HHG along different crystallographic directions: a, Normalized projection of the driving field amplitude E_{THz} on the two neighbouring d_1-directions (see inset to panel b) as a function of the in-plane azimuthal angle ϕ. **b,** The green curves show the expected HH intensity I_{HH} along the two d_1-directions defined in the inset, taking into account the experimentally determined scaling of I_{HH} with the driving field (compare figure 4.11). The blue curve depicts the sum of the green ones, while the experimentally determined HH intensity (exctracted from the data in figure 5.3d) is shown as blue dots. **c-e,** Experimental (dots) and calculated (solid curves) HH intensity of the 10^{th} (red) and 11^{th} (black) order harmonic as a function of the in-plane angle ϕ. The efficiency of the spectrograph for different polarizations has been taken into account. **f,** Experimentally recorded (dots) and calculated (solid curves) polarization of even-order (red) and odd-order (black) harmonics as a function of the azimuthal angle ϕ. The dashed curves show the polarization of the 2^{nd} and 3^{rd} harmonic as expected from the perturbative nonlinear susceptibility tensors $\chi^{(2)}$ and $\chi^{(3)}$, respectively.

time traces (compare, e.g., figure 5.4). The peaks in both pulse trains are thus temporally separated by $T = 30\,\mathrm{fs}$, corresponding to a period of the driving field centred at $\nu_{\mathrm{THz}} = 1/T = 33\,\mathrm{THz}$, while the pulse trains itself are shifted by $T/2 = 15\,\mathrm{fs}$ with respect to each other. Performing a Fourier transformation of these field profiles for different azimuthal angles consequently yields two frequency combs corresponding to one of the neighbouring d_1-directions each. Figure 5.7c compares the calculated spectral peak intensities of HH orders $n = 10$ and 11 with the experimentally measured intensity. Both theoretical and experimental curves show a very similar behaviour: Starting with the maximum efficiency for a driving field polarization along $\phi = 0°$, the intensity decreases by several ten percent to a minimum at $\phi = 30°$ before it increases again to approximately 75% of the initial value at $\phi = 60°$. The comparably lower efficiency along $\phi = 60°$ (compare also spectral mean in panel a) can be attributed to the fact that 3 dominant temporal bursts contribute along $\phi = 0°$, while only two are detected

along $\phi = 60°$. This asymmetry is thus a consequence of the ultrashort pulse width of the driving waveform. For much longer pulses, the number of HH bursts for positive and negative driving fields would be balanced, yielding the same intensity for both directions. The global trend of the HH intensity of even and odd orders as a function of ϕ is well reproduced, while the absolute value of the latter for $\phi = 30°$ is not perfectly displayed by the calculations yet. A possible explanation for this slight discrepancy might be an uncertainty in the experimental field scaling especially for lowest fields, where the strongly reduced HH intensity renders a qualitative extraction challenging[2]. The relative behaviour of even- and odd-order harmonics is well-explained, however: A magnified view of the region around minimum emission is shown in figure 5.7d and e for experiment and theory, respectively. The suppression of even order harmonics is more pronounced compared to the odd orders, which may be understood based on the vectorial decomposition of the high-order harmonic field E_{HH} sketched in figure 5.6f. The perpendicular component finally forming the even orders is weaker (shorter arrows) than the parallel one due to the sharp angle of 30° between the driving field and the d_1-directions.

Finally, the HH polarization may be extracted from the model by calculating the field-projection of emitted harmonics on the directions parallel and perpendicular to the driving field. As depicted in figure 5.7f, the model excellently reproduces the measured polarization behaviour. While both even and odd orders are polarized parallel for $\phi = 0°$ and $\phi = 60°$, the polarization of even orders is gradually rotated out of its initial orientation and encloses an angle of 90° to the odd order polarization at $\phi = 30°$. The polarization of odd orders, in contrast, is only slightly deflected from the parallel orientation for intermediate regions below and above $\phi = 30°$ due to the unbalance of the driving field projections along the two d_1-directions, which is lifted for $\phi = 30°$.

In conclusion, the frequency comb model has been proven to qualitatively explain and even quantitatively reproduce major features of the orientation-dependent emission of high-order harmonics from gallium selenide. Except one a-priori assumption which will be discussed below, all premises underlying the calculations have been extracted or derived from experimental observations. A quite surprising photonic property of the high-order harmonics along certain crystal directions is proven by the model: While the driving field is always linearly polarized, the emitted HH polarization encloses an angle of 30° to the driving field and, more remarkably, switches between two possible polarization directions from burst to burst. Similar to HHG in gases, the exact knowledge of the interlocked polarization-, time- and frequency-domain properties may be crucial for future applications like the isolation and use of single, few- or even sub-femtosecond

[2] Another possible reason might be the ad-hoc assumption that HHG purely occurs along the d_1-directions. See also discussion at the end of section 5.4.2.

pulses. A separation of the two intertwined pulse trains may for example enable novel delay schemes in ultrafast pump-probe experiments. Furthermore, the findings touch upon a property of solid-state high-harmonics never detected or analysed so far, namely their carrier envelope phase. While the phase-stability of emitted harmonics has already been proven, the exact carrier envelope phase has not yet been measured except for the lowest orders (compare section 3.2). The introduced model at least provides intuitive access to the relative phase change between individual HH bursts via measurable quantities, i.e., the polarization and the spectra of high-order harmonics. Apart from the relevance for envisaged applications, the observations additionally allow for interlinking the symmetry of strong-field driven, non-perturbative charge carrier dynamics with the crystal symmetry of gallium selenide, as will be discussed in the following section.

5.4.2 Comparison to the perturbatively assigned symmetry

In perturbative nonlinear optics, it is straightforward to decide which nonlinear optical process may, in principle, occur for a given solid and which may not. The crystal symmetry is reflected in the form of the nonlinear susceptibility tensor. The third-rank tensor describing the second-order susceptibility $\chi^{(2)}$ in gallium selenide, for instance, has only three non-vanishing tensor elements which can be derived from a group-theoretical analysis [Boy03]. As a consequence, the symmetry of the emitted second harmonic, i.e., its polarization for different incidence angles and polarization directions of the fundamental field, can be predicted (see appendix D). For the non-perturbative strong-field processes underlying HHG in solids, however, such symmetry considerations have not been discussed, yet. While it is obvious that the appearance of the second harmonic or even harmonics in general has to imply a broken inversion symmetry, this logic requirement has not been straightforward to connect to the microscopic processes. As shown in section 4.3.3, the quantum interference can only occur for non-inversion symmetric systems which provide at least three electronic states which are mutually dipole-coupled. Here, the observed complex behaviour in dependence on the crystallographic orientation shall in addition be connected to - and substantiated by - the symmetry of the crystal lattice. The concept of a perturbative, macroscopic polarization as defined in equation (3.1) is no longer valid here, but the microscopic interband polarization between different bands and their interplay seem to govern the emission symmetry. In section 4.3, the general field scaling of both *direct* and *indirect* pathways has been derived. A switch-off analysis has shown that the *indirect* paths, whose transition amplitudes generally scale with even orders of the driving field,

$$p_{\mathrm{indirect}} \propto \zeta^{(2)} E_{\mathrm{THz}}^{(2)} + \zeta^{(4)} E_{\mathrm{THz}}^{(4)} + \ldots, \tag{5.1}$$

are crucial for the quantum interference to occur. The coefficients $\zeta^{(n)}$ comprise the dipole matrix elements (compare equations (4.10) and (4.11)). All band indices and assignments have been discarded here for simplicity. While describing the microscopic interband polarization instead of a macroscopic polarization of bound electrons, equation (5.1) has the same general form as the perturbative scaling law for even-order effects. From a mathematical standpoint, the perturbatively assigned symmetry of the even order tensors in the nonlinear susceptibility may thus also hold for $\zeta^{(n)}$. Figure 5.7f compares the expected polarization of the perturbative second and third order harmonics, as calculated from the nonlinear tensors $\chi^{(2)}$ and $\chi^{(3)}$ of the symmetry group D_3^{h} of gallium selenide, with the measured polarization of even and odd order harmonics. As expected, no convincing quantitative match is found, whereas the polarization directions coincide for the high-symmetry orientations $\phi = 0°, 30°, 60°$. For $\phi = 30°$, the second harmonic is polarized perpendicularly with respect to the third order harmonic. Transferred to the microscopic interband polarizations (equation (5.1) and (4.10)), this implies that the *indirect* paths may no longer interfere with the *direct* pathways, i.e., the quantum interference is completely suppressed along these crystallographic directions. Going through this scenario permits a comparison of the expected consequences to the experimental observations: A switch-off of the quantum interference is theoretically expected to suppress the emitted intensity by a factor of approximately 30, as shown in figure 4.9. The three-fold rotational symmetry of GaSe ensures that one of the equivalent d_1-directions may always be addressed, however. As can be seen from figure 5.7a, the driving field projection along one of the d_1-directions always amounts to several ten percent of the full field. Emission along these high-efficiency directions, where the quantum interference enhances the intensity drastically, thus always dominates the recorded HH intensity in the experiment. Consequently, a maximum drop of the emitted HH intensity by less than a factor of ten is observed. This treatment may retrospectively justify the only ad-hoc assumption underlying the frequency comb model described in the previous sections, i.e., that HHG exclusively occurs along the d_1-directions. Applying established symmetry arguments from the perturbative analysis (see above) explains why HHG along these crystallographic directions is particularly efficient and why the other directions, where the quantum interference is switched off, may be neglected in the analysis.

To conclude, perturbatively assigned symmetry properties can not directly be transferred to strong-field driven high-order harmonic generation but basic concepts of the analysis may be adopted in order to understand the orientation-dependence of HHG in solids. In particular, applying straightforward symmetry arguments to different microscopic interband polarization pathways in gallium selenide has provided the missing link between the strong-field quantum interference and the surprising experimental ob-

servations of HHG in different crystallographic directions. The thorough study of the symmetry properties thus corroborates the novel quantum interference and helps drawing a conclusive, sophisticated picture of the HHG mechanism. Furthermore, envisaged applications of solid-state HHG as a spectroscopic tool for condensed matter physics, e.g., for all-optical bandstructure reconstruction [Vam15b, Vam15a], crucially depend upon the understanding of such basic symmetry arguments.

Chapter 6

Towards ultrafast spin injection

The preceding chapters have shown the unique possibilities opened up by field-resolved terahertz pulses with sufficiently strong electric peak fields. In a novel crossover regime between electronics and optics, phase-locked terahertz waveforms may be exploited to excite, accelerate and control charge carriers in solids on ultrashort time scales. The following chapter is intended to add one more degree of freedom which might be addressed by terahertz fields: the electron's spin.

At least since the idea of a spin-based transistor was stated [Dat90], the paradigm to exploit the spin degree of freedom instead of - or in addition to - the electrons charge in electronic devices has become the driving force behind an ever growing number of research projects defining the so-called field of *spintronics* [Aws07]. Major building blocks of anticipated spin-based electronics are the *injection* of spin-polarized carriers into technologically relevant semiconductors, the *manipulation* of the spins and finally the *detection* or read-out of the spin polarization. Different approaches of spin injection from ferromagnetic materials into a semiconductor rely either on optical or on electrical excitation [Tan11]. Examples of optical spin injection include two-colour optical pumping at the band edge of semiconductors which results in pure spin currents [Zha06] or so-called superdiffusive transport between two metals [Bat10, Mel11, Esc13]. Optical excitation always creates excited states far away from thermal equilibrium, however, which renders a direct transfer to technologically relevant devices challenging. While successful schemes of electrical spin injection [Ohn99, Fie99, Olt14] under static or low-frequency electric fields have been well-established, they do not provide experimental access to the temporal dynamics. Even the fundamental process of spin injection, e.g., through tunneling barriers, is not yet fully understood on ultrashort time scales in detail (see below). Although future spintronic devices will have to compete with conventional electronics in terms of achievable clock rates, questions regarding fundamental limits to

the ultimate speed of electrical spin injection have not yet been fully answered.
Here, a completely new approach combining the advantages of both electrical and optical spin injection is introduced. Based on a novel near-field antenna, ultrashort and intense terahertz waveforms shall be exploited as an ultrashort voltage burst which drives spin-polarized currents through a technologically relevant tunnel junction. Combined with optical detection of the spin polarization, the scheme is intended to enable the first study of electrically driven tunnel injection on ultrashort time scales.
After a brief explanation of the fundamental principles exploited to inject and detect spin-polarized carriers in so-called spin LEDs, the novel approach is discussed in detail within the following chapter. The feasibility of the concept is corroborated by numerical simulations, before the first operational prototype of the new spin injection device is introduced. The status report on this ongoing project is closed by presenting first, promising proof-of-principle experiments and a short outlook on the next steps towards ultrafast electrical spin injection.

6.1 Spin light-emitting diode

Electrical spin injection into semiconductors is successfully demonstrated and investigated based on so-called spin light-emitting diodes (spin LEDs) [Ohn99, Fie99, Tan11]. Similar to their conventional counterpart, the spin LEDs usually consist of a semiconductor heterostructure with embedded quantum wells, as schematically illustrated in figure 6.1a. An additional ferromagnetic top electrode enables the injection of spin-polarized electrons through a tunneling barrier (see below) under a static bias voltage V_{DC}. The electrons are subsequently driven to the quantum well where they recombine with holes injected from the p-type back contact (figure 6.1b). The concomitant optical luminescence is detected and allows for analysing the degree of spin polarization of the injected currents, as described in detail below. In the following, the basic working principle of spin LEDs as well as crucial prerequisites for efficient spin injection will be discussed.
For so-called band ferromagnets like iron, the spontaneous magnetization forms due to the spin splitting of the energy dispersion of electrons [Blu01]: As a consequence of the exchange interaction between the spins, the density of states (DOS) at the Fermi energy E_{F} is larger for electrons carrying the majority spin ("↑", see figure 6.1b) compared to the DOS for electrons with minority spin ("↓"). The corresponding spin polarization in a ferromagnet is given by

$$P_{\mathrm{f}} = \frac{n_{\uparrow} - n_{\downarrow}}{n_{\uparrow} + n_{\downarrow}} > 0, \tag{6.1}$$

where $n_{\uparrow}$ ($n_{\downarrow}$) is the density of electrons with majority (minority) spin. As a primary

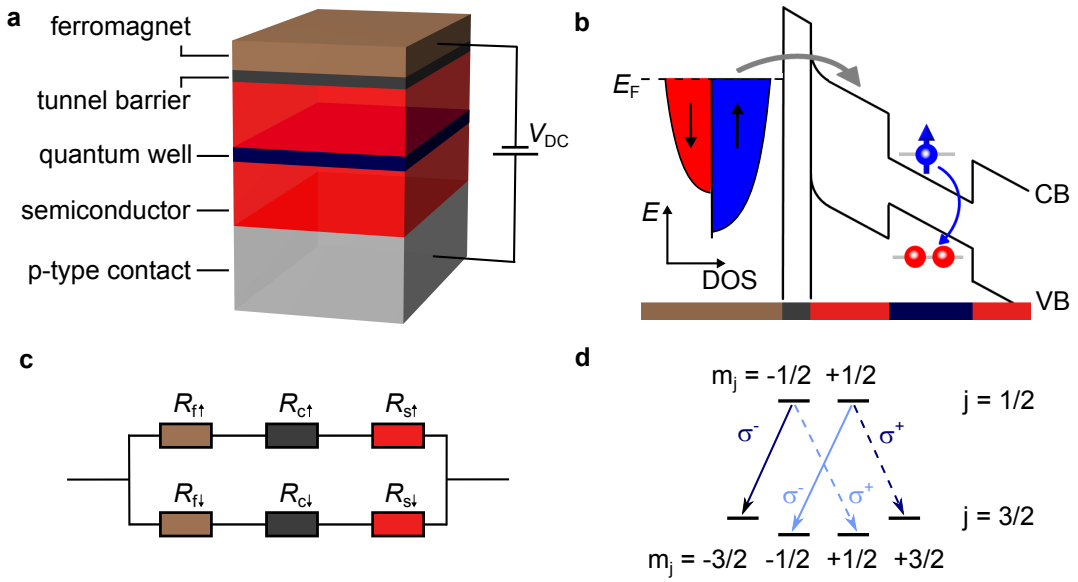

Figure 6.1: Principle of a spin-LED: a, Typical semiconductor heterostructure of a spin LED with a single quantum well. A ferromagnetic metal contact serves as a source of spin-polarized electrons (bias voltage V_{DC}). **b,** Schematic band structure of a typical device as shown in panel a. Electrons from the ferromagnet (spin-split density of states DOS schematically depicted in red (blue) for minority (majority) spins) may tunnel through the barrier (grey arrow) and recombine in the quantum well (blue arrow) with holes injected form the substrate, thereby emitting elliptically polarized light (not shown). E_F: Fermi energy in the metal; CB, VB: conduction and valence band edge, respectively. **c,** Equivalent circuit diagram representing the spin-dependent resistivity of the ferromagnetic top electrode (R_f), the tunneling contact (R_c) and the semiconductor (R_s). **d,** Illustrative energy diagram of conduction band (total angular momentum $j = 1/2$) and valence band ($j = 3/2$) electronic states in a gallium arsenide quantum well. Allowed transitions coupling to cirularly polarized light according to a change of the magnetic quantum number $\Delta m_j = 1$ (σ^+) and $\Delta m_j = -1$ (σ^-) are depicted as dashed and solid lines, respectively.

milestone on the route towards spintronic devices, an ideally effective transfer of this finite spin polarization into the semiconductor is intended. Besides magnetic semiconductors [Ohn99, Fie99, End12], ferromagnetic metals are widely used [Zhu01, Jon07, Kot07] as a spin polarizer due to their relatively high Curie temperatures. An intrinsic obstacle arises from this choice, however, which is connected to the so-called conductivity mismatch [Sch00] between the semiconductor and the metal owing to their drastically differing charge carrier densities. An intuitive derivation of the latter can be achieved by separating the current channels of majority and minority spins and constructing an equivalent circuit diagram for these parallel channels as depicted in figure 6.1c. Each channel is described by the serial resistivity composed of the effective ohmic resistances

per spin diffusion length of the ferromagnet (R_f), the semiconductor (R_s) and the contact between both (R_c). This so-called standard model of electric spin injection yields the total spin injection efficiency

$$P_\mathrm{j} = \frac{R_\mathrm{f} P_{\sigma\mathrm{f}} + R_\mathrm{c} P_{\sigma\mathrm{c}}}{R_\mathrm{f} + R_\mathrm{c} + R_\mathrm{s}} = \langle P_\sigma \rangle_R, \tag{6.2}$$

which is the conductivity spin polarization P_σ averaged over the three constituents (ferromagnet - contact - semiconductor, denoted by respective indices), weighted by their effective resistances [Fab07]. For spin injection from a metal through an ohmic contact, i.e., for $R_\mathrm{c} \ll R_\mathrm{f} \ll R_\mathrm{s}$, it is easy to see that equation 6.2 can be approximated by $P_\mathrm{j} = \frac{R_\mathrm{f}}{R_\mathrm{n}} P_{\sigma\mathrm{f}} \ll P_{\sigma\mathrm{f}}$, which renders the spin injection efficiency negligibly small. The situation changes if a high-resistivity contact $R_\mathrm{c} \gg R_\mathrm{f}, R_\mathrm{s}$ like a tunneling barrier is assumed. This scenario yields a spin injection efficiency $P_\mathrm{j} = P_{\sigma\mathrm{c}}$, i.e., the contact acts as an efficient spin filter. The preceding derivation shows that a tunneling barrier helps to overcome the conductivity mismatch problem [Ras00] and facilitates efficient injection of spin-polarized currents from a ferromagnetic metal into a semiconductor. Beside Schottky contacts, which will be used here, thin oxide layers have successfully been employed as tunneling barriers in spin LEDs [Jon07, Sai10].
Experimental proof of this spin polarization can be given by detecting the polarization state of the emitted photoluminescence light. The dipole selection rules define the possible transitions between the conduction and the valence band, via which spin-polarized electrons may recombine with holes injected from the substrate. The scenario is schematically depicted in figure 6.1d for the case of a quantum well in a III-V semiconductor like gallium arsenide (GaAs). Two classes of transitions from the conduction band ($S_{1/2}$) to the valence band ($P_{3/2}$) are allowed, corresponding to a change in the magnetic quantum number $\Delta m_j = 1$ (σ^+, dashed lines) and $\Delta m_j = -1$ (σ^-, solid lines) and giving rise to the emission of left- or right-handed circularly polarized light, respectively. The probability for transitions into the heavy-hole subband with $m_j = \pm 3/2$ (dark blue arrows) is a factor of three larger than for transitions into the light-hole subband with $m_j = \pm 1/2$ (light blue arrows). If the degeneracy between heavy- and light-hole bands is lifted due to sufficient confinement in the quantum well (as depicted in figure 6.1d), the corresponding emission channels may be spectrally separated. The degree of circular polarization P_circ of the emitted photoluminescence of a selected transition then directly yields the spin-polarization in the conduction band via $P_\mathrm{S} = P_\mathrm{circ}$.
Based on the spin LED approach [Ohn99, Fie99], spin injection with polarizations of several ten percents even at room temperature [Zhu01] and into important silicon-based devices [Jon07, van12] have been achieved. Electrical spin injection into technologically relevant semiconductors has only been observed in a time-integrated fashion, so far.

Future spintronic devices will have to compete with conventional electronics also in terms of speed and achievable clock rates, however. Resolving the underlying dynamics on ultrashort time scales could help answering a number of open questions, which are subject of recent debates, and would thus be highly beneficial for envisaged applications. These discussions include, e.g., the role of interface or surface states at the barrier [Cha07, Der07], which might trap carriers, influence their spin polarization or cause a delay of the injection process. The interplay of carriers, spins and phonons during the tunneling process has also remained untapped, yet. A time-resolved observation of spin propagation could also clarify spin coherence times and the influence of different scattering channels, for instance.

6.2 Terahertz near-field antenna for ultrafast tunnel injection

A novel approach combining the advantages of electrical spin injection and optical detection on ultrashort time scales is introduced here. Instead of a static bias voltage, an ultrashort voltage burst delivered by a single-cycle terahertz transient shall be employed to drive spin-polarized currents through a tunnel junction into a spin LED. This idea affords two main achievements. First, the terahertz electric field has to point along the growth direction of epitaxially grown semiconductor heterostructures, which is not straightforward to implement owing to the transversal nature of electromagnetic radiation in the far-field. Second, the bias has to be strong enough to drive significant tunnel currents within only one half-cycle of the driving waveform. Both requirements may be fulfilled with the help of a tailor-cut near-field antenna which hosts the semiconductor heterostructure, as explained in the following.

Inspired by planar, so-called bowtie-antennas [Cro03, Sch05], a three-dimensional near-field antenna concept has been developed here, which is schematically laid out in figure 6.2a and b: Two triangular-shaped antenna sheets are vertically and horizontally offset to form a vertical gap between their vertices. If both antenna halves are sufficiently conductive, an incident terahertz waveform (black transient in figure 6.2a), polarized along the long axis of the antenna (length l), will induce a transient current and a concomitant charge accumulation at the facing tips. Similar to a capacitor, a strong electric near-field builds up between the antenna plates in the overlap region, which is oriented longitudinally with respect to the propagation direction of the incident terahertz pulses. In order to use this electric near-field as an ultrashort bias for spin injection, the diode structure may be directly embedded within the gap region (compare cut-out in panel 6.2b). To this end, the lower antenna half may consist of highly p-doped gallium arsenide (p-GaAs) directly grown on top of an intrinsic GaAs substrate. Above the quantum well and a suitable tunnel junction, a spin-polarizing

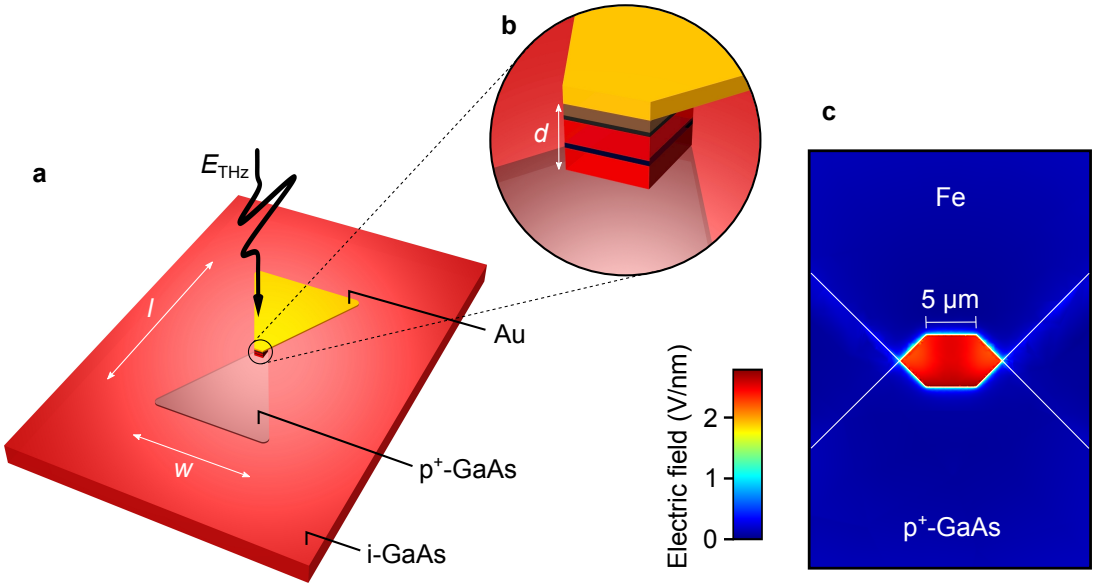

Figure 6.2: Terahertz near-field antenna for longitudinal tunnel injection: a,b, Illustration of the novel antenna concept. Two vertically and horizontally offset antenna triangles consisting of p-doped gallium arsenide and gold (a), respectively, enclose the spin LED in a small overlap region (b, compare figure 6.1a). An incident transient terahertz field (black waveform in panel a) is funnelled into the gap of the antenna and strongly enhanced locally, yielding an ultrashort, longitudinal bias voltage. **c,** Frequency domain simulation of an antenna as depicted in panel a (top antenna wing consists of iron instead of gold) for geometrical dimensions $l = 70\,\mu m$, $w = 75\,\mu m$ and $d = 200\,nm$. For resonant excitation at a frequency of 1 THz, the longitudinal electric field in the gap region is expected to reach values on the order of $1\,V/nm$ (see key).

electrode can be connected to the upper antenna half. This way, the incident terahertz radiation is anticipated to be efficiently funnelled into the gap region, where it can be employed as a localized, strongly enhanced and longitudinally oriented voltage burst to inject spin-polarized carriers into the spin LED.

Resulting photoluminescence light from the quantum well can be collected after transmission through the GaAs substrate and analysed to determine the spin polarization of the injected currents as explained above. In a second step, the population in the quantum well may be transiently probed by near-infrared pulses resonant to the quantum well transition. Pauli-blocking of the transition is expected to allow for examining the occupation of the electronic states. In addition, the spin polarization of the carriers in the quantum well may be probed by measuring the absorption for both left- and right-hand circularly polarized pulses. By delaying the optical probe with respect to the THz waveforms, the first study of electrically driven spin tunnel injection on ultrashort time scales could become possible.

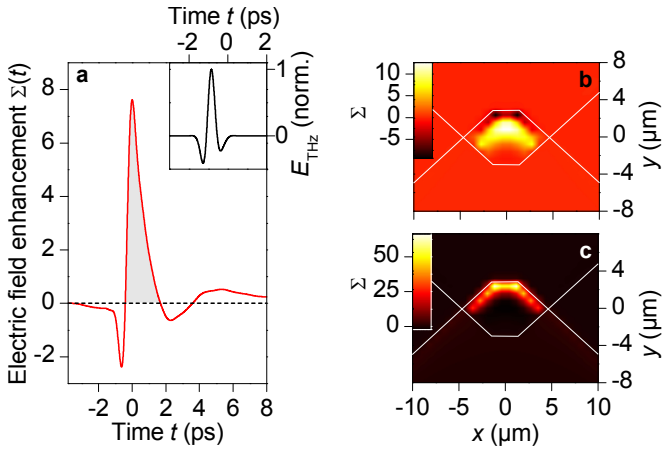

Figure 6.3: FDTD simulation: a, Computed field enhancement at the centre of the gap for an antenna as sketched in figure 6.2 with geometrical dimensions $l = w = 140\,\mu\text{m}$ and $d = 100\,\mu\text{m}$. The incoming field profile (see inset) resembles the experimentally available waveform. The doping level of the lower antenna part has been set to $p = 8 \cdot 10^{18}\,\text{cm}^{-3}$. **b,c,** 2D map of the electric near-field enhancement along a vertically centred plane in the antenna gap at times $t = 0\,\text{ps}$ (b) and $t = -0.5\,\text{ps}$ (c).

Frequency- and time-domain simulations of the near-field enhancement

As a first check of the feasibility of this novel approach, finite-difference frequency-domain (FDFD) simulations of the near-field enhancement have been performed. Using the commercial software package *COMSOL*, an antenna geometry as shown in figure 6.2a has been implemented and its response to an incoming terahertz field has been systematically tested. In the model, the upper and lower antenna halves consist of iron and p-GaAs with a doping level of $p = 1 \times 10^{19}\,\text{cm}^{-3}$, respectively[1]. The heterostructure in-between the antenna tips has been approximated by a block of gallium arsenide with a dielectric constant of $\varepsilon_{\text{GaAs}} = 12.9$. The exact geometrical parameters used in the calculations are given in the caption of figure 6.2. When tuned to resonance with an incoming plane wave centred at a frequency of 1 THz, the simulations indeed predict a strongly enhanced, longitudinally oriented electric near field in the centre of the vertical gap of the antenna (see figure 6.2c). A field enhancement factor of approximately 20 promises absolute electric near field amplitudes of 2 V/nm for realistic incoming peak fields of 1 MV/cm (compare figure 2.4). Such strong fields have already been shown to cause interband tunneling in undoped semiconductors and strong carrier multiplication by impact ionization [Lan14]. The concept is thus believed to readily support fields strong enough to drive tunnel currents through technologically relevant junctions and

[1] The corresponding dielectric functions of p-doped GaAs and iron have been extracted from a Drude-model with parameters from references [Hug00] and [Ord85], respectively.

may enable the study of yet unseen strong-field effects during the tunneling process.
The frequency-domain simulations described so-far corroborate the anticipated operating principle of the developed near-field antenna. To take into account the broadband nature of the ultrashort terahertz transients (compare figure 2.4), the full field profile has to be implemented in the calculations, however. To this end, finite-difference time-domain (FDTD) simulations have additionally been performed [Raa15] based on the commercial Maxwell-solver *Lumerical*. While a detailed description of the model is given in reference [Raa15], only the most relevant results shall be discussed here. The model itself has been set up similarly to the frequency domain simulations described above (see caption of figure 6.3 for geometrical and material parameters), but a field profile resembling the experimental waveforms has been implemented (see inset to figure 6.3a). Adjusting the size of the antenna to a resonance frequency lying in the centre of the terahertz amplitude spectrum in principle yields maximum field enhancement. This resonance manifests itself in pronounced, quasi-monochromatic trailing oscillations in the near-field trace, however, which might be undesired for a unidirectional, well-defined voltage burst. An increase of the antenna size is generally found to result in a growing near-field enhancement. On the other hand, the concomitantly decreasing resonance frequency elongates the dominant half-cycle of the field enhancement, which might blur the well-defined injection time. For a suitable trade-off between these two trends, an antenna length of approximately $l = 140\,\mu\text{m}$ (compare figure 6.2a) has been chosen. The corresponding simulated near-field enhancement in the centre (both laterally and vertically) of the overlap region as a function of time t is depicted in figure 6.3a. The strongly asymmetric near-field profile exhibits one dominant field crest (shaded area), which exceeds the extrema of opposite polarity by more than a factor of 3. In combination with the strongly nonlinear voltage-current characteristics of a tunnel junction and precise tuning of the incoming field strength, this asymmetric trace might help to inject tunnel currents in a well-defined way only during one half-cycle of the driving field, i.e., within a timespan on the order of less than 1 ps.
Two-dimensional snapshots of the computed near-field enhancement Σ along the centre plain in-between the antenna pads are shown for times $t = 0\,\text{ps}$ and $t = -0.5\,\text{ps}$ in figures 6.3b and c, respectively. A comparison of both panels shows that even significantly higher field amplitudes may be generated at the edge of the upper antenna half (structure boundaries are highlighted by white lines) and that the field enhancement is not yet perfectly homogeneous in the gap region. Future customization of the exact antenna shape may help to reduce such inhomogeneities if they were found to be detrimental for the envisaged experiments.

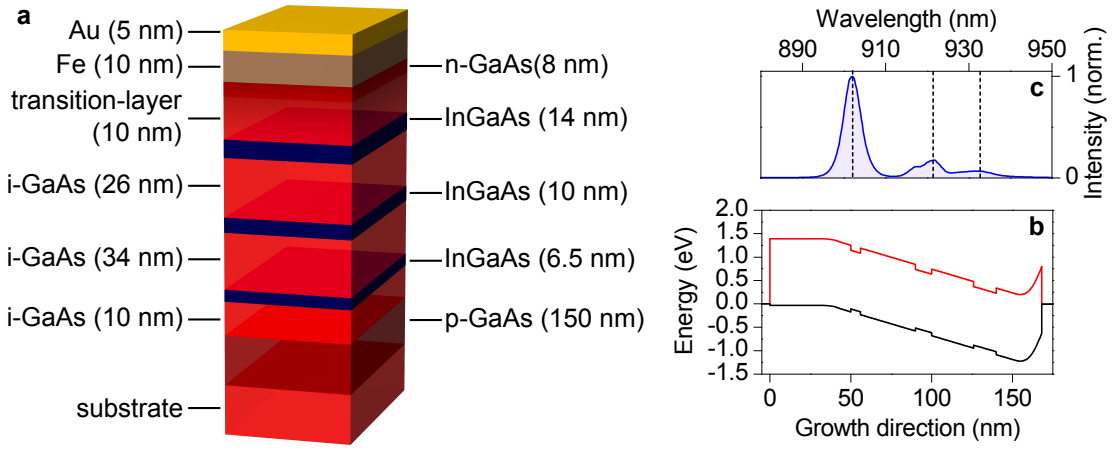

Figure 6.4: Semiconductor heterostructure: a, Schematic illustration of the epitaxially grown spin LED structure. The thickness of all layers is given in brackets. **b,** Computed conduction and heavy-hole valence band of the structure shown in panel a in the absence of an external field. **c,** Photoluminescence intensity spectrum from a fabricated antenna structure (see section 6.4) at a sample temperature of 4.2 K and under static bias voltage $V_{\mathrm{DC}} = 21\,\mathrm{V}$.

6.3 Fabrication of an operative device

So far, the feasibility and the function principle of the novel longitudinal near-field antenna have been discussed based on the conceptual scheme as well as computational simulations. The following section will briefly summarize the fabrication of the first prototypical, operative device. Again, a more detailed description can be found in reference [Raa15], while only some of the most important results are summarized here.

As the most common and compatible semiconductor material for electronic applications, gallium arsenide has been chosen as a substrate for the spin LED here. The heterostructure, which has been grown in the molecular beam epitaxy by the group of Dominique Bougeard in Regensburg, is schematically illustrated in figure 6.4a. As a conductive layer finally forming the lower antenna wing, a 150-µm-thick p-doped GaAs region has been grown (doping level $p = 6 \times 10^{18}\,\mathrm{cm}^{-3}$). On top of this conductive sheet, three indium gallium arsenide (InGaAs) quantum wells (QW) have been added, which are separated by intrinsic GaAs spacers and feature a thickness of 6.5 nm, 10 nm and 14 nm, respectively. The indium concentration in the QW amounts to 15% ($\mathrm{In}_{0.15}\mathrm{Ga}_{0.85}\mathrm{As}$), which is the maximum reachable value without risking lattice defects due to the mismatch between the lattice constants of GaAs and InGaAs. Following an additional intrinsic GaAs layer above the uppermost quantum well, a layer of gradually increasing negative doping $n = 0 \rightarrow n = 6 \times 10^{18}\,\mathrm{cm}^{-3}$ has been added which guarantees a smooth transition of

the electronic bands [Kot07, End12] to a highly n-doped region ($n = 6 \times 10^{18}\,\mathrm{cm}^{-3}$). A Schottky-type contact forms between this highly doped region and a thin iron electrode on top of the structure. To avoid oxidation, the iron contact has been covered by a 5-nm-thin gold layer.
The bandstructure of the epitaxially grown stack has been computed using the commercial software *nextnano* and is laid out in figure 6.4b. According to this simulation, the energy gaps in the three quantum wells are estimated to correspond to a photoluminescence wavelength of 892 nm, 905 nm and 918 nm, respectively, at a temperature of 4.5 K.

After growing the diode heterostructure, the novel near-field antennas have been fabricated using electron beam lithography and a series of elaborate etching and lift-off techniques [Raa15], which are only described in a condensed fashion here. First, the lower antenna half has to be exposed. To this end, a negative electron-sensitive resist is used to form a suitable mask for three subsequent etching processes which remove the gold capping, the iron electrode and the heterostructure including the p-doped GaAs layer, respectively. After this first step, the lower antenna half is still covered by the full spin LED stack, which is removed in a second, similar sequence of etching processes up to a small pillar at the apex of the triangular-shaped antenna wing. This intermediate status is captured by the electron microscope picture shown in figure 6.5a. On top of the lower antenna half consisting of p-GaAs, the hexagonal pillar consisting of the GaAs heterostructure, the iron electrode and the gold capping layer can be seen at the eventual overlap region of the antenna. Before the upper antenna half may be fabricated, the exposed etches of the diode have to be electrically insulated and the step in height between the substrate and the top electrode has to be filled up at least partially. For this purpose, the whole structure is covered with polymethylmethacrylat (PMMA). Under a sufficiently high electron dose in the electron beam lithography, the molecular chains in PMMA are connected to extended polymer chains. This so-called cross-linked PMMA [Zai96] is highly resistive against common solvents and electrically insulating. Leaving a small region in the middle of the top electrode open, the rest of the antenna is completely cladded by cross-linked PMMA. After that, the upper antenna half is defined by electron beam lithography based on a positive resist and finally produced by gold evaporation. An electron microscope image of the central part of the completed antenna structure is shown in figure 6.5b. The hexagonally shaped spin LED can be identified under the cross-linked PMMA (dark regions), smoothly covered by the 200-nm-thick upper antenna half (bright region). The circular dent marks the PMMA-free contact region, where the gold antenna is attached to the upper electrode of the spin LED.

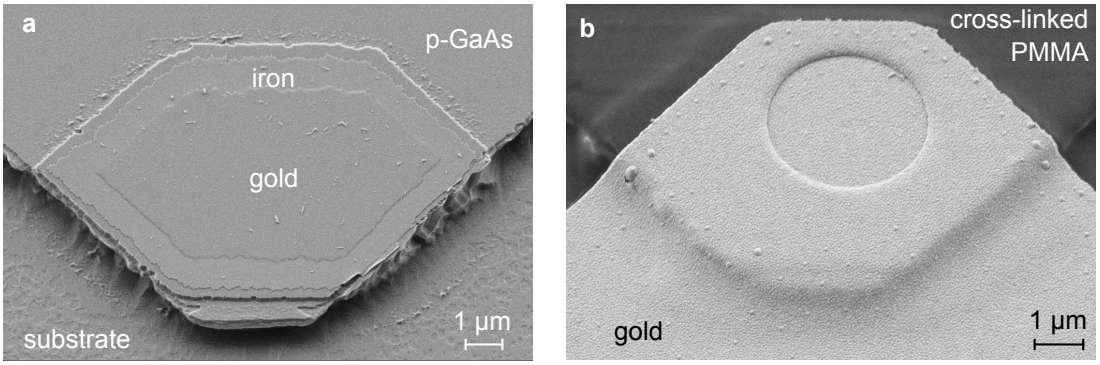

Figure 6.5: First prototype of the novel near-field antenna: Electron microscope pictures of the lower antenna half with the spin LED (a) and of the completed antenna structure (b).

In order to make sure that the numerous processing steps have been successful and the diode structure has not been damaged, some of the fabricated antennas have been connected to contact patches both from the upper (gold) and the lower (p-GaAs) part [Raa15]. This way, an external static voltage may be applied and the photoluminescence can be collected[2]. For a temperature of 4.2 K, a typical PL intensity spectrum is shown in figure 6.4c for an applied voltage of $V_{\mathrm{DC}} = 21\,\mathrm{V}$. Note that the applied bias does not necessarily define the voltage drop over the single diodes, since only two contacts have been used to measure both the voltage and the current. All three QW are clearly discernible in the spectrum. The centre wavelengths of the PL peaks (highlighted by the black dashed lines) are slightly red-shifted with respect to the expected values, which is likely connected to the quantum-confined Stark-effect due to the band bending in the diode structure. At room temperature, signatures of the individual quantum wells are still discernible, the broadening of the peaks strongly smears out their visibility, however (see below).

6.4 Terahertz-induced tunnel injection - status quo and outlook

To test the prototypical near-field device for ultrafast tunnel injection introduced during the last sections, the low-frequency terahertz source shown in figure 2.3a has been extended by a suitable micro-luminescence setup. As schematically depicted in figure 6.6a, the antenna sample is placed in the nearly-diffraction limited focal spot of the strong terahertz pulses (compare figure 2.5c, peak field strength $E_{\mathrm{THz}} \approx 1.2\,\mathrm{MV/cm}$). A mi-

[2]For this purpose, the micro-PL setup of the group of Dominique Bougeard has been used.

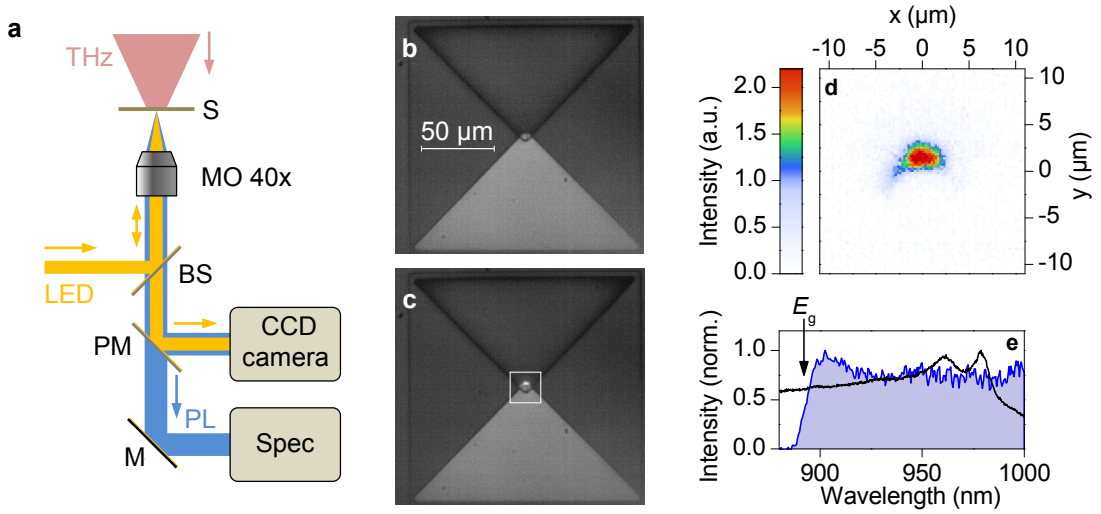

Figure 6.6: Micro-luminescence setup and first terahertz-induced luminescence: a, Schematic illustration of the micro-photoluminescence setup. S: antenna sample, MO: microscope objective (magnification factor: 40), LED: light-emitting diode, BS: beam splitter, PM: pick-off mirror, M: mirror, PL: photoluminescence, Spec: grating spectrograph. **b,c,** Photograph of one of the near-field antennas under illumination via the LED with (c) and without (b) incident terahertz waveforms. **d,** False-colour plot of the luminescence intensity as extracted by subtraction of the picture shown in panel b from the one shown in panel c. The cut-out region is highlighted by the white rectangle in panel c. **e,** Intensity spectrum of the signal shown in panel d (blue shaded curve) and of the collected PL under static biasing (black). The black arrow marks the fundamental band gap energy E_g of intrinsic gallium arsenide at room temperature. The spectral responses of the grating and the detector have been accounted for in the terahertz-induced PL recording.

croscope objective (magnification factor 40) is used to collect the terahertz-induced photoluminescence (PL), which is either spectrally or spatially resolved via a grating spectrograph or a CCD camera, respectively. An additional illumination path (yellow beam) has been implemented to be able to orient the sample properly and to assign the detected PL to a certain spot at the sample. Since the GaAs substrate employed for the first samples has not yet been polished on the rear facet, the sample had to be put into the beam path with the spin LEDs[3] on the side of the microscope. Figure 6.6b presents an optical microscope image captured with the CCD camera, which shows one of the antennas on the sample. The darker side depicts the lower antenna half consisting of p-GaAs, while the reflection at the gold surface leads to the relative brightness of the upper antenna wing.

[3]Several identical antenna structures have been fabricated on one substrate in parallel.

When the terahertz pulses are focused onto the sample, a bright spot appears in the vicinity of the gold antenna apex (figure 6.6c). The numerical difference between the two pictures (with and without incident terahertz waveforms) isolates the luminescence signal shown in a magnified view in picture 6.6d. Switching to the spectrograph allows for further analysing the emitted light. The corresponding intensity spectrum in figure 6.6e (blue shaded) shows a distinct onset, which coincides with the fundamental band gap energy E_g of intrinsic GaAs at room temperature. A plateau-like region up to a wavelength of approximately 1000 nm close to the detection limit of the employed silicon CCD is observed. While the exact shape and the origin of this signal might not yet be perfectly understood, it clearly represents the first terahertz-induced photoluminescence from the novel near-field antenna. The broadband nature of the spectrum including wavelengths well above the fundamental band gap of intrinsic GaAs suggests that the radiation indeed stems from the quantum wells inside the spin diode. A comparison with a typical PL spectrum from the quantum wells in-between the antenna wings gained under static bias (black curve in figure 6.6e, see preceding section for the experiment) further corroborates this hypothesis. The distinct onset of the signal at the intrinsic band gap E_g excludes other sources like, e.g., luminescence from ionized air, which has been observed close to terahertz near-field hot spots at antenna structures [Iwa15]. The shape of the spectrum rather indicates that the observed signal has been transmitted through intrinsic GaAs before detection. Since the upper antenna part hinders PL photons from the quantum wells to directly emerge along the growth direction, the observed signal might only represent a small portion of the actually induced PL light which is reflected and strayed in-between the antenna halves. The observed spatial form of the luminescence spot presented in figure 6.6d strongly supports such a scenario.

In conclusion, the feasibility of the fundamentally new concept for ultrafast tunnel injection has been proven by the DC bias experiments as well as first collected terahertz-induced luminescence spectra. Given the complexity of the fabrication process, the operability of the structures may be seen as the most important milestone on the route towards the first time-resolved study of spin-polarized tunneling into relevant semiconductor heterostructures. The promising findings also set the agenda for future experimental improvements: For straightforward optical detection of the emitted PL through the rear facet of the substrate, the next generation of samples will be fabricated on GaAs wavers polished on both sides. Furthermore, a novel optical cryostat in combination with a superconducting magnet is currently being installed in the high-field terahertz laboratory. At cryogenic temperatures, the assignment of spectral features to the quantum wells will be much more reliable. In addition, the magnet will permit magnetic field

biasing of the spin-polarizing electrode along the growth direction (so-called Faraday geometry). With these upgrades, the detection of terahertz-driven, spin-polarized tunnel currents comes into practical reach, which directly sets the stage for time-resolved pump-probe measurements. Apart from spin injection experiments, the ability to form a strong longitudinal electric bias on ultrashort time scales may in general open up new perspectives for coherent control schemes of charge transport along the growth direction of epitaxial semiconductor heterostructures [Vän15].

Chapter 7

Summary and outlook

In this thesis, non-perturbative charge carrier dynamics in crystalline solids have been explored in a novel coherent high-field regime bridging nonlinear optics and sub-cycle lightwave electronics. Ultrashort, atomically strong terahertz waveforms have been exploited to drive coherent interband excitation and dynamical Bloch oscillations in bulk gallium selenide [Sch14b]. The resulting phase-locked and octave-spanning high-order harmonic emission has been temporally resolved for the first time [Hoh15a], shedding light on a strong-field quantum interference of different interband polarization paths.

The experiments have been made possible by a new high-field source, which delivers phase-stable, ultrashort waveforms with extremely high field strengths in a broad spectral regime of far- to mid-infrared wavelengths. In a first setup, single-cycle transients at frequencies around 1 THz with peak electric and magnetic fields on the order of 1 MV/cm and 0.3 T, respectively, provide a particularly well-defined, ultrashort and contactless bias field for the study of non-perturbative charge carrier dynamics and nonlinear spin control in solids [Lan14, Maa16, Bai16]. Based on these waveforms, a fundamentally new approach for ultrafast electric spin injection via tailored near-fields in a three-dimensional optical antenna has been introduced. First operational prototypes have been demonstrated and characterized, which set the stage for time-resolved studies of spin-polarized tunnel injection into technologically relevant semiconductor heterostructures.
A second beamline facilitates lightwave electronics at multi-THz clock rates with sub-cycle time resolution by combining phase-locked waveforms featuring peak electric fields on the order of 100 MV/cm with octave-spanning, 8-fs-long optical pulses from a solid-state filamentation source. The strong multi-THz transients have been employed to drive coherent interband excitation across the fundamental band gap in undoped gallium selenide, which is more than 14 times larger than the terahertz photon energy. Simulta-

neously, the carriers are accelerated within their respective energy bands through the whole Brillouin zone, giving rise to dynamical Bloch oscillations. This highly anharmonic quantum motion results in the emission of a record-bandwidth, phase-stable high-order harmonic spectrum which covers more than 12 optical octaves [Sch14b].
Yet more importantly, the terahertz-driven high-harmonic emission has been temporally resolved in intensity and relative phase and in precise correlation with the driving waveform [Hoh15a]. A novel cross-correlation scheme with synchronized electro-optic sampling clocks the underlying dynamics with an accuracy of only 1.5 fs, a fraction of 1/20 of a single driving field cycle. The high-order harmonics are emitted as a unipolar pulse train of ultrashort and nearly unchirped bursts, which emerge exactly at the driving field crests. As explained by a quantum-mechanical many-body theory, these findings reveal a novel strong-field quantum interference between several, off-resonantly driven interband polarization pathways, including even electronic transitions well below the Fermi level.
A sophisticated examination of non-perturbative high-order harmonic generation along different crystallographic directions in gallium selenide has brought a surprising polarization behaviour of emitted harmonics to light. A phenomenological model based on the properties of frequency combs reconciles the spectrally, temporally and polarization-resolved findings and enables a comparison to straightforward symmetry arguments known from perturbative nonlinear optics.

The thorough investigation of high-order harmonic emission from gallium selenide marks an important milestone on the route towards envisaged photonic applications: Intrinsically short pulse durations of the emitted harmonic bursts spark hope for future few- or even sub-femtosecond solid-state laser sources with unique capabilities for sub-cycle pulse shaping. Boosting the peak driving field strength with the help of custom-tailored nano-antennas may in the future even allow for generating high-order harmonics in solids at megahertz repetition rates, which would bring the use of octave-spanning harmonic spectra for frequency combs and metrology into practical reach.
On a more fundamental level, the findings reported here help to draw a complete quantum picture of the microscopic dynamics underlying solid-state high-order harmonic generation. Intended applications in fundamental solid-state research like all-optical band structure reconstruction will crucially depend on the understanding of the coupled interband- and intraband dynamics, including strong-field interference effects as uncovered here. In the future, local field enhancement at the tip of state-of-the-art near-field microscopes [Eis14] could even bring the sub-cycle observation of highly nonlinear charge carrier dynamics to the nanoscale.

In general, lightwave-driven electronics in solids at terahertz clock rates may become a key to a variety of yet unforeseen quantum phenomena during high-field charge transport on sub-cycle time scales. A fascinating example for the perspectives opened up by the experimental apparatus introduced in this thesis is the time-resolved study of lightwave-driven electron-hole recollisions, which is currently under way and will be described in detail elsewhere [Lan16]. While the strong-field excitation underlying high-order harmonic generation, as shown in this work, creates a population of quasi-free Bloch electrons throughout the whole Brillouin zone, optical excitation may create excitons - Coulomb-bound electron-hole pairs with well-defined momentum, which feature hydrogen-like internal electronic states. Similarly to the three-step model of high-order harmonic generation in atoms [Cor93, Lew94], a strong lightwave may ionize these excitons, subsequently accelerate their consituents and finally recollide them. Upon recollision and annihilation of the electron-hole pair, the excess kinetic energy gained during the acceleration phase may be emitted as high-order spectral sidebands of the interband resonance [Liu07, Zak12]. Here, optical pulses create excitonic electron-hole pairs in an only 60-nm-thick sheet of tungsten diselenide, while a co-propagating few-cycle multi-THz waveform is simultaneously focused onto the sample (see figure 7.1a). For narrowband, resonant exciton preparation, the dynamics indeed result in the emission of ultrabroadband high-order sidebands up to the ultraviolet spectral range (figure 7.1b). Going one step further, the excitons are prepared on a sub-cycle time scale, i.e., at a distinct and well-defined phase of the low-frequency driving field (black curve in figure 7.1c). The emitted high-order sideband intensity I_{HSG} (blue shaded curve in panel c) may now be recorded as a function of the exciton preparation time. Remarkably, a pronounced sub-cycle modulation of I_{HSG} becomes apparent, attesting to the presence of efficient and less efficient injection times with respect to the phase of the driving field. In sharp contrast to the temporal features of high-order harmonic emission studied in this work, a global delay δ_{g} between the envelopes of the driving waveform and I_{HSG} as well as a distinct sub-cycle delay δ_{SC} is clearly discernible. These findings rule out any instantaneous nonlinearities like the dynamic Franz-Keldysh effect and directly prove the ballistic nature of the underlying dynamics.

These experiments will not only expand the horizon of lightwave electronics towards exploiting excitonic degrees of freedom in state-of-the-art material systems. They also open up a fundamentally new approach to study the internal degrees of freedom as well as the dynamics of complex many-body states in condensed matter: lightwave-driven quasi-particle collisions.

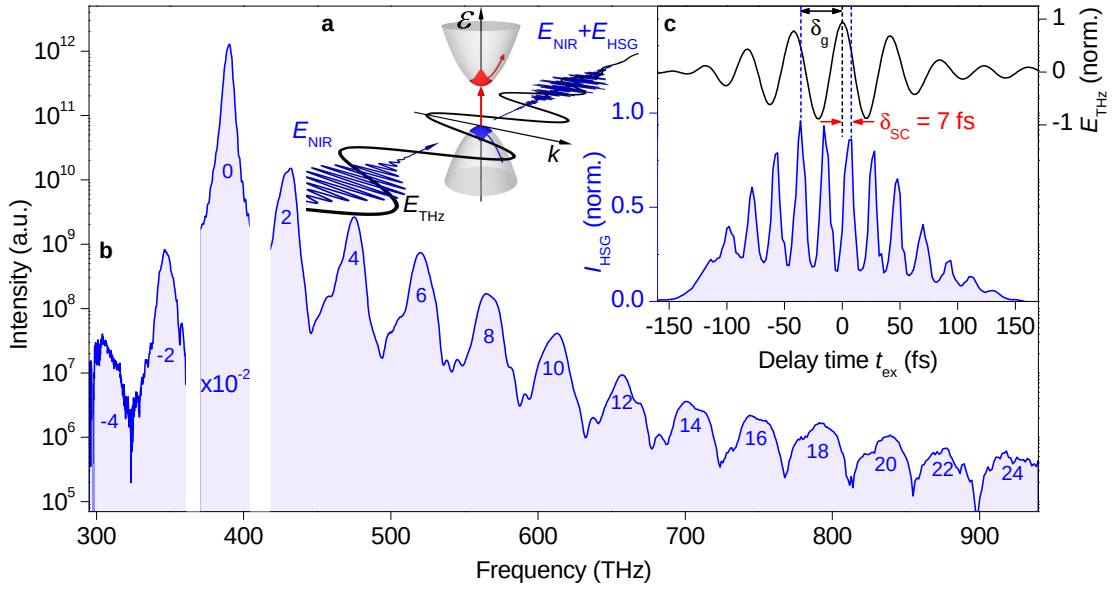

Figure 7.1: Time-resolved high-order sideband generation in tungsten diselenide: a, Schematic illustration of the experimental setting. A near-infrared excitation pulse (E_{NIR}, incoming blue waveform) resonantly prepares an excitonic polarization (red and blue wavepackets in the parabolic dispersion) in tungsten diselenide (WSe_2), which is simultaneously modulated by a co-propagating, strong multi-THz field (E_{THz}, black waveform), giving rise to the emission of spectral sidebands of the near-infrared pulse (outgoing blue waveform). **b,** Ultrabroad high-order sideband intensity spectrum emitted from a 60-nm-thin sheet of WSe_2 for narrowband resonant exciton preparation at a frequency of 392 THz and a driving field featuring a centre frequency of $\nu_{\mathrm{THz}} = 22$ THz and peak field strengths of 11 MV/cm. Numerals denote the sideband order n. The near-infrared excitation spectrum ('0') has been scaled by a factor of 10^{-2} relative to the sideband intensity. **c,** High-order sideband intensity I_{HSG} (blue shaded) and field profile of the driving waveform (black) as a function of the delay time t_{ex} between a 10-fs excitation pulse and the terahertz peak field. A distinct delay $\delta_{\mathrm{g}} \approx 1/\nu_{\mathrm{THz}}$ between the global maximum of I_{HSG} and the highest driving field crest as well as a sub-cycle delay δ_{SC} between the sideband peaks and the field crests becomes apparent.

Appendix A

Influence of third-order dispersion on ultrashort white-light pulses

Resolving sub-cycle dynamics requires probe pulses with durations significantly shorter than one half-cycle of the driving (terahertz) waveform. As described in section 2.6, such short pulses can only be realized via sophisticated dispersion control. In general, the chirp, i.e., a temporally varying frequency, of a broadband light pulse may be described [Die06] based on its spectral phase $\varphi(\omega)$. The electric field of the pulse is then given by $E(\omega) = \sqrt{I(\omega)} \cdot \mathrm{e}^{-i\varphi(\omega)}$ in the frequency domain, where ω is the angular frequency and $I(\omega)$ represents the spectral intensity. The spectral phase can be expanded in a Taylor series around the centre frequency ω_0 of the laser pulse:

$$\varphi(\omega-\omega_0) \approx \varphi(\omega_0)+\frac{\partial\varphi}{\partial\omega}|_{\omega_0}\cdot(\omega-\omega_0)+\frac{1}{2}\frac{\partial^2\varphi}{\partial\omega^2}|_{\omega_0}\cdot(\omega-\omega_0)^2+\frac{1}{6}\frac{\partial^3\varphi}{\partial\omega^3}|_{\omega_0}\cdot(\omega-\omega_0)^3+\dots \quad \text{(A.1)}$$

While the first and the second term only add a constant phase and a temporal delay to the optical pulse, respectively, they do not influence its shape. The third term describes a quadratic contribution to the spectral phase, which adds a frequency-dependent delay. The so-called group velocity dispersion (GVD) is connected to the group velocity $v_\mathrm{g} = \frac{\partial\omega}{\partial k}$ via

$$\mathrm{GVD} = \frac{\partial^2\varphi}{\partial\omega^2} = \frac{\partial}{\partial\omega}\left(\frac{1}{v_\mathrm{g}}\right), \quad \text{(A.2)}$$

where k is the wave vector. This contribution to the chirp of ultrashort pulses is commonly compensated by a prism compressor as explained in section 2.2.1. The third order dispersion (TOD) given by the fourth term in equation (A.1), which is proportional to

$$\mathrm{TOD} = \frac{\partial^3\varphi}{\partial\omega^3} = \frac{\partial^2}{\partial\omega^2}\left(\frac{1}{v_\mathrm{g}}\right), \quad \text{(A.3)}$$

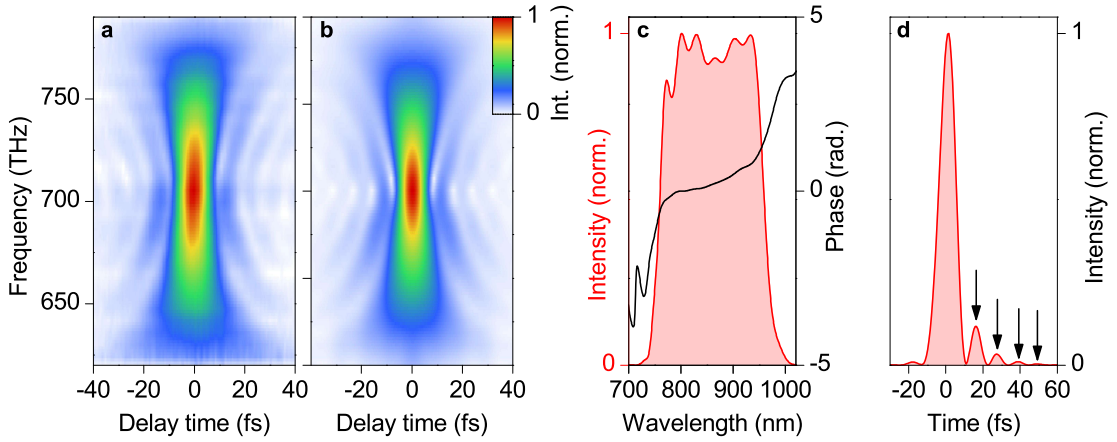

Figure A.1: Influence of third order dispersion on the temporal shape of an ultrashort pulse: a,b, Measured (a) and reconstructed (b) second harmonic FROG spectrogram showing the second harmonic intensity as a function of the frequency and the relative delay time between the two replica of the pulses. **c,** Reconstructed spectral intensity (red) and phase (black) of the spectrally tailored white light pulse. **d,** Reconstructed temporal envelope of the intensity showing pronounced post-pulses (highlighted by black arrows) due to third-order dispersion.

can in general not be compensated at the same time without further degrees of freedom. Adding a cubic dependency on the frequency to the spectral phase, TOD leads to pre- or post-pulses, depending on its sign.

Figure A.1 shows a second-harmonic FROG recording of spectrally tailored white-light pulses after compression of the GVD with the prism compressor sketched in figure 2.6a without additional compensation of third order dispersion. The good match between the measured (panel a) and reconstructed (panel b) intensity spectrograms permits a faithful extraction of the spectral intensity $I(\omega)$ and phase $\varphi(\omega)$ as depicted in figure A.1c. As already obvious from the shape of the spectral phase (black curve), a cubic dependence on the frequency by TOD dominates the phase evolution. This fact is reflected in pronounced satellite pulses after the short main pulse[1] (figure A.1d), which are also clearly discernible in the spectrograms shown in panel a and b. Although the intensity FWHM of the pulses is already shorter than 10 fs, these post-pulses contain significant intensity and may blur the intended sub-cycle snapshot of terahertz-field-driven dynamics. Consequently, the compressor has been re-designed to primarily compensate the TOD, while the GVD may additionally be minimized by chirped mirrors (section 2.2.1).

[1]Note that due to the symmetry of the second-harmonic FROG scheme, the sign of the time axis in figure A.1d is not well-defined but arbitrarily chosen.

Appendix B

Broadband critical phase matching in BBO

To resolve the temporal structure of high-order harmonics, a preferably broadband phase matching range in the cross-correlation experiment (section 4.1.1) is crucial due to the ultra-broad emission bandwidth in HHG (see, e.g., figure 4.2). The commonly employed nonlinear material BBO not only features a very broad transparency range, but also a relatively flat dispersion. In combination with a comparably high nonlinear coefficient, these properties render the material an ideal choice for sum-frequency generation of high-order harmonics and the ultrashort gating pulses. For this specific purpose, critical phase matching requires the wave vector mismatch

$$\Delta k = k_{\mathrm{HH}} + k_{\mathrm{gate}} - k_{\mathrm{SF}} \tag{B.1}$$

to be minimized, where the indices 'HH', 'gate' and 'SF' denote the wave vectors of the high-order harmonics, the gating pulse and the generated sum-frequency signal, respectively. Since BBO is uni-axially negative birefringent, $\Delta k = 0$ can only be fulfilled for a given triplet of frequencies, if the lowest-frequency pulse, i.e., the HH pulse train, addresses the ordinary refractive index. The gate pulse may either be polarized perpendicular or parallel to the optical axis. The first case corresponds to a polarization setting often denoted with "ooe" (where o and e stand for ordinary and extraordinary polarization of the involved pulses arranged from lowest to highest frequencies) and is named type I phase matching, while the latter corresponds to type II with polarizations "oee". For a given crystal length L, the wave vector mismatch may be determined from the known dispersion of BBO [Eim87] for different internal angles α between the propagation direction of the pulses and the optical axis. The generated sum-frequency

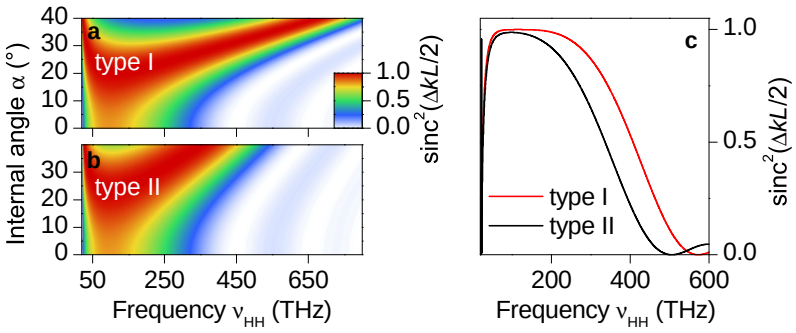

Figure B.1: Broadband sum-frequency generation in a 10-µm-thin BBO crystal: a,b, Colour-coded representation of the phase matching curves (a: type I (ooe), b: type II (oee)) for different internal angles α between the propagation direction and the optical axis of BBO as a function of the high-order harmonic frequency ν_{HH}. The wavelength of the gating pulse has been kept constant at $\lambda_{\mathrm{gate}} = 840\,\mathrm{nm}$. **c,** Efficiency curves for type I (red) and type II (black) phase matching for an internal angle $\alpha = 20°$.

intensity I_{SF} is proportional to

$$I_{\mathrm{SF}} \propto \left(\frac{\sin(\Delta kL/2)}{\Delta kL/2}\right)^2 = \mathrm{sinc}(\Delta kL/2)^2. \tag{B.2}$$

Figures B.1a and b show the corresponding phase matching curves for type I (a) and type II (b) phase matching as a function of the high-order harmonic frequency for different internal angles α. For simplicity, the wavelength of the gate pulse has been kept constant at a value of $\lambda_{\mathrm{gate}} = 840\,\mathrm{nm}$ in the calculations. Even under this limiting assumption, the achievable bandwidth covers more than 500 THz for the case of type I phase matching (see figure B.1c).

In the experiment described in section 4.1.1, the polarization of the gating pulse has thus been chosen parallel to the HH polarization and perpendicular to the optical axis. The thin BBO crystal has been cut at an angle of 20° with respect to the optical axis, which ensures minimal reflection losses under normal incidence. A comparison of the reconstructed HH spectrum (figure 4.2) proves that the determined phase matching bandwidth is sufficiently broad and the detection range is rather limited by the rapidly decreasing intensity of high-order harmonics with increasing frequencies.

Appendix C

XFROG reconstruction scheme

As described in section 4.1.1, an XFROG reconstruction scheme has been applied to extract the temporal intensity $I_{\mathrm{HH}}(t)$ and phase $\varphi_{\mathrm{HH}}(t)$ of the high-order harmonic pulse train from the recorded cross-correlation signal. A brief explanation of the different steps of data processing and numerical reconstruction from the initial raw data acquisition to the retrieved HH time structure shall be given here.

For every single delay time τ between the gating pulse and the HH pulse train, the spectral intensity of the sum-frequency (SF) signal is recorded, yielding a two-dimensional spectrogram $I_{\mathrm{SF}}(\omega, \tau)$. The recorded SF intensity is enclosed by remaining spectral signatures of the strongly suppressed gating pulse and its second harmonic at the low- and high-frequency side, respectively. To isolate the SF signal before the reconstruction is performed, the intensity at these spectral regions is set to zero by numerically applying a suitable mask function. Since the gating spectrum covers a spectral region of more than 100 THz, sum-frequency components consisting of the sum of lowest HH orders and lowest frequencies within the gating spectrum are covered by the latter (see figure 4.2b) and are consequently removed by applying the mask function. To avoid sharp spectral edges leading to artificial features in the reconstructed time structure, a spectral flank (wing of a Gaussian function) is added to the sharp low-frequency cut-off, thereby ascertaining that the exact shape and position of this flank does not significantly influence the resulting time trace. For the applied XFROG algorithm (see below) to work properly, the temporal and spectral grid of the 2D spectrogram has to be adjusted such that τ and ω are Fourier transforms of each other. To this end, the dataset is numerically interpolated on a new grid, consisting of 1024 data points along the time and frequency axis each. Finally, a faint noise floor on the order of 10^{-4} of the maximum measured intensity is removed in order to avoid unreasonable reconstruction of weak fluctuations. The subsequently applied numerical reconstruction algorithm is based on open-source

MATLAB code [Wya]. This code has been developed on the basis of reference [Kan98], which also underlies the following brief explanation. Mathematically, the HH pulses can be described by

$$E_{\mathrm{HH}}(t) = \mathrm{Re}\left\{\sqrt{I_{\mathrm{HH}}(t)}\exp\left[i\omega_0 t + i\varphi_{\mathrm{HH}}(t)\right]\right\}, \tag{C.1}$$

where $I_{\mathrm{HH}}(t)$ and $\varphi_{\mathrm{HH}}(t)$ are the time-dependent HH intensity and phase, respectively, and ω_0 is the centre frequency. The frequency mixing field (including the sum-frequency signal which is evaluated here) for a given delay time τ is the product of the HH field with the delayed field of the gating pulse

$$E_{\mathrm{SF}}(t,\tau) = E_{\mathrm{HH}}(t)E_{\mathrm{gate}}(t-\tau), \tag{C.2}$$

which is named the *physical constraint*. This signal has to be compared to the experimentally accessible observable, which is the spectrally resolved SF intensity, here. Fourier transformation of the signal field given in equation (C.2) yields this connection via

$$I_{\mathrm{SF}}(\omega,\tau) = \left|\int_{-\infty}^{\infty} E_{\mathrm{HH}}(t)E_{\mathrm{gate}}(t-\tau)\exp(-i\omega t)dt\right|^2, \tag{C.3}$$

which is named the *intensity constraint*. Since I_{SF} is a real quantity, the reconstruction algorithm has to find the phase $\phi(\omega,\tau)$ in the equation

$$\sqrt{I_{\mathrm{SF}}}\phi(\omega,\tau) = \int_{-\infty}^{\infty} E_{\mathrm{SF}}(t,\tau)\exp(-i\omega t)dt. \tag{C.4}$$

To provide a reasonable starting point for the reconstruction algorithm, the field profile of the gating pulse is extracted from a second-harmonic FROG reconstruction (see figure 2.7) and implemented as an initial guess for the shape of the gating pulse $E_{\mathrm{gate}}(t)$. It is kept fixed for the first five iterations, before the algorithm is running in a double-blind fashion for 85 iterations, i.e., both pulse shapes are dynamically adapted. During every iteration step, a guess $E_{\mathrm{guess}}(t,\tau)$ for the time-domain representation $E_{\mathrm{SF}}(t,\tau)$ is calculated whose Fourier transform yields the frequency domain representation $\sqrt{I_{\mathrm{guess}}(\omega,\tau)}\phi_{\mathrm{guess}}(\omega,\tau)$. The square root is subsequently replaced by the measured signal, and a next guess E(t) is calculated via an inverse Fourier transformation of $\sqrt{I_{\mathrm{SF}}(\omega,\tau)}\phi_{\mathrm{guess}}(\omega,\tau)$. An effective and time-saving way to calculate the next guess is realized by an algorithm based on the so-called *Principal Component Generalized Projections* [Kan99], which will not be described here. In an iterative way, the algorithm thus alternates between the time domain, where the *physical constraint* (equation (C.2)) is applied, and the frequency domain, where the *intensity constraint* (equation (C.3)) is applied, thereby minimizing the error between the measured and the reconstructed spectrograms, $I_{\mathrm{SF}}(\omega,\tau)$ and $I_{\mathrm{guess}}(\omega,\tau)$, respectively (see figure 4.3a and b).

Appendix D

Symmetry of perturbative nonlinearities in gallium selenide

In chapter 5, the symmetry of emitted high-order harmonics and their polarization has been discussed and compared to the behaviour expected for perturbative harmonics (see figure 5.7f). Here, a brief summary of the straightforward derivation of this perturbatively assigned symmetry shall be given.

It is most convenient to introduce a Cartesian coordinate system (x, y, z), where $\mathbf{x}$ is oriented along the crystallographic a-axis of the crystal (compare figure 5.1) and $\mathbf{z}$ points along the c-axis perpendicular to the layer plane. In the following, a scenario as described in sections 5.3 and 5.4 will be discussed, where the fundamental driving field $\mathbf{E}$ is always oriented perpendicular to $\mathbf{z}$, i.e., $\mathbf{E} = (E_x, E_y, E_z) = E_0 \cdot (\cos\alpha, \sin\alpha, 0)$. The angle alpha is consequently connected to the in-plane angle ϕ (see chapter 5) via $\alpha = \phi - 30°$. Following equation (3.1), the Cartesian component i of the perturbative nonlinear polarization of order n may be written as

$$P_{\mathrm{i}}^{(\mathrm{n})} \propto \sum_{\lambda_1 \ldots \lambda_\mathrm{n}} \chi^{(\mathrm{n})}_{\mathrm{i}\lambda_1\ldots\lambda_\mathrm{n}} E_{\lambda_1} \cdot \ldots \cdot E_{\lambda_\mathrm{n}}, \tag{D.1}$$

where $\lambda_1, \ldots, \lambda_\mathrm{n}$ represent the coordinates x, y, z. As two examples, the second- and third-order nonlinear polarization vectors,

$$P_{\mathrm{i}}^{(2)} \propto \sum_{\mathrm{jk}} \chi^{(2)}_{\mathrm{ijk}} E_\mathrm{j} E_\mathrm{k} \quad \text{and} \quad P_{\mathrm{i}}^{(3)} \propto \sum_{\mathrm{jkl}} \chi^{(3)}_{\mathrm{ijkl}} E_\mathrm{j} E_\mathrm{k} E_\mathrm{l}, \tag{D.2}$$

respectively, will be derived in the following. The form of the susceptibility tensor is defined by the crystal symmetry. Group-theoretical considerations thus allow for a determination of the non-vanishing tensor elements of $\chi^{(2)}$ and $\chi^{(3)}$. For the point group

D_3^{h} of ε-type GaSe, the second order nonlinear tensor features only four non-vanishing elements, none of which are independent [Boy03]:

$$\chi^{(2)}_{yyy} = -\chi^{(2)}_{yxx} = -\chi^{(2)}_{xxy} = -\chi^{(2)}_{xyx} \tag{D.3}$$

Inserting the driving field in equation (D.2) yields the in-plane components of the second order nonlinear polarization as a function of α:

$$P_x^{(2)} \propto E_0^2 \cdot 2\sin\alpha\cos\alpha = E_0^2 \cdot \sin(2\alpha), \tag{D.4}$$

$$P_y^{(2)} \propto E_0^2 \cdot \left\{(\cos\alpha)^2 - (\sin\alpha)^2\right\} = E_0^2 \cdot \cos(2\alpha). \tag{D.5}$$

The polarization angle θ_{pol} as shown in figure 5.7 is the difference between the angle enclosed by the nonlinear polarization and the **x**-axis, and α:

$$\begin{aligned}\theta_{\mathrm{pol}} &= \tan^{-1}\left\{\frac{P_y^{(2)}}{P_x^{(2)}}\right\} - \alpha = \tan^{-1}(\cot(2\alpha)) - \alpha \\ &= \tan^{-1}(\tan(90^\circ - 2\alpha)) - \alpha = 90^\circ - 3\alpha\end{aligned} \tag{D.6}$$

Consequently, the polarization of the perturbative second harmonic continuously rotates when the incident field polarization is varied [Cat78], as shown in figure 5.7. In particular, the polarization is found to be parallel to the incident field for $\alpha = 30^\circ$ ($\phi = 0^\circ$) and perpendicular for $\alpha = 0^\circ$ ($\phi = 30^\circ$).
The fourth-rank tensor of the third-order nonlinear susceptibility exhibits eight non-vanishing elements [Boy03]

$$\begin{aligned}&\chi^{(3)}_{xxxx} = \chi^{(3)}_{yyyy} = \chi^{(3)}_{xxyy} + \chi^{(3)}_{xyyx} + \chi^{(3)}_{xyxy} \\ \text{with}\quad &\chi^{(3)}_{xxyy} = \chi^{(3)}_{yyxx}, \quad \chi^{(3)}_{xyyx} = \chi^{(3)}_{yxxy}, \quad \chi^{(3)}_{xyxy} = \chi^{(3)}_{yxyx}.\end{aligned} \tag{D.7}$$

An analogous derivation as for the second order polarization yields

$$P_x^{(3)} \propto E_0^3 \cdot \{\cos^3\alpha + \cos\alpha\sin^2\alpha\} = E_0^3 \cdot \cos\alpha \quad \text{and} \tag{D.8}$$

$$P_y^{(3)} \propto E_0^3 \cdot \{\sin^3\alpha + \sin\alpha\cos^2\alpha\} = E_0^3 \cdot \sin\alpha. \tag{D.9}$$

which results in the polarization angle

$$\theta_{\mathrm{pol}} = \tan^{-1}\left\{\frac{P_y^{(3)}}{P_x^{(3)}}\right\} - \alpha = \alpha - \alpha = 0^\circ. \tag{D.10}$$

The polarization of the perturbative third harmonic thus always follows the incident field vector, irrespective of the in-plane orientation of the sample (figure 5.7).

Appendix E

Publications

Publications in peer-reviewed journals

- F. Langer, M. Hohenleutner, C. Schmid, C. Poellmann, P. Nagler, T. Korn, C. Schüller, M. S. Sherwin, U. Huttner, J. T. Steiner, S. W. Koch, M. Kira, and R. Huber
  Lightwave-driven quasiparticle collisions on a sub-cycle timescale
  Nature (2016), accepted

- T. Maag, A. Bayer, S. Baierl, M. Hohenleutner, T. Korn, C. Schüller, D. Schuh, D. Bougeard, C. Lange, R. Huber, M. Mootz, J. E. Sipe, S. W. Koch, and M. Kira
  Coherent cyclotron motion beyond Kohn's theorem
  Nature Physics **12**, 119-123 (2016)

- M. Hohenleutner, F. Langer, O. Schubert, M. Knorr, U. Huttner, S. W. Koch, M. Kira, and R. Huber
  Real-time observation of interfering crystal electrons in high-harmonic generation
  Nature **523**, 572-575 (2015)

- O. Schubert, M. Hohenleutner, F. Langer, B. Urbanek, C. Lange, U. Huttner, M. Kira, S. W. Koch, and R. Huber
  Sub-cycle control of terahertz high-harmonic generation by dynamical Bloch oscillations
  Nature Photonics **523**, 119-123 (2014)

- C. Lange, T. Maag, M. Hohenleutner, S. Baierl, O. Schubert, E. R. J. Edwards, D. Bougeard, G. Woltersdorf, and R. Huber
  Extremely Nonperturbative Nonlinearities in GaAs Driven by Atomically Strong Terahertz Fields in Gold Metamaterials
  Physical Review Letters **113**, 227401 (2014)

Reports at international conferences and workshops

- M. Hohenleutner, F. Langer, O. Schubert, M. Knorr, C. Lange, U. Huttner, S. W. Koch, M. Kira, and R. Huber
  Sub-cycle quantum interference in solid-state high-harmonic generation
  DPG Spring Meeting 2016, Regensburg, Germany, March 2016

- M. Hohenleutner, F. Langer, O. Schubert, M. Knorr, C. Lange, U. Huttner, S. W. Koch, M. Kira, and R. Huber
  Sub-cycle terahertz control of strong-field quantum interference in solid-state high-harmonic generation (invited talk)
  International Conference on Extreme Light (ICEL 2015), Bucharest, Romania, November 2015

- M. Hohenleutner
  Sub-cycle high harmonics from terahertz-driven crystal electrons (invited talk)
  Future of Ultrashort Pulses, Munich, Germany, September 2015

- M. Hohenleutner, O. Schubert, F. Langer, C. Lange, U. Huttner, D. Golde, T. Meier, M. Kira, S. W. Koch, and R. Huber
  High-order harmonic generation by dynamical Bloch oscillations in a bulk solid
  Winter School on Ultrafast Processes in Condensed Matter (WUPCOM 2015), Reit im Winkl, Germany, March 2015

- M. Hohenleutner, O. Schubert, F. Langer, C. Lange, U. Huttner, D. Golde, T. Meier, M. Kira, S. W. Koch, and R. Huber
  Phase-Locked Multi-Terahertz High-Harmonic Generation by Dynamical Bloch Oscillations (invited talk)
  Mid-IR Optoelectronics: Materials and Devices (MIOMD 2014), Montpellier, France, October 2014

- M. Hohenleutner, O. Schubert, F. Langer, B. Urbanek, C. Lange, U. Huttner, D. Golde, T. Meier, M. Kira, S. W. Koch, and R. Huber
  Phase-locked Multi-THz High-Harmonic Generation by Dynamical Bloch Oscillations in Bulk Semiconductors (invited talk)
  Ultrafast Phenomena XIX, Okinawa, Japan, 2014
  Springer Proceedings in Physics 162, 721 (2015)

- M. Hohenleutner, O. Schubert, F. Langer, C. Lange, U. Huttner, D. Golde, T. Meier, M. Kira, S. W. Koch, and R. Huber
  Phase-locked multi-THz fields control high-harmonic generation by dynamical Bloch oscillations in a bulk semiconductor
  4th EOS Topical Meeting on Terahertz Science & Technology (EOS-TST 2014), Camogli, Italy, May 2014

Bibliography

[Alf06] R. R. Alfano, *The Supercontinuum Laser Source*, 2nd ed., Springer Science and Business Media, 2006.

[Ant96] P. Antoine, A. L'Huillier, and M. Lewenstein, *Attosecond Pulse Trains Using High-Order Harmonics*, Physical Review Letters **77**, 1234-1237 (1996).

[Aus84] D. H. Auston, K. P. Cheung, J. A. Valdamis, and D. A. Kleinman, *Cherenkov Radiation fro Femtosecond Optical Pulses in Electro-Optic Media*, Physical Review Letters **53**, 1555-1558 (1984).

[Aws07] D. D. Awschalom and M. E. Flatté, *Challenges for semiconductor spintronics*, Nature Physics **3**, 153-159 (2007), and references therein.

[Bai16] S. Baierl, M. Hohenleutner, L. Braun, T.-M. Do, C. Lange, A. Sell, M. Fiebig, G. Woltersdorf, T. Kampfrath, and R. Huber, *Terahertz-driven nonlinear spin response of antiferromagnetic nickel oxide*, submitted (September 2015).

[Bak08] M. I. Bakunov, S. B. Bodrov, and M. V. Tsarev, *Terahertz emission from a laser pulse with tilted front: Phase-matching versus Cherenkov effect*, Journal of Applied Physics **104**, 073105 (2008).

[Bal02] A. Baltuška, T. Fuji, and T. Kobayashi, *Controlling the carrier-envelope phase of ultrashort light pulses with optical parametric amplifiers*, Physical Review Letters **88**, 133901 (2002).

[Bas09] M. Bass, C. Decusatis, J. Enoch, V. Lakshminarayanan, G. Li, C. MacDonald, V. Mahajan, and E. Van Stryland, *Handbook of Optics*, 3rd ed., vol. 4, McGraw-Hill Education, 2009.

[Bat10] M. Battiato, K. Carva, and P. M. Oppeneer, *Superdiffusive spin transport as a mechanism of ultrafast demagnetization*, Physical Review Letters **105**, 027203 (2010).

[Bea02] M. C. Beard, G. M. Turner, and C. A. Schmuttenmaer, *Terahertz Spectroscopy*, Journal of Physical Chemistry B **106**, 7146-7159 (2002).

[Ben13] M. G. Benedict and P. Földi, *Laser driven currents in solids: dynamical Bloch oscillations and phonon scattering*, Physica Scripta **T153**, 014005 (2013).

[Ber07] L. Bergé, S. Skupin, R. Nuter, J. Kasparian, and J.-P. Wolf, *Ultrashort filaments of light in weakly ionized, optically transparent media*, Reports on Progress in Physics **70**, 1633-1713 (2007).

[Bla07] F. Blanchard, L. Razzari, H.-C. Bandulet, G. Sharma, R. Morandotti, J.-C. Kieffer, T. Ozaki, M. Reid, H. F. Tiedje, H. K. Haugen, and F. A. Hegmann, *Generation of 1.5 μJ single-cycle terahertz pulses by optical rectification from a large aperture ZnTe crystal*, Optics Express **15**, 13212-13220 (2007).

[Blo29] F. Bloch, *Über die Quantenmechanik der Elektronen in Kristallgittern*, Zeitschrift für Physik **52**, 555-600 (1929).

[Blu01] S. Blundell, *Magnetism in Condensed Matter*, Oxford University Press, 2001.

[Boy03] R. W. Boyd, *Nonlinear optics*, 3rd ed., Academic press, 2003.

[Bra00] T. Brabec and F. Krausz, *Intense few-cycle laser fields: Frontiers of nonlinear optics*, Reviews of Modern Physics **72**, 545-591 (2000), and references therein.

[Bra09] M. Bradler, P. Baum, and E. Riedle, *Femtosecond continuum generation in bulk laser host materials with sub-μJ pump pulses*, Applied Physics B **97**, 561-574 (2009).

[Bre13] J. Breuer and P. Hommelhoff, *Laser-Based Acceleration of Nonrelativistic Electrons at a Dielectric Structure*, Physical Review Letters **111**, 134803 (2013).

[Bur77] N. H. Burnett, H. A. Baldis, M. C. Richardson, and G. D. Enright, *Harmonic generation in CO_2 laser target interaction*, Applied Physics Letters **31**, 172-174 (1977).

[Cat78] I. M. Catalano, A. Cingolani, A. Minafra, and C. Paorici, *Second Harmonic Generation in Layered Compounds*, Optics Communications **24**, 105-108 (1978).

[Cha07] A. N. Chantis, K. D. Belashchenko, D. L. Smith, E. Y. Tsymbal, M. Van Schilfgaarde, and R. C. Albers, *Reversal of spin polarization in Fe/GaAs (001) driven by resonant surface states: First-principles calculations*, Physical Review Letters **99**, 196603 (2007).

[Che69] F. S. Chen, *Optically Induced Change of Refractive Indices in $LiNbO_3$ and $LiTaO_3$*, Journal of Applied Physics **40**, 3389-3396 (1969).

[Chi85] S. L. Chin, F. Yergeau, and P. Lavigne, *Tunnel ionization of Xe in an ultra-intense CO_2 laser field (10^{14} Wcm^{-2}) with multiple charge creation*, Journal of Physics B: Atomic, Molecular and Optical Physics **18**, L213-L215 (1985).

[Chi06] L. E. Chipperfield, P. L. Knight, J. W. G. Tisch, and J. P. Marangos, *Tracking individual electron trajectories in a high harmonic spectrum*, Optics Communications **264**, 494-501 (2006).

[Chi14] M. Chini, K. Zhao, and Z. Chang, *The generation, characterization and applications of broadband isolated attosecond pulses*, Nature Photonics **8**, 178-186 (2014), and references therein.

[Cor93] P. B. Corkum, *Plasma Perspective on Strong-Fields Multiphoton Ionization*, Physical Review Letters **71**, 1994-1997 (1993).

[Cor07] P. B. Corkum and F. Krausz, *Attosecond science*, Nature Physics **3**, 381-387 (2007), and references therein.

[Cou07] A. Couairon and A. Mysyrowicz, *Femtosecond filamentation in transparent media*, Physics Reports **441**, 47-189 (2007).

[Cro03] K. B. Crozier, A. Sundaramurthy, G. S. Kino, and C. F. Quate, *Optical antennas: Resonators for local field enhancement*, Journal of Applied Physics **94**, 4632-4642 (2003).

[Dat90] S. Datta and B. Das, *Electronic analog of the electro-optic modulator*, Applied Physics Letters **56**, 665-667 (1990).

[Der07] H. Dery and L. J. Sham, *Spin extraction theory and its relevance to spintronics*, Physical Review Letters **98**, 046602 (2007).

[Die06] J.-C. Diels and W. Rudolph, *Ultrashort Laser Pulse Phenomena*, 2nd ed., Academic Press, 2006.

[Dre02] M. Drescher, M. Hentschel, R. Kienberger, M. Uiberacker, V. Yakovlev, A. Scrinzi, Th. Westerwalbesloh, U. Kleineberg, U. Heinzmann, and F. Krausz, *Time-resolved atomic inner-shell spectroscopy*, Nature **419**, 803-807 (2002).

[Dro06] B. Dromey, M. Zepf, A. Gopal, K. Lancaster, M. S. Wei, K. Krushelnick, M. Tatarakis, N. Vakakis, S. Moustaizis, R. Kodama, M. Tampo, C. Stoeckl, R. Clarke, H. Habara, D. Neely, S. Karsch, and P. Norreys, *High harmonic generation in the relativistic limit*, Nature Physics **2**, 456-459 (2006).

[Dud06] N. Dudovich, O. Smirnova, J. Levesque, Y. Mairesse, M. Yu. Ivanov, D. M. Villeneuve, and P. B. Corkum, *Measuring and controlling the birth of attosecond XUV pulses*, Nature Physics **2**, 781-786 (2006).

[Eck08] P. Eckle, A. N. Pfeiffer, C. Cirelli, A. Staudte, R. Dörner, H. G. Muller, M. Büttiker, and U. Keller, *Attosecond ionization and tunneling delay time measurements in helium*, Science **322**, 1525-1529 (2008).

[Eim87] D. Eimerl, L. Davis, S. Velsko, E. K. Graham, and A. Zalkin, *Optical, mechanical, and thermal properties of barium borate*, Journal of Applied Physics **62**, 1968-1983 (1987).

[Eis14] M. Eisele, T. L. Cocker, M. A. Huber, M. Plankl, L. Viti, D. Ercolani, L. Sorba, M. S. Vitiello, and R. Huber, *Ultrafast multi-terahertz nanospectroscopy with sub-cycle temporal resolution*, Nature Photonics **8**, 841-845 (2014).

[End12] B. Endres, M. Ciorga, R. Wagner, S. Ringer, M. Utz, D. Bougeard, D. Weiss, C. H. Back, and G. Bayreuther, *Nonuniform current and spin accumulation in a 1 μm thick n-GaAs channel*, Applied Physics Letters **100**, 092405 (2012).

[Esc13] A. Eschenlohr, M. Battiato, P. Maldonado, N. Pontius, T. Kachel, K. Holldack, R. Mitzner, A. Föhlisch, P. M. Oppeneer, and C. Stamm, *Ultrafast spin transport as key to femtosecond demagnetization*, Nature Materials **12**, 332-336 (2013).

[Fab07] J. Fabian, A. Matos-Abiague, C. Ertler, P. Stano, and I. Zutic, *Semiconductor Spintronics*, Acta Physica Slovaca **57**, 565-907 (2007).

[Fei85] A. Feisst and P. Koidl, *Current induced periodic ferroelectric domain structures in $LiNbO_3$ applied for efficient nonlinear optical frequency mixing*, Applied Physics Letters **47**, 1125-1127 (1985).

[Fel92] J. Feldmann, K. Leo, J. Shah, D. A. B. Miller, J. E. Cunningham, T. Meier, G. von Plessen, A. Schulze, P. Thomas, and S. Schmitt-Rink, *Optical investigation of Bloch oscillations in a semiconductor superlattice*, Physical Review B **46**, 7252-7255 (1992).

[Fer94] N. C. Fernelius, *Properties of gallium selenide single crystal*, Progress in Crystal Growth and Characterization of Materials **28**, 275-353 (1994).

[Fie99] R. Fiederling, M. Keim, G. Reuscher, W. Ossau, G. Schmidt, A. Waag, and L. W. Molenkamp, *Injection and detection of a spin-polarized current in a light-emitting diode*, Nature **402**, 787-790 (1999).

[Föl13] P. Földi, M. G. Benedict, and V. S. Yakovlev, *The effect of dynamical Bloch oscillations on optical-field-induced current in a wide-gap dielectric*, New Journal of Physics **15**, 063019 (2013).

[Fra61] P. A. Franken, A. E. Hill, C. W. Peters, and G. Weinreich, *Generation of optical harmonics*, Physical Review Letters **7**, 118-120 (1961).

[Fre12] J. K. Freericks, A. Y. Liu, A. F. Kemper, and T. P. Devereaux, *Pulsed high harmonic generation of light due to pumped Bloch oscillations in noninteracting metals*, Physica Scripta **T151**, 014062 (2012).

[Fül10] J. A. Fülöp, L. Pálfalvi, G. Almási, and J. Hebling, *Design of high-energy terahertz sources based on optical rectification*, Optics Express **18**, 12311-12327 (2010).

[Gal99] G. Gallot and D. Grischkowsky, *Electro-optic detection of terahertz radiation*, Journal of the Optical Society of America B **16**, 1204-1212 (1999).

[Gan05] S. D. Ganichev and W. Prettl, *Intense Terhaertz Excitation of Semiconductors*, Oxford University Press, 2005.

[Ghi10] S. Ghimire, A. D. DiChiara, E. Sistrunk, P. Agostini, L. F. DiMauro, and D. A. Reis, *Observation of high-order harmonic generation in a bulk crystal*, Nature Physics **7**, 138-141 (2010).

[Ghi12] S. Ghimire, A. D. DiChiara, E. Sistrunk, G. Ndabashimiye, U. B. Szafruga, A. Mohammad, P. Agostini, L. F. DiMauro, and D. A. Reis, *Generation and propagation of high-order harmonics in crystals*, Physical Review A **85**, 043836 (2012).

[Ghi14] S. Ghimire, G. Ndabashimiye, A. D. DiChiara, E. Sistrunk, M. I. Stockman, P. Agostini, L. F. DiMauro, and D. A. Reis, *Strong-field and attosecond physics in solids*, Journal of Physics B: Atomic, Molecular and Optical Physics **47**, 204030 (2014).

[Gün09] G. Günter, A. A. Anappara, J. Hees, A. Sell, G. Biasiol, L. Sorba, S. De Liberato, C. Ciuti, A. Tredicucci, A. Leitenstorfer, and R. Huber, *Sub-cycle switch-on of ultrastrong light-matter interaction*, Nature **458**, 178-181 (2009).

[Gol08] D. Golde, T. Meier, and S. Koch, *High harmonics generated in semiconductor nanostructures by the coupled dynamics of optical inter- and intraband excitations*, Physical Review B **77**, 075330 (2008).

[Gol11] D. Golde, M. Kira, T. Meier, and S. W. Koch, *Microscopic theory of the extremely nonlinear terahertz response of semiconductors*, Physica Status Solidi (B) **248**, 863-866 (2011).

[Gou07] E. Goulielmakis, V. S. Yakovlev, A. L. Cavalieri, M. Uiberacker, V. Pervak, A. Apolonski, R. Kienberger, U. Kleineberg, and F. Krausz, *Attosecond Control and Measurement: Lightwave Electronics*, Science **317**, 769-776 (2007).

[Hau09] H. Haug and S. W. Koch, *Quantum theory of the optical and electronic properties of semiconductors*, World Scientific, 2009.

[Haw15] P. G. Hawkins, M. Yu. Ivanov, and V. S. Yakovlev, *Effect of multiple conduction bands on high-harmonic emission from dielectrics*, Physical Review A **91**, 013405 (2015).

[Heb02] J. Hebling, G. Almási, I. Kozma, and J. Kuhl, *Velocity matching by pulse front tilting for large area THz-pulse generation*, Optics Express **10**, 1161-1166 (2002).

[Heb04] J. Hebling, A. G. Stepanov, G. Almási, B. Bartal, and J. Kuhl, *Tunable THz pulse generation by optical rectification of ultrashort laser pulses with tilted pulse fronts*, Applied Physics B: Lasers and Optics **78**, 593-599 (2004).

[Hig14] T. Higuchi, M. I. Stockman, and P. Hommelhoff, *Strong-Field Perspective on High-Harmonic Radiation from Bulk Solids*, Physical Review Letters **113**, 213901 (2014).

[Hir11a] H. Hirori, A. Doi, F. Blanchard, and K. Tanaka, *Single-cycle terahertz pulses with amplitudes exceeding 1 MV/cm generated by optical rectification in $LiNbO_3$*, Applied Physics Letters **98**, 091106 (2011).

[Hir11b] H. Hirori, K. Shinokita, M. Shirai, S. Tani, Y. Kadoya, and K. Tanaka, *Extraordinary carrier multiplication gated by a picosecond electric field pulse*, Nature Communications **2**, 594 (2011).

[Hoh15a] M. Hohenleutner, F. Langer, O. Schubert, M. Knorr, U. Huttner, S. W. Koch, M. Kira, and R. Huber, *Real-time observation of interfering crystal electrons in high-harmonic generation*, Nature **523**, 572-575 (2015).

[Hoh15b] M. Hohenleutner, O. Schubert, F. Langer, B. Urbanek, C. Lange, U. Huttner, D. Golde, T. Meier, M. Kira, S. W. Koch, and R. Huber, *Phase-Locked Multi-THz High-Harmonic Generation by Dynamical Bloch Oscillations in Bulk Semiconductors*, Ultrafast Phenomena XIX SE - 177, Springer Proceedings in Physics, vol. 162, Springer International Publishing, 2015.

[Hub00] R. Huber, A. Brodschelm, F. Tauser, and A. Leitenstorfer, *Generation and field-resolved detection of femtosecond electromagnetic pulses tunable up to 41 THz*, Applied Physics Letters **76**, 3191-3193 (2000).

[Hub01] R. Huber, F. Tauser, A. Brodschelm, M. Bichler, G. Abstreiter, and A. Leitenstorfer, *How many-particle interactions develop after ultrafast excitation of an electron-hole plasma.*, Nature **414**, 286-289 (2001).

[Hug00] P. G. Huggard, J. A. Cluff, G. P. Moore, C. J. Shaw, S. R. Andrews, S. R. Keiding, E. H. Linfield, and D. A. Ritchie, *Drude conductivity of highly doped GaAs at terahertz frequencies*, Journal of Applied Physics **87**, 2382-2385 (2000).

[Iwa15] K. Iwaszczuk, M. Zalkovskij, A. C. Strikwerda, and P. U. Jepsen, *Nitrogen plasma formation through terahertz-induced ultrafast electron field emission*, Optica **2**, 116-123 (2015).

[Jep11] P. U. Jepsen, D. G. Cooke, and M. Koch, *Terahertz spectroscopy and imaging - Modern techniques and applications*, Laser & Photonics Reviews **5**, 124-166 (2011).

[Jon07] B. T. Jonker, G. Kioseoglou, A. T. Hanbicki, C. H. Li, and P. E. Thompson, *Electrical spin-injection into silicon from a ferromagnetic metal/tunnel barrier contact*, Nature Physics **3**, 542-546 (2007).

[Jun10] F. Junginger, A. Sell, O. Schubert, B. Mayer, D. Brida, M. Marangoni, G. Cerullo, A. Leitenstorfer, and R. Huber, *Single-cycle multiterahertz transients with peak fields above 10 MV/cm*, Optics Letters **35**, 2645-2647 (2010).

[Jun12] F. Junginger, B. Mayer, C. Schmidt, O. Schubert, S. Mährlein, A. Leitenstorfer, R. Huber, and A. Pashkin, *Nonperturbative interband response of a bulk insb semiconductor driven off resonantly by terahertz electromagnetic few-cycle pulses*, Physical Review Letters **109**, 147403 (2012).

[Kam11] T. Kampfrath, A. Sell, G. Klatt, A. Pashkin, S. Mährlein, T. Dekorsy, M. Wolf, M. Fiebig, A. Leitenstorfer, and R. Huber, *Coherent terahertz control of antiferromagnetic spin waves*, Nature Photonics **5**, 31-34 (2011).

[Kam13] T. Kampfrath, K. Tanaka, and K. A. Nelson, *Resonant and nonresonant control over matter and light by intense terahertz transients*, Nature Photonics **7**, 680-690 (2013).

[Kan93] D. J. Kane and R. Trebino, *Characterization of Arbitrary Femtosecond Pulses Using Frequency-Resolved Optical Gating*, IEEE Journal of Quantum Electronics **29**, 571-579 (1993).

[Kan98] D. J. Kane, *Real-time measurement of ultrashort laser pulses using principal component generalized projections*, IEEE Journal of Selected Topics in Quantum Electronics **4**, 278-284 (1998).

[Kan99] D. J. Kane, *Recent Progress Toward Real-Time Measurement of Ultrashort Laser Pulses*, IEEE Journal of Quantum Electronics **35**, 421-431 (1999).

[Kan05] T. Kanai, S. Minemoto, and H. Sakai, *Quantum interference during high-order harmonic generation from aligned molecules*, Nature **435**, 470-474 (2005).

[Kat13] K. Kato, F. Tanno, and N. Umemura, *Sellmeier and thermo-optic dispersion formulas for GaSe (Revisited)*, Applied Optics **52**, 2325-2328 (2013).

[Kei16] S. Keiber, S. Sederberg, A. Schwarz, M. Trubetskov, V. Pervak, F. Krausz, and N. Karpowicz, *Electro-optic sampling of near-infrared waveforms*, Nature Photonics (2016), advance online publication, doi:10.1038/nphoton.2015.269.

[Kel65] L. V. Keldysh, *Ionization in the field of a strong electromagnetic wave*, Journal of Experimental and Theoretical Physics **20**, 1307-1314 (1965).

[Kem13] A. F. Kemper, B. Moritz, J. K. Freericks, and T. P. Devereaux, *Theoretical description of high-order harmonic generation in solids*, New Journal of Physics **15**, 023003 (2013).

[Kim10] D. H. Kim and J. A. del Alamo, *30-nm InAs PHEMTs With $f_T = 644GHz$ and $f_{\max} = 681GHz$*, IEEE Electron Device Letters **31**, 806-808 (2010).

[Kim12] K. W. Kim, A. Pashkin, H. Schäfer, M. Beyer, M. Porer, T. Wolf, C. Bernhard, J. Demsar, R. Huber, and A. Leitenstorfer, *Ultrafast transient generation of spin-density-wave order in the normal state of $BaFe_2As_2$ driven by coherent lattice vibrations*, Nature Materials **11**, 497-501 (2012).

[Kir12] M. Kira and S. W. Koch, *Semiconductor quantum optics*, Cambridge University Press, 2012.

[Koh61] W. Kohn, *Cyclotron Resonance and de Haas-van Alphen Oscillations of an Interacting Electron Gas*, Physical Review **123**, 1242-1244 (1961).

[Kot07] P. Kotissek, M. Bailleul, M. Sperl, A. Spitzer, D. Schuh, W. Wegscheider, C. H. Back, and G. Bayreuther, *Cross-sectional imaging of spin injection into a semiconductor*, Nature Physics **3**, 872-877 (2007).

[Kra30] H. A. Kramers, *Théorie générale de la rotation paramagnétique dans les cristaux*, Proceedings of the Royal Academy of Sciences at Amsterdam **33**, 959-972 (1930).

[Kra14] F. Krausz and M. I. Stockman, *Attosecond metrology: from electron capture to future signal processing*, Nature Photonics **8**, 205-213 (2014), and references therein.

[Küb04] C. Kübler, R. Huber, S. Tübel, and A. Leitenstorfer, *Ultrabroadband detection of multi-terahertz field transients with GaSe electro-optic sensors: Approaching the near infrared*, Applied Physics Letters **85**, 3360-3362 (2004).

[Kuh75] A. Kuhn, A. Chevy, and R. Chevalier, *Crystal structure and interatomic distances in GaSe*, Physica Status Solidi (A) **31**, 469-475 (1975).

[KY12] K. Ki-Yong, J. H. Glownia, A. J. Taylor, and G. Rodriguez, *High-Power Broadband Terahertz Generation via Two-Color Photoionization in Gases*, IEEE Journal of Quantum Electronics **48**, 797-805 (2012).

[Lan14] C. Lange, T. Maag, M. Hohenleutner, S. Baierl, O. Schubert, E. R. J. Edwards, D. Bougeard, G. Woltersdorf, and R. Huber, *Extremely Nonperturbative Nonlinearities in GaAs Driven by Atomically Strong Terahertz Fields in Gold Metamaterials*, Physical Review Letters **113**, 227401 (2014).

[Lan16] F. Langer, M. Hohenleutner, C. Schmid, C. Poellmann, P. Nagler, T. Korn, C. Schüller, M. S. Sherwin, U. Huttner, J. T. Steiner, S. W. Koch, M. Kira, and R. Huber, *Lightwave-driven quasiparticle collisions on a sub-cycle timescale*, Nature (2016), accepted.

[Lei99] A. Leitenstorfer, S. Hunsche, J. Shah, M. C. Nuss, and W. H. Knox, *Ultrafast high-field transport in semiconductors*, Physica B **272**, 348-352 (1999).

[Lei08] S. Leinß, T. Kampfrath, K. v.Volkmann, M. Wolf, J. T. Steiner, M. Kira, S. W. Koch, A. Leitenstorfer, and R. Huber, *Terahertz coherent control of optically dark paraexcitons in Cu2O*, Physical Review Letters **101**, 246401 (2008).

[Lew94] M. Lewenstein, P. Balcou, M. Y. Ivanov, A. L'Huillier, and P. B. Corkum, *Theory of high-harmonic generation by low-frequency laser fields*, Physical Review A **49**, 2117-2132 (1994).

[Liu07] R.-B. Liu and B.-F. Zhu, *High-order THz-sideband generation in semiconductors*, AIP Conference Proceedings **893**, 1455-1456 (2007).

[Liu12] M. Liu, H. Y. Hwang, H. Tao, A. C. Strikwerda, K. Fan, G. R. Keiser, A. J. Sternbach, K. G. West, S. Kittiwatanakul, J. Lu, S. A. Wolf, F. G. Omenetto, X. Zhang, K. A. Nelson, and R. D. Averitt, *Terahertz-field-induced insulator-to-metal transition in vanadium dioxide metamaterial*, Nature **487**, 345-348 (2012).

[Luu15] T. T. Luu, M. Garg, S. Yu. Kruchinin, A. Moulet, M. Th. Hassan, and E. Goulielmakis, *Extreme ultraviolet high-harmonic spectroscopy of solids*, Nature **521**, 498-502 (2015).

[Maa16] T. Maag, A. Bayer, S. Baierl, M. Hohenleutner, T. Korn, C. Schüller, D. Schuh, D. Bougeard, C. Lange, R. Huber, M. Mootz, J. E. Sipe, S. W. Koch, and M. Kira, *Coherent cyclotron motion beyond Kohn's theorem*, Nature Physics **12**, 119-123 (2016).

[Mai03] Y. Mairesse, A. de Bohan, L. J. Frasinsky, H. Merdji, L. C. Dinu, P. Monchicourt, P. Breger, M. Kovacek, R. Taieb, B. Carré, H. G. Muller, P. Agostini, and P. Salières, *Attosecond Synchronization of High-Harmonic Soft X-rays*, Science **302**, 1540-1543 (2003).

[Mal65] I. H. Malitson, *Interspecimen Comparison of the Refractive Index of Fused Silica*, Journal of the Optical Society of America **55**, 1205-1209 (1965).

[Mel11] A. Melnikov, I. Razdolski, T. O. Wehling, E. Th. Papaioannou, V. Roddatis, P. Fumagalli, O. Aktsipetrov, A. I. Lichtenstein, and U. Bovensiepen, *Ultrafast transport of laser-excited spin-polarized carriers in Au/Fe/MgO(001)*, Physical Review Letters **107**, 076601 (2011).

[Mén14] J. M. Ménard, C. Poellmann, M. Porer, U. Leierseder, E. Galopin, A. Lemaître, A. Amo, J. Bloch, and R. Huber, *Revealing the dark side of a bright exciton-polariton condensate*, Nature Communications **5**, 1-5 (2014).

[Moi15] N. Moiseyev, *Selection rules for harmonic generation in solids*, Physical Review A **91**, 053811 (2015).

[Müc11] Oliver D. Mücke, *Isolated high-order harmonics pulse from two-color-driven Bloch oscillations in bulk semiconductors*, Physical Review B **84**, 081202 (2011).

[Nom09] Y. Nomura, R. Horlein, P. Tzallas, B. Dromey, S. Rykovanov, Zs. Major, J. Osterhoff, S. Karsch, L. Veisz, M. Zepf, D. Charalambidis, F. Krausz, and G. D. Tsakiris, *Attosecond phase locking of harmonics emitted from laser-produced plasmas*, Nature Physics **5**, 124-128 (2009).

[Ohn99] Y. Ohno, D. K. Young, B. Beschoten, F. Matsukura, and H. Ohno, *Electrical spin injection in a ferromagnetic semiconductor heterostructure*, Nature **402**, 790-792 (1999).

[Olt14] M. Oltscher, M. Ciorga, M. Utz, D. Schuh, D. Bougeard, and D. Weiss, *Electrical Spin Injection into High Mobility 2D Systems*, Physical Review Letters **113**, 236602 (2014).

[Ord85] M. A. Ordal, R. J. Bell, R. W. Alexander, L. L. Long, and M. R. Querry, *Optical properties of fourteen metals in the infrared and far infrared: Al, Co, Cu, Au, Fe, Pb, Mo, Ni, Pd, Pt, Ag, Ti, V, and W*, Applied Optics **24**, 4493-4499 (1985).

[Pál08] L. Pálfalvi, J. A. Fülöp, G. Almási, and J. Hebling, *Novel setups for extremely high power single-cycle terahertz pulse generation by optical rectification*, Applied Physics Letters **92**, 171107 (2008).

[Pau01] P. M. Paul, E. S. Toma, P. Breger, G. Mullot, and F. Auge, *Observation of a Train of Attosecond Pulses from High Harmonic Generation*, Science **292**, 1689-1693 (2001).

[Poe15] C. Poellmann, P. Steinleitner, U. Leierseder, P. Nagler, G. Plechinger, M. Porer, R. Bratschitsch, C. Schüller, T. Korn, and R. Huber, *Resonant internal quantum transitions and femtosecond radiative decay of excitons in monolayer WSe_2*, Nature Materials **14**, 889-893 (2015).

[Por14a] M. Porer, U. Leierseder, J.-M. Ménard, H. Dachraoui, L. Mouchliadis, I. E. Perakis, U. Heinzmann, J. Demsar, K. Rossnagel, and R. Huber, *Non-thermal separation of electronic and structural orders in a persisting charge density wave*, Nature Materials **13**, 857-61 (2014).

[Por14b] M. Porer, J.-M. Ménard, and R. Huber, *Shot noise reduced terahertz detection via spectrally postfiltered electro-optic sampling*, Optics Letters **39**, 2435-2438 (2014).

[Raa15] J. Raab, *Entwicklung und Herstellung von THz-Nahfeldantennen zur ultraschnellen Spininjektion*, Master's thesis, University of Regensburg, 2015.

[Ras00] E. I. Rashba, *Theory of electrical spin injection: Tunnel contacts as a solution of the conductivity mismatch problem*, Physical Review B **62**, 267-270 (2000).

[Ros02] F. Rossi and T. Kuhn, *Theory of ultrafast phenomena in photoexcited semiconductors*, Reviews of Modern Physics **74**, 895-950 (2002), and references therein.

[RP01] F. Rosca-Pruna and M. J. J. Vrakking, *Experimental Observation of Revival Structures in Picosecond Laser-Induced Alignment of* I_2, Physical Review Letters **87**, 153902 (2001).

[Ruc12] C. Ruchert, C. Vicario, and C. P. Hauri, *Scaling submillimeter single-cycle transients toward megavolts per centimeter field strength via optical rectification in the organic crystal OH1*, Optics Letters **37**, 899-901 (2012).

[Ruf99] A. B. Ruffin, J. V. Rudd, J. F. Whitaker, S. Feng, and H. G. Winful, *Direct Observation of the Gouy Phase Shift with Single-Cycle Terahertz Pulses*, Physical Review Letters **83**, 3410-3413 (1999).

[Sai10] H. Saito, J. C. Le Breton, V. Zayets, Y. Mineno, S. Yuasa, and K. Ando, *Efficient spin injection into semiconductor from an Fe/*GaO_x *tunnel injector*, Applied Physics Letters **96**, 012501 (2010).

[Sch76] M. Schlüter, *Optical properties of GaSe and GaSxSe1-x mixed crystals*, Physical Review B **13**, 3534-3547 (1976).

[Sch00] G. Schmidt, D. Ferrand, and L. W. Molenkamp, *Fundamental obstacle for electrical spin injection from a ferromagnetic metal into a diffusive semiconductor*, Physical Review B **62**, 4790-4793 (2000).

[Sch05] P. J. Schuck, D. P. Fromm, A. Sundaramurthy, G. S. Kino, and W. E. Moerner, *Improving the mismatch between light and nanoscale objects with gold bowtie nanoantennas*, Physical Review Letters **94**, 017402 (2005).

[Sch11] O. Schubert, C. Riek, F. Junginger, A. Sell, A. Leitenstorfer, and R. Huber, *Ultrashort pulse characterization with a terahertz streak camera*, Optics Letters **36**, 4458-4460 (2011).

[Sch13a] A. Schiffrin, T. Paasch-Colberg, N. Karpowicz, V. Apalkov, D. Gerster, S. Mühlbrandt, M. Korbman, J. Reichert, M. Schultze, S. Holzner, J. V. Barth, R. Kienberger, R. Ernstorfer, V. S. Yakovlev, M. I. Stockman, and F. Krausz, *Optical-field-induced current in dielectrics*, Nature **493**, 70-74 (2013).

[Sch13b] M. Schultze, E. M. Bothschafter, A. Sommer, S. Holzner, W. Schweinberger, M. Fiess, M. Hofstetter, R. Kienberger, V. Apalkov, V. S. Yakovlev, M. I. Stockman, and F. Krausz, *Controlling dielectrics with the electric field of light*, Nature **493**, 75-78 (2013).

[Sch14a] O. Schubert, *Dynamical Bloch oscillations and terahertz high-harmonic generation in bulk semiconductors*, PhD thesis, University of Regensburg, 2014.

[Sch14b] O. Schubert, M. Hohenleutner, F. Langer, B. Urbanek, C. Lange, U. Huttner, D. Golde, T. Meier, M. Kira, S. W. Koch, and R. Huber, *Sub-cycle control of terahertz high-harmonic generation by dynamical Bloch oscillations*, Nature Photonics **8**, 119-123 (2014).

[Seg97] A. Segura, J. Bouvier, M. V. Andres, F. J. Manjon, and V. Munoz, *Strong optical nonlinearities in gallium and indium selenides related to inter-valence-band transitions induced by light pulsesro*, Physical Review B **56**, 4075-4084 (1997).

[Sel08a] A. Sell, A. Leitenstorfer, and R. Huber, *Phase-locked generation and field-resolved detection of widely tunable terahertz pulses with amplitudes exceeding 100 MV/cm.*, Optics letters **33**, 2767-2769 (2008).

[Sel08b] A. Sell, R. Scheu, A. Leitenstorfer, and R. Huber, *Field-resolved detection of phase-locked infrared transients from a compact Er:fiber system tunable between 55 and 107 THz*, Applied Physics Letters **93**, 251107 (2008).

[Ser05] J. Seres, E. Seres, A. J. Verhoef, G. Tempea, C. Streli, P. Wobrauschek, V. Yakovlev, A. Scrinzi, C. Spielmann, and F. Krausz, *Laser technology: Source of coherent kiloelectronvolt X-rays*, Nature **433**, 596-596 (2005).

[Sha09] D. Shafir, Y. Mairesse, D. M. Villeneuve, P. B. Corkum, and N. Dudovich, *Atomic wavefunctions probed through strong-field light-matter interaction*, Nature Physics **5**, 412-416 (2009).

[Sha12] D. Shafir, H. Soifer, B. D. Bruner, M. Dagan, Y. Mairesse, S. Patchkovskii, M. Yu. Ivanov, O. Smirnova, and N. Dudovich, *Resolving the time when an electron exits a tunnelling barrier*, Nature **485**, 343-346 (2012).

[She14] W. Shen, A. F. Kemper, T. P. Devereaux, and J. K. Freericks, *Exact solution for high harmonic generation and the response to an ac driving field for a charge density wave insulator*, Physical Review B **90**, 115113 (2014).

[Smi09] O. Smirnova, Y. Mairesse, S. Patchkovskii, N. Dudovich, D. Villeneuve, P. Corkum, and M. Y. Ivanov, *High harmonic interferometry of multi-electron dynamics in molecules.*, Nature **460**, 972-977 (2009).

[Su09] F. H. Su, F. Blanchard, G. Sharma, L. Razzari, A. Ayesheshim, T. L. Cocker, L. V. Titova, T. Ozaki, J.-C. Kieffer, R. Morandotti, M. Reid, and F. A. Hegmann, *Terahertz pulse induced intervalley scattering in photoexcited GaAs*, Optics Express **17**, 9620-9629 (2009).

[Tan11] T. Taniyama, E. Wada, M. Itoh, and M. Yamaguchi, *Electrical and optical spin injection in ferromagnet/semiconductor heterostructures*, NPG Asia Materials **3**, 65-73 (2011), and references therein.

[Tha07] C. Thaury, F. Quere, J.-P. Geindre, A. Levy, T. Ceccotti, P. Monot, M. Bougeard, F. Reau, P. d'Oliveira, P. Audebert, R. Marjoribanks, and Ph. Martin, *Plasma mirrors for ultrahigh-intensity optics*, Nature Physics **3**, 424-429 (2007).

[Ton07] M. Tonouchi, *Cutting-edge terahertz technology*, Nature Photonics **1**, 97-105 (2007), and references therein.

[Uib07] M. Uiberacker, Th. Uphues, M. Schultze, A. J. Verhoef, V. Yakovlev, M. F. Kling, J. Rauschenberger, N. M. Kabachnik, H. Schröder, M. Lezius, K. L. Kompa, H.-G. Muller, M. J. J. Vrakking, S. Hendel, U. Kleineberg, U. Heinzmann, M. Drescher, and F. Krausz, *Attosecond real-time observation of electron tunnelling in atoms*, Nature **446**, 627-632 (2007).

[Ulb11] R. Ulbricht, E. Hendry, J. Shan, T. F. Heinz, and M. Bonn, *Carrier dynamics in semiconductors studied with time-resolved terahertz spectroscopy*, Review of Modern Physics **83**, 543-586 (2011), and references therein.

[Vam14] G. Vampa, C. R. McDonald, G. Orlando, D. D. Klug, P. B. Corkum, and T. Brabec, *Theoretical Analysis of High-Harmonic Generation in Solids*, Physical Review Letters **113**, 073901 (2014).

[Vam15a] G. Vampa, T. J. Hammond, N. Thiré, B. E. Schmidt, F. Légaré, C. R. McDonald, T. Brabec, and P. B. Corkum, *Linking high harmonics from gases and solids*, Nature **522**, 462-464 (2015).

[Vam15b] G. Vampa, T. J. Hammond, N. Thiré, B.E. Schmidt, F. Légaré, C. R. McDonald, T. Brabec, D. D. Klug, and P.B. Corkum, *All-Optical Reconstruction of Crystal Band Structure*, Physical Review Letters **115**, 193603 (2015).

[van12] O. M. J. van't Erve, a. L. Friedman, E. Cobas, C. H. Li, J. T. Robinson, and B. T. Jonker, *Low-resistance spin injection into silicon using graphene tunnel barriers*, Nature Nanotechnology **7**, 737-742 (2012).

[Vän15] O. Vänskä, I. Tittonen, S. W. Koch, and M. Kira, *Coherent Terahertz Control of Vertical Transport in Semiconductor Heterostructures*, Physical Review Letters **114**, 1-5 (2015).

[Voz11] C. Vozzi, M. Negro, F. Calegari, G. Sansone, M. Nisoli, S. De Silvestri, and S. Stagira, *Generalized molecular orbital tomography*, Nature Physics **7**, 822-826 (2011).

[Wim14] L. Wimmer, G. Herink, D. R. Solli, S. V. Yalunin, K. E. Echternkamp, and C. Ropers, *Terahertz control of nanotip photoemission*, Nature Physics **10**, 432-436 (2014).

[Wol15] B. Wolter, M. G. Pullen, M. Baudisch, M. Sclafani, M. Hemmer, A. Senftleben, C. D. Schröter, J. Ullrich, R. Moshammer, and J. Biegert, *Strong-Field Physics with Mid-IR Fields*, Physical Review X **5**, 21034 (2015).

[Wu95] Q. Wu and X.-C. Zhang, *Free-space electro-optic sampling of terahertz beams*, Applied Physics Letters **67**, 3523-3525 (1995).

[Wu97] Q. Wu and X.-C. Zhang, *Free-space electro-optics sampling of mid-infrared pulses*, Applied Physics Letters **71**, 1285-1286 (1997).

[Wu15] M. Wu, S. Ghimire, D. A. Reis, K. J. Schafer, and M. B. Gaarde, *High-harmonic generation from Bloch electrons in solids*, Physical Review A **91**, 043839 (2015).

[Wya] A. Wyatt, *Frequency-resolved optical gating*, http://www.mathworks.com/matlabcentral/fileexchange/16235-frequency-resolved-optical-gating-frog- (MATLAB central file exchange, 7 July 2008).

[You93] D. You, D. R. Dykaar, R. R. Jones, and P. H. Bucksbaum, *Generation of high-power sub-single-cycle 500-fs electromagnetic pulses*, Optics Letters **18**, 290-292 (1993).

[You97] D. You and P. H. Bucksbaum, *Propagation of half-cycle far infrared pulses*, Journal of the Optical Society of America B **14**, 1651-1655 (1997).

[Zai96] I. Zailer, J. E. F. Frost, V. Chabasseur-Molyneux, C. J. B. Ford, and M. Pepper, *Crosslinked PMMA as a high-resolution negative resist for electron beam lithography and applications for physics of low-dimensional structures*, Semiconductor Science and Technology **11**, 1235-1238 (1996).

[Zak12] B. Zaks, R. B. Liu, and M. S. Sherwin, *Experimental observation of electron-hole recollisions*, Nature **483**, 580-583 (2012).

[Zen34] C. A. Zener, *Theory of the electric breakdown of solid dielectrics*, Proceedings of the Royal Scociety of London A **145**, 523-529 (1934).

[Zen07] T. Zentgraf, R. Huber, N. C. Nielsen, D. S. Chemla, and R. A. Kaindl, *Ultrabroadband 50-130 THz pulses generated via phase-matched difference frequency mixing in $LiIO_3$*, Optics Express **15**, 5775-5781 (2007).

[Zha06] H. Zhao, E. J. Loren, H. M. Van Driel, and A. L. Smirl, *Coherence control of hall charge and spin currents*, Physical Review Letters **96**, 246601 (2006).

[Zhu01] H. J. Zhu, M. Ramsteiner, H. Kostial, M. Wassermeier, H. P. Schönherr, and K. H. Ploog, *Room-temperature spin injection from Fe into GaAs*, Physical Review Letters **87**, 016601 (2001).

Acknowledgements

This work would not have been possible without the significant contribution and the help of numerous people. I am very grateful for this support and would like to particularly thank

- Prof. Dr. Rupert Huber for giving me the opportunity to join his team and to work on fascinating projects at the frontier of research in a prime working environment, for his steady support, the trust he put in me and the many insightful physical discussions.
- Prof. Dr. Mackillo Kira, Prof. Dr. Stephan W. Koch, Prof. Dr. Torsten Meier, Dr. Johannes T. Steiner and Ulrich Huttner for the great theoretical support during the collaborations on high-order harmonic and high-order sideband generation.
- Prof. Dr. Christian Schüller for the collaboration on the WSe_2 project and for taking the time to examine this work.
- PD Dr. Tobias Korn and Philip Nagler for the collaboration on electron-hole recollisions, in particular for providing and characterizing the WSe_2 samples.
- Prof. Dr. Mark S. Sherwin for the collaboration on the high-order sideband project.
- Prof. Dr. Dominique Bougeard, Dr. Dieter Schuh and Andreas Bayer for the collaboration on the spin injection project and for developing and growing the spin LED.
- Prof. Dr. Christian Back for the collaboration on the spin injection project.
- Dr. Olaf Schubert, Fabian Langer and Sebastian Baierl for the shared efforts in installing the terahertz high-field sources and for the great and reliable teamwork in our numerous joint projects. Special thanks to Fabian and Sebastian for proofreading this thesis.

- Dr. Christoph Lange, Thomas Maag and Andreas Bayer for the collaborations on high-field-driven charge carrier dynamics as well as the good cooperation in the lab.
- Jürgen Raab for processing, fabricating and characterizing the spin injection antennas as well as for proof-reading parts of this thesis.
- Matthias Knorr, Christoph Schmid and Benedikt Urbanek for contributing to the high-field studies during their Bachelor's projects.
- Martin Furthmeier for engineering assistance in many cases, his perfectionism in finding the best technical solutions and in particular for designing, constructing and manufacturing the cryostat.
- Imke Gronwald for her patient introduction to the e-beam lithography as well as for the elaborate fabrication of all kinds of antenna structures.
- Ulla Franzke for her help in any bureaucratic or administrative concerns and her constant cheerfulness.
- Sebastian Baierl, Dr. Tyler Cocker, Dr. Max Eisele, Martin Furthmeier, Markus Huber, Fabian Langer, Ursula Leiderseder, Thomas Maag, Dr. Christoph Pöllmann, Dr. Michael Porer and Stefan Schlauderer for the great time we had during and especially after work.
- all current and former members of the chair for numerous discussions, mutual assistance and the collegial, friendly atmosphere.
- my family for the steady and confidently support in various ways, which laid the foundations not only for this work.
- Julia, for so many reasons.